Understanding the physics behind the correlations of Gamma-ray bursts data

Onelda Bardho

UNIVERSITE DE NICE SOPHIA ANTIPOLIS

Doctorat Conjoint Erasmus Mundus Communauté Européenne
Programme Doctoral International d'Astrophysique Relativiste
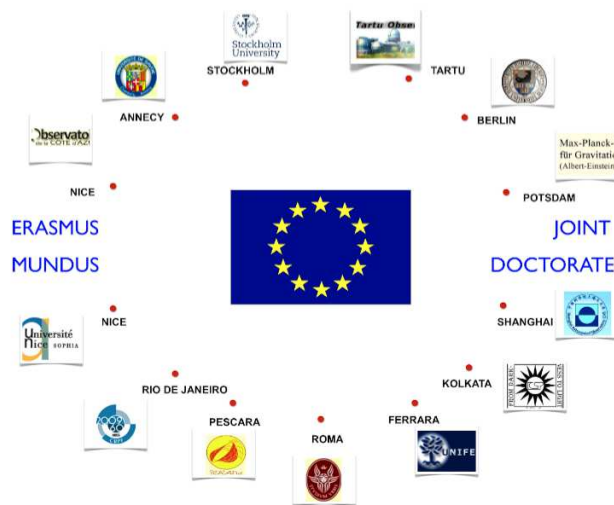
Comprendre la physique des sursauts gamma grâce aux corrèlations dans les données

Présenté et soutenue par

Onelda BARDHO

Membre Erasmus Mundus

Soutenue le 10/03/2016

Jury:

Lorenzo Amati	Chercheur, IASF-INAF	Co-Directeur de thése
Michel Boër	Directeur de Recherche CNRS	Directeur de thése
Pascal Chardonnet	Professeur	Examinateur
Enrico Costa	Directeur de Recherche, IAPS-INAF	Rapporteur
Mimoza Hafizi	Professeur	Rapporteur
Alain Klotz	Professeur	Examinateur
Bruce Gendre	Professeur Associé, HDR Astrophysique	Examinateur
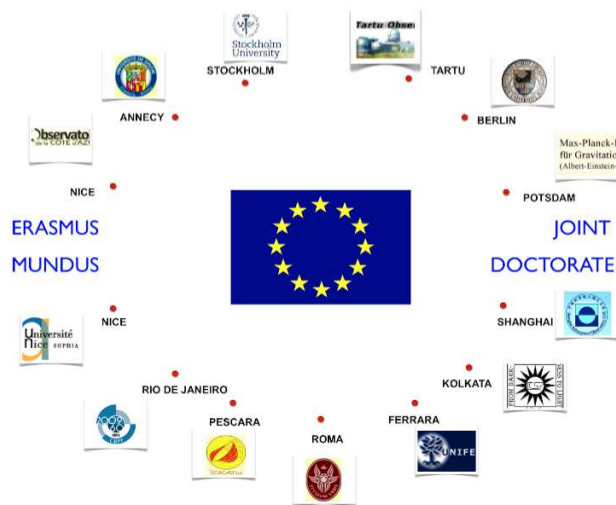
Understanding the physics behind the correlations of Gamma-Ray Bursts data

Presented and defended by

Onelda BARDHO

Erasmus Mundus Fellow

Defended on 10/03/2016

Commission:

Lorenzo Amati	Researcher, IASF-INAF	Co-supervisor
Michel Boër	Director of Research, CNRS	Supervisor
Pascal Chardonnet	Professor	Examiner
Enrico Costa	Director of research, IAPS-INAF	Reporter
Mimoza Hafizi	Professor	Reporter
Alain Klotz	Professor	Examiner
Bruce Gendre	Associate Professor, HDR Astrophysics	Examiner
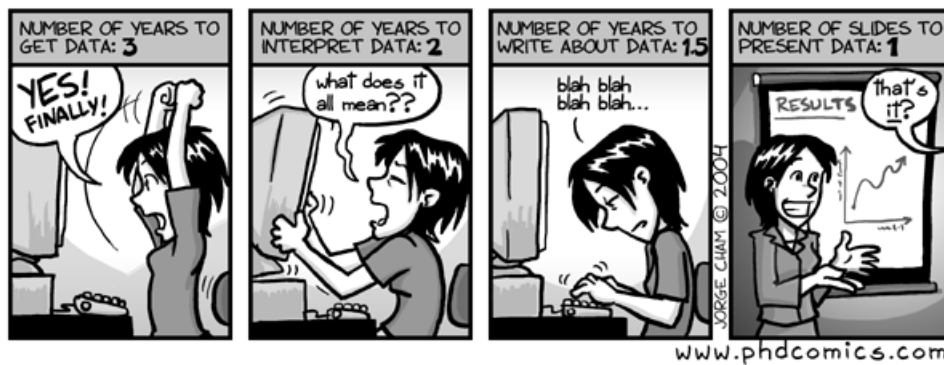
"Without data you are just another person with an opinion"

William Edwards Deming

Acknowledgments

This thesis was completed with the support of many people, who gave their specific contribution during these three years of hard work. I would like to thank each and everyone of them for their honorable and limitless help.

Firstly, I would like to thank the coordinator of the Erasmus Mundus Joint Doctorate Program, Prof. Pascal Chardonnet for his support through the European Commission and his every piece of advice throughout my PhD work. I would also like to thank the director of the Erasmus Mundus IRAP PhD program and the director of ICRANet, Prof. Remo Ruffini.

Secondly, I would like to express my sincerest gratitude to my supervisor, Dr. Michel Boër who gave me the opportunity to work with the GRB team of the ARTEMIS laboratory, in the Nice Observatory and to travel around the world, which allowed me to meet with some of the most important people in the astrophysics area. I am grateful for his valuable guidance and his expertise during my thesis work.
My special and greatest thanks go to Dr. Bruce Gendre, who effectively became my associate supervisor for all of my study. This thesis would not have been possible without his support and his guidance. His expertise made me significantly broaden my knowledge.

Third, I would like to thank my co-supervisor, Dr. Lorenzo Amati, who made my stay easy during my mobility in the INAF-CNR-Area della Ricerca di Bologna. His expertise made me to better understand data analysis processes in gamma and X-rays. His friendly behaviour made me to feel at home during my stay in Bologna. I would like to thank Prof. Filippo Frontera, who helped me with all administrative problems during my mobility. My sincere thanks go to Dr. Andrea Rossi and Dr. Eliana Palazzi for their collaboration, discussions and comments with regards to my work especially in optical analysis. I would also like to thank Dr. Cristiano Guidorzi, Dr. Elena Pian, Dr. Raffaella Landi, Dr. Giulia Stratta and Prof. Mauro Orlandini for their helpful and supportive discussions and comments during that period. I was honored to have colleagues like Dr. Elisabetta Maiorano, Dr. Natalia Auricchio and Dr. Milena Schiavone during my stay in Bologna. I would not forget the help of the PhD students of the Ferrara University, Tais Maiolino, Simone Dichiara, Camilo Delgado-Correal and Gabriel Caminha. My special thanks go to Disha Sawant for her warm friendship and continuous help.

I am indebted to my former adviser, Prof. Mimoza Hafizi, who introduced me to the research. She has been one of my biggest supporters with regards to my PhD.

My colleagues in the ARTEMIS laboratory gave me a huge help during my research study. I extend my gratitude to Hüsne Dereli, Karelle Siellez, Romain Laugier, Guillaume Langin,

Duncan Meacher and Li-Wei Wei.

I would also like to thank the director of the ARTEMIS laboratory, Dr. Catherine Nary Man who to me has been not just a director but a great moral supporter, the former director of the Observatoire de la Côte d'Azur, Prof. Farrokh Vakili, and the current director, Dr. Thierry Lanz. My thanks go also to the secretary of ARTEMIS, David Andrieux and the finance administrator, Seynabou N'Diaye, who supported my administrative problems along my stay in Nice to the maximum. The ARTEMIS laboratory personnel has been like a family for me. I would like to thank each and everyone of them for their advice, encouragement and support during my stay there.

My life in Nice as a foreigner for the last three years, would not have been easy without my friends in the Nice Observatory: Hüsne Dereli, Karelle Siellez, Sibilla Di Pace, Laurent Galluccio, Aurelie Marcotto, Narges Jami, Suvendu Rakshit, Mamdou Cisse, Arwa Dabbech, Zeinab Khorrami, Samir Kashani, Alkis Vlasis, Alvaro Rojas, Srivatsan Sridhar, Sinan Alis, Reda Bruzaite, Sarunas Mikolaitis, Giulia Macario, Judit Szulagyi, and with a lot more others. I am so glad that I met such wonderful friends and I broadened my knowledge of different cultures.

I cannot leave out the kitchen staff of Nice Observatory, Khaled Ben Saada, Karima Alem and Nadia Elhirech, for their great service and amazing lunches they have cooked during my stay here, plus now I have gotten a nick name, the Chef has named me "Madame Chocolat".

I would like to thank Vasilika Xhunga and Elvisa Daka for the English improvement of this manuscript.

I am grateful the jury members of my thesis especially my thesis reporters Prof. Mimoza Hafizi and Dr. Enrico Costa.

Last but not least, I would like to express my appreciation and gratitude to my family: my mom Tefta Bardho, my dad Veri Bardho and my brother Orges Bardho. Your unconditional love and support have always been and continue to be the main motivation in my life. My sincere gratitude goes to my aunt, Vasilika Xhunga for her endless support and consistent advice during my study and in every kind of situation along my education. A special gratitude of mine goes to Florian Bouillet, who has been a very positive force behind my back, always supporting my work and efforts, encouraging me when I was down and providing unwavering support to complete this thesis. I would like to thank Florian's family as well, for their kind support and for their understanding of my absence in their family gatherings.
I would also like to thank my friends around the world and family who I do not get to see or visit as often as I would like to, for their encouragement and support.

ONELDA BARDHO

Nice, France
March 2016

Contents

List of Figures

List of Tables

Abbreviations

AGN	**A**ctive **G**alactic **N**uclei
BATSE	**B**urst **A**nd **T**ransient **S**ource **T**elescope
BeppoSAX	**Beppo**(Nick name of famous italian physicist, Giuseppe Occhialini) **S**atellite italiano per **A**stronomia **X**
BH	**B**lack **H**ole
CCD	**C**harge **C**oupled **D**evice
ECF	**E**nergy**C**orrection **F**actor
ESA	**E**uropean **S**pace **A**gency
FoV	**F**ield **o**f **V**iew
GBM	**G**amma-ray **B**urst **M**onitor
GCN	**G**amma-ray burst **C**ircular **N**etwork
GRB	**G**amma **R**ay **B**urst
GRBM	**GRB** **M**onitor
HETE	**H**igh **E**nergy **T**ransient **TE**elescope
ISM	**I**nter **S**tellar **M**edium
LAD	**L**arge **A**rea **D**etector
LAT	**L**arge **A**rea **T**elescope
lGRB	long **G**amma **R**ay **B**ursts
NASA	**N**ational **A**eronautics and **S**pace **A**dministration
NS	**N**eutron **S**tar
PC	**P**hoton **C**ounting mode
SD	**S**pectroscopic **D**etector
SED	**S**pectral **E**nergy **D**istribution
sGRB	short **G**amma **R**ay **B**ursts
SNR	**S**uper**N**ova **R**emnant
SXC	**S**oft **X**-ray **C**amera
WFC	**W**ide **F**ield **C**amera
WT	**W**indow **T**iming mode
WXM	**W**ide field **X**-ray **M**onitor
XMM-Newton	**X**-ray **M**ulti-Mirror **M**ission
XRF	**X** - **R**ay **F**lash

Symbols

Symbol	Name
z	Redshift
α	Decay Index
β	Spectral Index
E_p	Peak Energy
E_{iso}	Isotropic Energy
F	Flux
L	Luminosity
S	Fluence
Γ	Bulk Lorentz Factor
ν_m	Injection Frequency
ν_c	Cooling Frequency
ν_a	Self-absorption Frequency
D_L	Luminosity Distance at a given redshift
t_{rest}	Time in the rest frame
t_{obs}	Time in the observer frame

Résumé

Les sursauts (de rayonnement) gamma (Gamma-ray bursts GRBs) sont des flashs lumineux émanant du cosmos. Ce sont des événements parmi les plus mystérieux que nous sommes capables d'observer depuis leur découverte. Un phénomène aussi énergétique ($10^{51} - 10^{54}$ ergs) dans un laps de temps aussi court (environ dix secs) le rend parmi les plus intéressant et énigmatique car c'est une quantité d'énergie équivalente à celle ce que génèrerait notre Soleil en 10 milliards d'années.

Ces impulsions de rayons gamma proviennent de sources extragalactiques et sont aléatoirement (isotropiquement) réparties dans l'espace. Ils sont temporellement constitués de 2 parties:

- Le sursaut de rayons gamma à proprement parler, aussi appelé émission brève (prompt emission)

- Puis un rayonnement rémanent (afterglow emission) dans des longueurs d'onde allant des rayons X aux ondes radio moins énergétiques et pouvant durer jusqu'à plusieurs jours.

Ces événements extrêmement lumineux ont été accidentellement découverts par le satellite militaire Vela, le 2 Juillet 1967. Celui ci était alors censé détecter des explosions nucléaires à ciel ouvert telles qu'interdites par le "Traité d'interdiction partielle des essais nucléaires" (LTBT) du 5 Aout 1963 entre les Etats-Unis et l'URSS.

Les GRBs sont répartis en deux catégories en fonction de leur durée:

- Les GRBs brefs qui durent moins de deux secondes et présentent un spectre "dur" (hard spectrum): plus riche en hautes fréquences

- Les GRBs longs qui durent plus de deux secondes et spectre "mou" (soft spectrum).

Contrairement aux GRBs brefs/durs, de nombreux GRBs long/mous sont reliés à des supernovas.
Ces deux types de GRBs proviennent de progéniteurs différents:

- Les GRBs longs ont lieu du fait de l'effondrement d'étoiles massives

- Les courts sont vus comme le résultat dune fusion d'un système binaire (deux étoiles à neutrons, ou une étoile à neutron et un trou noir).

A l'heure actuelle, la meilleure modélisation de la physique des GRBs est celle du modèle dit de la "boule de feu".

Quelque soit le type de GRBs, le progéniteur crée un trou noir qui expulse une grande quantité d'énergie dans un petit volume et la propage dans le milieu environnant sous la forme de deux jets dans deux directions opposées. Les mécanismes physiques à l'origine des radiations brèves et rémanentes sont supposés être une radiation synchrotron et/ou une diffusion Compton inverse (ICS).

Le lancement du satellite *Swift* a marqué le dèbut d'une nouvelle ère dans l'étude des GRBs. En effet, *Swift* est capable de fournir une localisation précise des GRBs grâce à ses capacités d'orientation rapide. En outre *Swift* nous montre que les GRBs ont un comportement canonique en ce qui concerne l'émission rémanente dans le rayonnement X dont les courbes lumineuses sont constituées de trois ou quatre lois puissance.

Dans le chapitre 1, je donnerai un aperçu des GRBs, du point de vue historique, instrumental et théorique. Je mentionnerai également les corrélations classiques entre paramètres observés qui ont pour but de rendre les GRBs assimilables à des chandelles standards (standard candles).

L'idée de départ de ce projet est la standardisation des GRBs en tant qu'outil d'étude de la cosmologie et au delà la compréhension plus profonde des progéniteurs des différents groupes de GRBs et de leur sous classes.

Le processus d'analyse de données reste le point clé de l'étude des GRBs.

Dans le chapitre 2, je donnerai une explication détaillée de l'analyse des rayons X provenant des satellites *Swift* et Fermi. Le processus d'analyse de données sera expliqué dans les cas temporels et spectraux en indiquant les opérations à effectuer dans les différentes étapes de l'analyse.

Les résultats de chaque GRB sont publiés et libre d'accès sur le dépôt "*Swift*-XRT GRB" après le lancement du satellite *Swift*.

Les résultats de l'analyse dans le domaine des rayons X a un impact sur la correction d'empilement (pile-up correction), la sélection de région ainsi que les retranchements de mauvaises colonnes et de fond (bad columns and background substraction). Ces différentes corrections ont une influence directe sur les résultats scientifiques tirés des observations associées. Je comparerai également mon analyse manuelle avec l'analyse automatique faite par le dépôt officiel de *Swift*.

Dans le chapitre 3, je présenterai dans ce manuscrit une étude détaillée du GRB 141221A dans différentes longueurs d'onde.

GRB 141221A est un GRB observé depuis l'infrarouge jusque dans le rayonnement gamma faiblement énergétique. C'est un sursaut détecté par *Swift* le 21 Décembre 2014 à 08:07:10 UTC. La durée du sursaut était celle typique de GRB long ($T_{90} = 36.9 \pm 4.0\,\text{s}$), ce qui a permis aux télescopes terrestres de démarrer leur observation alors l'émission brève était encore visible.

Dans le domaine des rayons X, l'explosion est très similaire à tous les GRBs observés précédemment avec un éclat lumineux tardif (late flare). Dans le domaine optique cependant, les courbes lumineuses montrent une hausse inhabituelle, un pseudo-plateau et diverses cassures temporelles. Nous expliquons ces cassures par le passage de certaines fréquences spécifique du modèle dans le domaine optique. Un choc inverse est nécessaire à minima pour complétement expliquer à la fois les courbes de lumière et de spectre dans le domaine optique.

Une autre possibilité serait la présence d'une composante temporelle afin d'expliquer la répartition d'énergie spectrale (SED). Dans ce cas, la dernière cassure temporelle observée serait due à un effet de jet (jet effect). Cela mènerait cependant à considérer certaines propriétés bien que ce ne soit pas formellement exclu par le modéle comme extrêmes et en plus à prendre en compte la présence d'une émission thermique dans la partie molle (soft) du domaine des rayons X. Toutes ces observations sont inhabituelles et difficiles à expliquées.

Il est clair que ces deux solutions sont un défi aux modèles standards des GRBs. Dans le premier cas, toutes les données sont en faveur de l'absence de vent stellaire durant tout le phénomène, ce qui est en contradiction avec les modèles actuels. Dans le dernier cas, les paramètres microphysique obtenus par le modèle sont très étranges voir même excluent complètement la cohérence du modèle.

Le GRB 141221A devraient être ajouté à la courte liste des GRBs très étranges pour lesquels de nouveaux modèles devraient être testés.

Dans le chapitre 4, je décrirai le travail statistique effectué sur le regroupement (clustering) des GRBs dans le domaine des rayons X.
Durant l'ère pré-*Swift*, un regroupement des émissions rémanentes des GRBs a été observé dans les domaines X, optiques et infrarouges. Dans le domaine des rayons X, cette classification est constituée de trois groupes:

- Le groupe 1 (Gr. I) dont les émissions rémanentes sont brillantes avec un flux moyen de $= 7.0 \times 10^{-12} erg\, s^{-1}\, cm^{-2}$,

- Le groupe 2 (Gr. II) dont les émissions rémanentes sont plus faibles avec un flux moyen de $= 3.1 \times 10^{-12} erg\, s^{-1}\, cm^{-2}$ et enfin

- Le groupe 3 (Gr. III) dont les émissions rémanentes sont faibles et dont les valeurs sont plus ou moins aberrantes.

Cette classification a été dèbattue après le lancement de *Swift*. Ce travail est donc dans la continuité des travaux de Boër et Gendre.

Nous avons utilisé un échantillon de 254 émissions rémanentes pour vérifier cette classification dans l'ère *Swift*. Cet échantillon est constitué des GRBs longs et dont le décalage vers l'infrarouge est connu jusqu'en Février 2013. Nous avons corrigé les valeurs de flux en fonction des dilatations de temps et de distance et des pertes d'énergie dus aux effets cosmologiques. Cet échantillon montre une dispersion de la distribution du flux après un jour. Les courbes de lumière de cette distribution ont été normalisées en fonction du décalage vers l'infrarouge. Nous avons investigué ce problème d'éparpillement selon trois axes:

- La possibilité d'un problème instrumental,

- La possibilité d'un problème de calibration des données,

- La possibilité de l'absence de regroupement des GRBs.

Le point de départ de l'examen du problème instrumental a été la répartition mensuelle de 35 GRBs problématiques situés entre les groupes 1 et 2 Cette distribution illustre certains effets saisonniers en Juillet, Aout et Octobre. Le résultat de cette étude nous parvient sous la forme d'une comparaison avec les répartitions mensuelles des 254 GRBs de l'échantillon complet pour ces mois particuliers. La distribution cumulée jour après jour tout au long de l'année ou de certains mois illustre également le problème.

La comparaison des distributions d'indices spectraux des 35 GRBs problématiques, des derniers GRBs au sein desquels nous pouvions trouver des regroupements ainsi que de l'ensemble des échantillons ne montre pas de différences claires.

Cela signifie que tous ces échantillons présentent des distributions identiques de leurs indices spectraux. Nous ne pouvons donc pas identifier de groupes au sein de ces échantillons.
Dans tous ces cas, la distribution cumulée montre que les mois problématiques sont Juillet, Aout et Octobre.

Nous avons des preuves que certains problèmes pourraient être causés par la trop faible valeur de l'angle de limbe de la terre (earth limb angle) par rapport à la direction du GRB. Des valeurs inférieures à 45 degrés doivent être systématiquement exclues, ce qui n'est pas toujours le cas.

La calibration des données est également une étape de l'analyse de données qui peut poser problème. En comparant mon analyse spectrale avec celle du dépôt de *Swift*-XRT, il est apparu que, bien que la plupart des spectres soient similaires, il existe des incohérences pour 11.2 d'entre eux. Certaines d'entre elles sont facilement explicables par une différence de l'étendue temporelle sur laquelle est effectué le calcul du spectre ou du modèle d'ajustement de spectre. D'autres sont plus difficiles à expliquer et comprendre.

Le facteur de correction d'énergie (ECF) est un élément supplémentaire de divergence entre les analyses automatiques et manuelles. Il dépend directement du flux du modèle de GRB utilisé. L'analyse manuelle approche de manière bien plus précise les minima locaux. Cela implique que l'analyse automatique ne donne pas de résultats précis en ce qui concerne le facteur de conversion.

La dernière possibilité, celle de la non existence des regroupements de GRBs pourrait être un effet de sélection. En effet, avant le lancement de *Swift*, la possibilité d'observer des émissions rémanentes dans le spectre X était très faible.

Dans le chapitre 5, j'apporterai une conclusion à mes travaux et présenterai des pistes pour investiguer plus profondément ces problématiques.
Une d'entre elles serait d'analyser plus en détail les GRBs problématiques afin de trouver s'il existe des problèmes observationnels pendant les solstices et les équinoxes. Cela mènerait à la vérification des effets potentiels de la position du satellite par rapport aux positions du soleil, de la lune et de la terre. Un problème de fond (background) induit par l'orbite pourrait alors être mis en évidence. Par ailleurs, l'étude des paramètres orbitaux durant une année complète pourrait nous donner un indice de la présence ou non de ces problèmes. L'investigation des 35 GRBs problématiques dans le domaine optique serait également une étude intéressante. Elle confirmerait les problèmes, s'ils existent, pour ces GRBs.

De plus, une étude de la distribution des courbes de lumière dans le domaine optique de ces GRBs par rapport à tous les GRBs utilisés nous apporterait également des informations intéressantes. Cette étude serait une vérification utile des différentes propriétés qui peuvent avoir une influence sur les instruments de mesure durant une observation.

L'analyse de données devrait être vérifiée doublement en ce qui concerne l'information fournie par le GRB et le but d'une étude. Une petite variation d'un des paramètres de l'analyse peut avoir d'énormes conséquences sur le résultat d'une étude. Cela signifie qu'une analyse de données manuelle pour une étude particulière n'est jamais une perte de temps dans les cas où une analyse particulière, requise pour une étude spécifique ne puisse pas être effectuée depuis le dépôt *Swift*-XRT de données spectrale.
Les pipelines existants sont une bonne option pour ne pas perdre de temps à refaire l'analyse des données. Mais des différences apparaissent quand le but d'une étude requiert des informations au-delà de celles que peut fournir une analyse automatique.

Un autre travail possible postérieurement à cette étude serait une simulation qui choisirait aléatoirement un certain nombre de GRBs et calculerait la distribution du flux après un jour pour déterminer la probabilité que le regroupement existe ou non.
Dans ce cas, la simulation signalerait une différence entre analyse manuelle et automatique qui signifierait que le processus automatique doit être entièrement ré-exécuté afin de l'améliorer dans des optiques variées.

Abstract

GRBs are flashes of gamma-rays coming from the cosmos. They are one of the most mysterious events we have been able to observe since their discovery. GRBs are classified into two groups: long/soft GRBs and short/hard GRBs. Their emission mechanism consists of two phases: prompt emission and afterglow emission. The launch of the *Swift* satellite opened a New Era in the GRBs research. *Swift* is able to provide accurate position for more GRBs than previous missions, thanks to its fast capabilities of slewing. Furthermore the *Swift* shows that GRBs have a canonical behavior for the X-ray afterglow light curves.

The data analysis process remains the key point of the GRBs studies. I present a detailed study of the peculiar GRB 141221A at different wavelengths. GRB 141221A shows an unusual steep rise in the optical light curve of the afterglow. The broad band spectral energy distribution, taken near the maximum of the optical emission, presents either a thermal component or a behavior break. This burst displays unusual feature in the optical band, whereas the X-ray data is more common. GRB 141221A is one of the challenging bursts that excludes a stellar wind from the progenitor of the GRBs.

A clustering in the X-ray afterglow light curves was observed before the launch of the *Swift* satellite. This feature has been debated after the launch of the *Swift*. We have built a sample of 254 GRBs that shows a scattering of the data for the flux distribution at one day. This distribution was investigated with a normalization of light curves at redshift one. We have investigated the problem into three different directions: instrumental problems; data calibration problems and absence of clustering.

The investigation of the instrumental problems is related to the observation problems of the *Swift* satellite along the year, since we observe some seasonal effects during solstices and equinoxes. The earth limb angle is one evidence indicating that there are not instrumental problems rather than data processing problems. The data shows that the admission limit angle is overtaken.

The data calibration process is an interesting issue which might influence the results of the study. I provide different of evidence towards the problems that can induce serious flows in the results of the data analysis process, by comparing the manual and the automatic data analysis found from *Swift* - XRT repository. I suggest the cases where the manual analysis should be performed and the cases where the automatic analysis does not affect the results.

The last possibility of the non-existence of this clustering should be a selection effect. This is because, before the launch of the *Swift* satellite, the possibility of observing the X-ray afterglow was extremely low. However, it is extremely difficult to find a bias in this analysis that was performed using the data from two different satellites.

Chapter 1

Introduction

1.1   Gamma-Ray Bursts

Gamma-Ray Bursts (GRBs) are still one of the most mysterious events in the universe, after almost 48 years since their discovery. Being such an event that in a short period of time (around 10 sec) it releases an amount of energy around $10^{51} - 10^{54}$ ergs makes them highly enigmatic and interesting, since this is an amount of energy that our Sun would radiate in 10 billion years of its lifetime. These bright flashes of gamma-rays are extragalactic events and are randomly distributed on the sky. They consist of flashes of gamma-rays which may last from seconds to hours (the so-called prompt emission). The radiation of X-ray, optical/UV and radio emission can last up to several days but is less energetic (the so-called afterglow emission).

These extremely luminous events were accidentally discovered by the Vela military satellites on July 2, 1967, (Klebesadel et al., 1973), which was a mission seeking the signature of the Partial Test Ban Treaty in 1963, between the Soviet Union and the United States. The goal of the Vela satellites was to watch for the gamma-ray radiation emitted by nuclear weapons inside and outside the atmosphere of the Earth. The first publication related to GRBs was made in 1973 (Klebesadel et al., 1973), when 16 GRBs were observed.

Several missions were launched and step by step these phenomena were opening a new hot topic in the Astrophysics community. On April 5, 1991, NASA launched the Compton Gamma Ray Observatory, on-board of which was the Burst and Transient Source Experiment (BATSE), mostly dedicated to the GRB research. BATSE detected 2704 GRBs during its 9-year lifetime and proved that GRBs are uniformly distributed in the sky and that they have extragalactic or galactic-halo origin. The detection of the first X-ray afterglow was done by the BeppoSAX satellite, an Italian – Dutch mission launched on April 30, 1996. The first X-ray and optical detections were realized almost, one year after the launch, thus in 1997 a new era emerged for the GRB afterglow research. This led to redshift measurement and the evidence of the relation of lGRBs with supernovae (SNe).

Almost three years after the evidence of progenitors of lGRBs, there was the first evidence of optical afterglow of sGRBs, dark GRBs and X-ray flashes, which came from the detection of HETE-2 (High Energy Transient Explorer, a NASA - CNES - RIKEN mission launched on

October 9, 2000). Despite all these discoveries, the New Era of studying the GRBs started after the launch of *Swift* (a NASA mission launched on November 20, 2004) and Fermi (a NASA mission launched on June 11, 2008).

1.2   Classification of GRBs

When the BATSE instrument had observed many GRBs, Kouveliotou et al., 1993 checked the distribution of time for around 222 GRBs and they found two different groups (Fig. 1.1). According to this new classification, GRBs are separated into two groups based on their duration: short GRBs which last for less than 2 seconds and long GRBs that last for more than 2 seconds. This bimodality of GRB duration was also reported earlier from Dezalay et al., 1992 using the data from the Phebus experiment. Currently, it is assumed that the origin of short GRBs is the merger of two binary systems such as Neutron Star (NS) - Neutron Star or Neutron Star - Black Hole (BH), whereas the origin of the long GRBs is the collapse of massive stars. In both
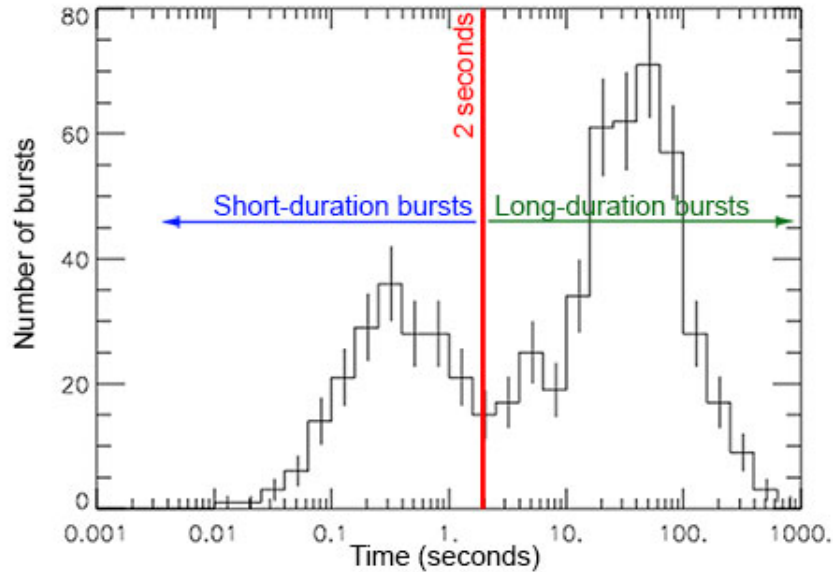
FIGURE 1.1: Duration of distribution for 222 BATSE GRBs. Credit: Kouveliotou et al., 1993

cases of these two different progenitors, they end in a BH. But this does not mean that the emission mechanism and the released energy are the same for short and long GRBs. Usually it is seen that short GRBs exhibit a harder spectrum than the long ones. In long/soft GRBs we see that many of them are associated with Supernova, while we do not see this association for short/hard GRBs.

All these ideas of the classification of GRBs related to the duration and hardness ratio started to be debated after the GRB 060614 (Gehrels et al., 2006). This GRB is considered to show a long duration ($>2\,\text{sec}$) but a hard spectrum. Later, a new idea popped out for the classification of GRBs as Type I for GRBs that have a compact star as a progenitor and Type II GRBs for those that have a massive star as a progenitor (Zhang, 2011, Zhang et al., 2009).

1.3   Progenitors of GRBs

The study of the progenitors is one of the most difficult part in the study of GRBs. Until recently, only the framework of the progenitors is well known, two different classes of GRBs, have different progenitors. Hence we can classify the progenitors of GRBs in two types:

Collapsar Model

The Collapsar Model is thought to be related to the long GRBs. This model consists of the collapse of the iron core of massive stars (alone or in a binary system) directly in a BH. In order for the Collapsar Model to be reliable, it should fulfill these three requirements: 1. A massive core, 2. The hydrogen envelope should be removed before the death of the star and 3. A high angular momentum.

To be a massive star for the progenitor of a GRB means that it should happen in the brightest region of the host galaxy. The metallicity for the formation of a GRB is required to be low. Thus, in this way it will be a weak stellar wind that allows for the creation of more massive core and BHs as well (Fryer et al., 2007). The second requirement is true, since we have the evidence of the association of lGRBs with supernovae. The third requirement is highly significant, since in this case it will support a debris torus around the BH in order to create a spinning BH that has a natural rotation along the axis, creating in this manner the jet (Fryer et al., 1999).

Merger Model

Different from lGRBs, there is no evidence for sGRBs showing that their progenitors can be a massive star that collapses. Their progenitors might be a merger between a binary system (NS-NS and/or NS-BH). In a few seconds (less than 2 sec), the two objects, while rotating closer and closer to each other, will lose their energy and due to the tidal forces they will merge together releasing an immense amount of energy. These mergers can happen in old galaxies with no star formation (see Berger, 2013 for a review).

1.4   The Pre-*Swift* Era

All observations and results that we have thus far for all of the observed GRBs are due to the instruments dedicated to the GRBs research. Since their accidental discovery in the late '60s, a lot of instruments were launched for observing GRBs providing as much information as possible.

One of the first instruments dedicated to GRBs research was BATSE, launched on April 5, 1991. BATSE consisted of eight identical pairs of detectors. Each pair contains two NaI scintillation detectors: a Large Area Detector (LAD) optimized for sensitivity and directional response and a Spectroscopy Detector (SD) optimized for energy coverage and resolution (Fig. 1.2).

The sensitivity of LAD and SD were $2025\,cm^2$ and $127\,cm^2$ respectively, while the energy range were $20\,\mathrm{keV}$ – $1.9\,\mathrm{MeV}$ and $10\,\mathrm{keV}$ and $100\,\mathrm{MeV}$ respectively. The minimum resolution was
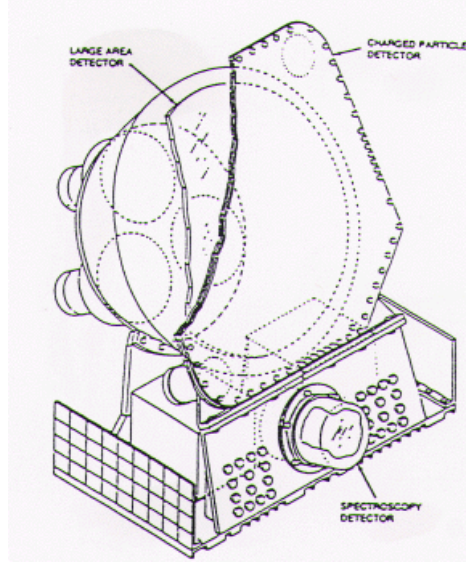
FIGURE 1.2: One of the eight identical detectors of BATSE. Credit: NASA/BATSE

$2\,\text{sec}$, while the burst sensitivity for $1\,\text{sec}$ was $3 \times 10^{-8}\,erg/cm^2$. BATSE has completed several important discoveries for GRBs. The most important one is the isotropic distribution of GRBs in the sky.

The first hint for an isotropic distribution was given by Atteia et al., 1987. In 1992, Meegan et al., 1992 provided evidence showing that the weakest and brightest GRBs are isotropic and the weakest ones are as isotropic as the longest ones. This confirms that GRBs are not located in our Galaxy, but they are extragalactic events. After building the 3rd BATSE catalog, Briggs et al., 1996, by using 1005 GRBs confirmed the isotropic distribution of GRBs. This feature of GRBs for 2704 BATSE GRBs is well seen in Fig. 1.3.
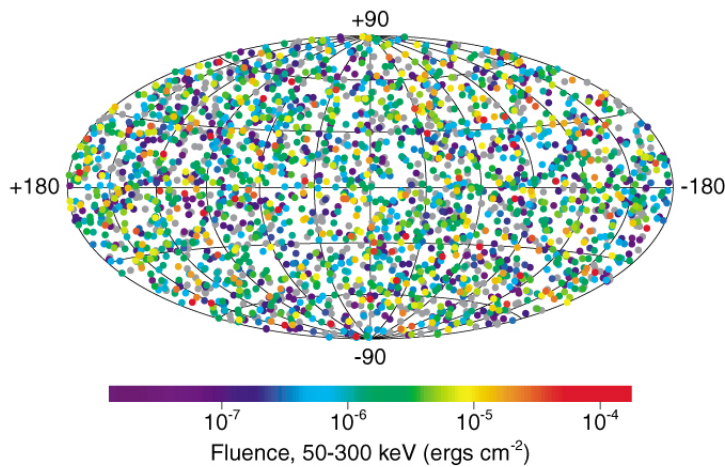
FIGURE 1.3: Isotropic distribution for 2704 BATSE GRBs. Credit: NASA/BATSE

Another important discovery made by BATSE is the classification of GRBs in "short" and "long"

events. Last, but not least, it was the radiated spectrum of the prompt phase of GRBs (see Section 1.7), which was discovered thanks to the data collected by BATSE.

The second mission dedicated to the GRBs research was BeppoSAX, launched on April 30, 1996. BeppoSAX (Boella et al., 1997) consisted of GRB Monitor (GRBM) and Wide Field Camera (WFC), Fig. 1.4. The GRBM is composed of four identical CsI(Na) scintillator slabs. The energy range for GRBM (Costa et al., 1998, Frontera et al., 1997) and WFC (Jager et al., 1997) were 40-700 keV and 2-26 keV respectively. The GRBs were located with a precision of around 3 arcminutes.
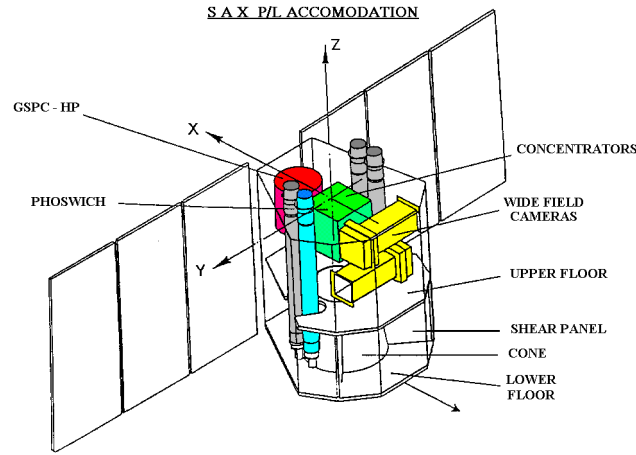
FIGURE 1.4: BeppoSAX instrument. Credit: NASA/BeppoSAX

During the 6 years of observing, BeppoSAX made fundamental discoveries related to GRBs. The key of its success was the capability of BeppoSAX to obtain arcminute positions in a few hours.

BeppoSAX was the first satellite able to discover the multi wavelength afterglow. The observation of the first X-ray (Costa et al., 1997a,b) and optical afterglow (Groot et al., 1997, van Paradijs et al., 1997) was seen for GRB 970228. It was the first one with a measurement of the distance, at redshift z=0.835 (Bloom et al., 1998). Whereas the radio afterglow was detected on the GRB 970508 (Frail et al., 1997) and the first GRB observed in all wavelengths. Hence, it started a new Era in GRBs research: *The Afterglow Era.*
Another discovery of BeppoSAX is the first dark GRB, GRB 970828 (Groot et al., 1998). Whereas GRB 980425A was the first GRB that gave the evidence of the relation of lGRBs with the supernovae (SNe). In 2002 Amati et al., 2002, by using the prompt phase of GRBs α–decay index, found a tight correlation between E_{peak} – the peak Energy and E_{iso}– the isotropic energy radiated by GRBs during the prompt phase (see Section 1.8).

HETE-1 was the third satellite dedicated to GRBs. The first attempt was made on November 4, 1996, but one day after the launch, the two instruments died because the rocket was unable to release them. Then on October 9, 2000, NASA launched HETE-2, using the spare flight model of HETE-1 satellite. On the board of HETE-2 there were four wide field gamma-ray detectors (FREGATE), one wide field X-ray Monitor (WXM), one soft X-ray camera (SXC) and four

wide fields near-UV CCD cameras. These instruments were sensitive to 6-400 keV, 2-25 keV and 0.5-10 keV respectively for gamma-ray detectors, X-ray Monitor and soft X-ray camera (see Fig. 1.5).
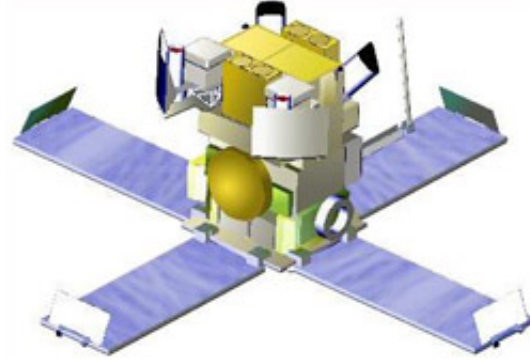
FIGURE 1.5: HETE-2 Instrument. Credit: NASA/HETE

Compared to previous missions, HETE-2 was able to get a precise position for GRBs, quicker than BeppoSAX, since all of its instruments were simultaneously looking to the sky. HETE-2 was getting the position within tens of seconds.

The discoveries made by HETE-2 are also as significant as the discoveries made by the two previous instruments. Thanks to these capabilities, HETE-2 was able to observe X-ray flashes (XRFs) and X-ray rich GRBs for the first time and to solve the mystery of the progenitors of sGRBs. The contribution in confirming the association of lGRBs with SNe was another important discovery of HETE-2.

1.5 *Swift* Era and the Canonical X-Ray light-curve

The *Swift* mission, launched on November 20, 2004, is a medium-sized explorer (MIDEX) mission dedicated to GRB astronomy (Gehrels et al., 2004). It orbits at 567 km x 585 km with a period of ~ 95.9 min. *Swift* is the first multi wavelength mission for the study of GRBs, being elaborated by an international collaboration.

Swift consists of three instruments: BAT (Burst Alert Telescope), XRT (X-ray telescope) and UVOT (Ultraviolet/Optical Telescope), (Fig. 1.6).

Swift is a mission totally dedicated to the GRB study, while trying to find answers to these questions:

- Which are the properties of the afterglow?

- Which are the progenitors of GRBs?

- Do different classes of GRBs exist?

- Can we study the early Universe with GRBs?

- What is the evolution of the outflow and the interaction with its surroundings like?
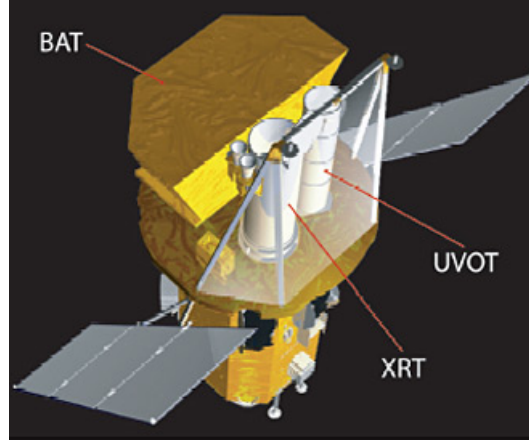
FIGURE 1.6: *Swift* satellite. Credit: NASA/*Swift*

BAT

BAT (Barthelmy et al., 2005) is dedicated to the observation of the prompt emission (the radiation of GRBs). It is an instrument with very high sensitivity (5.3 mCrab), large Field of view (FoV) (1.4 sr half-coded), time resolution 64 s and energy range 15-150 keV. BAT has a detecting area of $5240\,cm^2$ and consists of a detector plane of 32.768 CZT detector elements, a coded aperture mask located 1 m above the detector plane, a graded-Z fringe to reduce the instrumental background rate and diffuse cosmic background, a thermal radiator and control system to keep the detector plane at a constant temperature (Fig. 1.7 and Fig. 1.8).
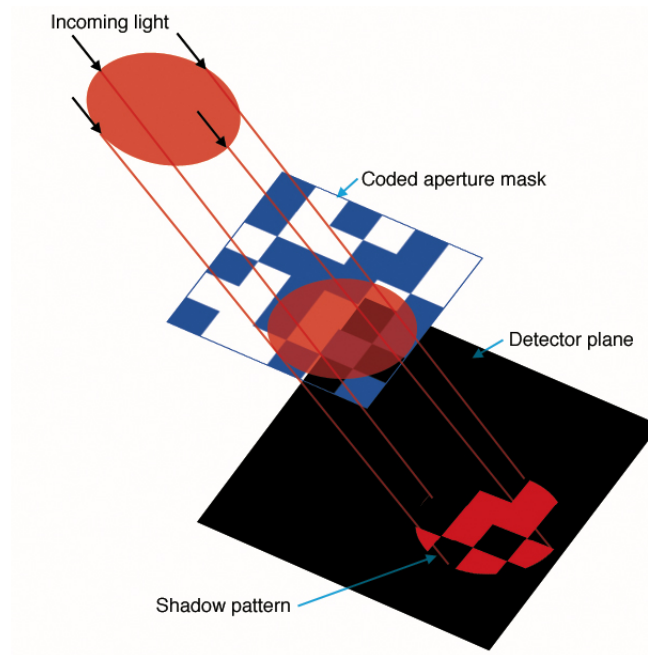
FIGURE 1.7: BAT instrument. Credit: NASA/*Swift*

The three main goals of BAT are:

- The discovery of new transient X-ray sources

- The detection of outflows

- The study of light curves
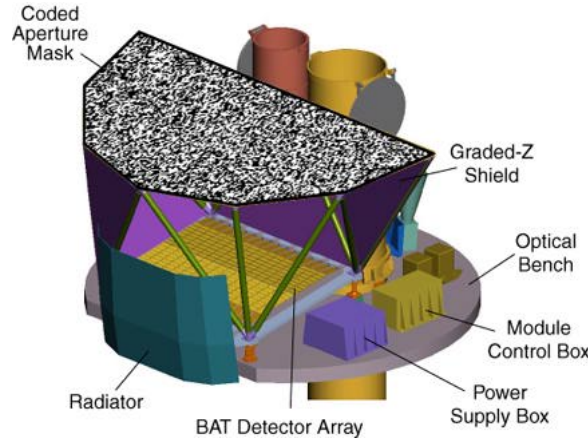
FIGURE 1.8: Position of the different detectors in the BAT instrument. Credit: NASA/*Swift*

BAT detects the burst and computes the initial position within 10 sec and sent it to the spacecraft and ground. Then the spacecraft slews (if it is needed). This is the first mode of BAT (burst mode). The second mode is the survey mode, which produces hard X-ray survey data. While BAT is searching for a burst, it surveys all the sky for the hard X-ray transients. During this mode, the instrument collects count rate data in 5 minute time bins for 80 Energy intervals. More details Krimm et al., 2013.

XRT

XRT (Burrows et al., 2005) is dedicated to the observation of light curves, spectra and fluxes of both GRBs and afterglows over a wide dynamic range of more than 7 orders of magnitude in flux. XRT determines GRBs position in 5 arcsec accuracy less than 100 seconds after the burst. XRT is sensitive in the X-ray band (0.2-10 keV). FoV is smaller than BAT (23.6 x 23.6 arcmin), but aligned with it and with resolution of 18 arcsec.

The XRT uses a set of Wolter 1 mirrors for focusing the X-rays, from XMM-Newton/EPIC MOS detector spare. The set of mirrors consists of the X-ray mirrors, thermal baffle, a mirror collar and an electron deflector (Fig. 1.9).

The main goals of creating XRT are:

- To determine a rapid and accurate position

- To moderate resolution spectroscopy and accurate photometry
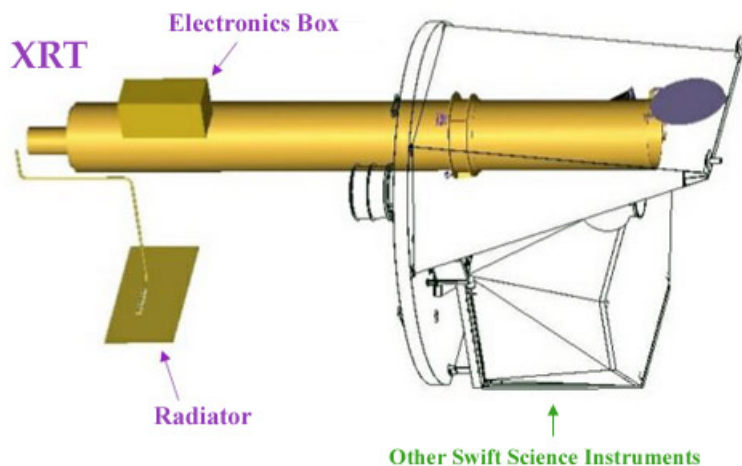
FIGURE 1.9: XRT instrument. Credit: NASA/*Swift*

- To investigate light curves with high timing resolution

The following 4 observing systems were created to reach these goals: Imaging Mode (IM), Window Timing mode (WT), Photon Counting mode (PC) and Photo Diode mode (PD). PD has not been working from May 27, 2005, because a micrometeoroid hit the CCD of the XRT and produced a very high background rate in this mode.

UVOT

UVOT (Roming et al., 2005) is dedicated to the observation of the UV and optical afterglows within the early minutes in the wavelengths 170-600 nm. It has a Ritchey-Crétien telescope with a 30 cm primary mirror and an f-number of 12.7. UVOT is co-aligned with XRT and has a FoV of 17 x 17 arcmin. The maximum magnitude that UVOT can reach is 24 in 1000 s in white light. UVOT consists of 5 units (Fig. 1.10):

- The telescope module (TM) which in itself consists of:

  1. UV/optical telescope
  2. A beam steering mirror
  3. Two redundant filter wheel mechanisms
  4. Photon counting detectors
  5. Power supplies
  6. Electronics

- Two digital electronics modules (DEMs)

- Two interconnecting units to connect TM to DEMs
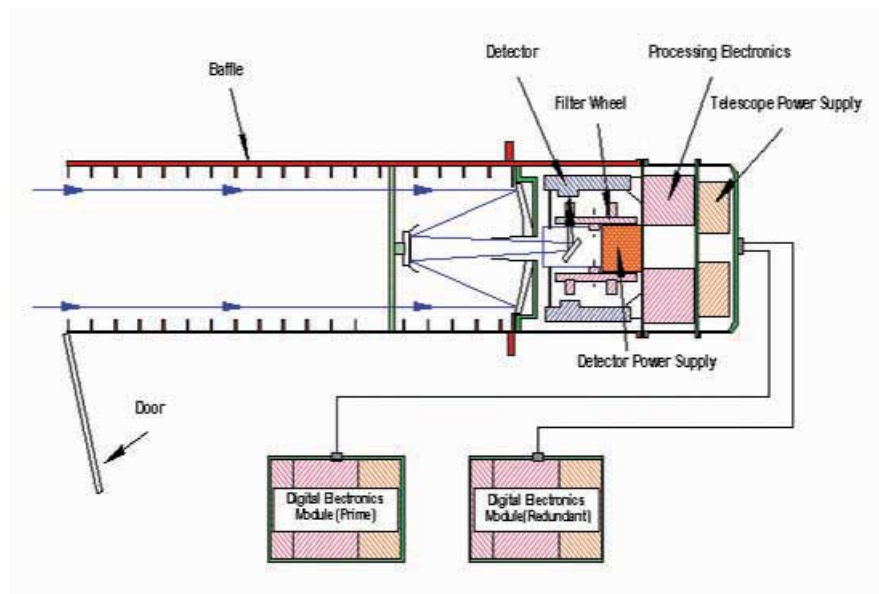
FIGURE 1.10: UVOT instrument. Credit: NASA/*Swift*

The main goals of UVOT are:

- To capture the early light of GRBs

- To rapidly determine their positions to sub-arcsecond accuracy

- To quickly follow-up GRB afterglows

- To identify the GRB environment

- To provide spectral and photometric redshifts

- To provide timing analysis of GRB afterglows

- To solve the question of dark bursts

UVOT uses 5 operating systems to reach its goals: settling, finding charts, automated targets, pre-planned targets and safe pointing targets. When the spacecraft slews to the target, the UVOT does not observe in order to protect itself from damage due to bright sources.

Swift has big advantages compared to other missions because of its small error boxes related to the location of GRBs and its fast capability of rotating. These are the great properties of *Swift* which opened a new era in the GRBs research.

The observation of a canonical light-curve of the X-ray afterglow was one of the most important discoveries of *Swift* in the beginning of its operation. Such an observation, mostly for the early X-ray afterglow, was almost impossible from the previous missions when they were following the X-ray afterglow several hours after the trigger of GRB. Whereas *Swift*, thanks to its fast slewing, obtains the observation only after one minute. In such a short time, *Swift* is able to

figure out the transition between prompt and afterglow emission and determine the connection between these two phases.

Nousek et al., 2006 proposed a canonical light curve for the X-ray afterglow, which consists of 3 or 4 power laws (see Fig. 1.11).
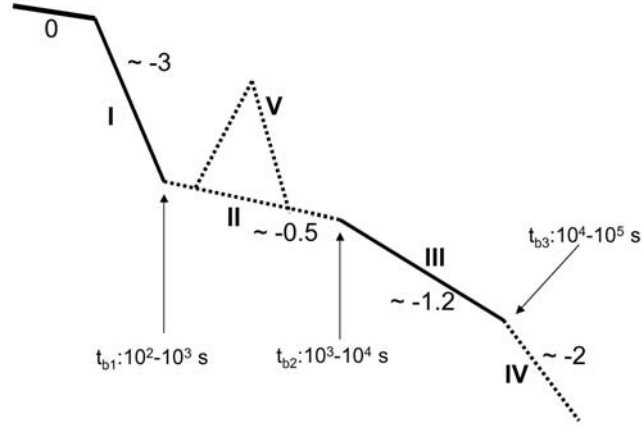
FIGURE 1.11: A cartoon of the canonical light curve for X-ray afterglow light curves. See the text for explanation. Credit: Zhang et al., 2006

The X-ray afterglow of a light curve might have one or more of these phases (Nousek et al., 2006, Zhang et al., 2006):

- **An initial steep decay (I)**: This is a phase with a very rapid decay $(3 < \alpha_1 < 5)$, usually known as GRB tail emission, since it is considered to be the tail of the prompt emission. There are different ideas on the creation of this phase. One of these ideas is related to the prompt emission, considering that internal shocks are created at large angles compared to the line of sight and they obviously reach the observer with a delay as: $\Delta t \equiv R\theta^2/2c$. Another idea of this steep decay is coming from Kobayashi et al., 2006 which assumes that the initial steep decay is caused by a reverse shock emission from large angles relative to our line of sight propagating in a magnetized ejecta. The emission can be either Synchrotron or Synchrotron Self-Compton (SSC). Other ideas are: the emission from a hot cocoon caused by a Collapsar Model (for further details see Mészáros and Rees, 2001, Ramirez-Ruiz et al., 2002), or a patchy shell (for further details see Kumar and Piran, 2000, Tagliaferri et al., 2005). In all cases the decay is given as: $\alpha = 2 + \beta$ due to the curvature effect.

- **Shallow decay (II)**: This is a phase with a very small decay $(0.5 < \alpha_2 < 1)$ which indicates about the transition between prompt and afterglow emissions. The shallow decay is the most unknown to date, among all the phases of X-ray afterglow light curve. There are a lot of ideas explaining the emission mechanism of this phase (Nousek et al., 2006), but only two of them are the most acceptable: 1. A smooth and gradual energy injection that arrives in the afterglow shock (in the forward shock), due to the decrease of the Lorentz factor Γ at the end of the prompt emission. The mass that is injected to the forward shock is the function of its Lorentz factor and the energy injected. As a result

the Γ increases monotonically with radius. The flux decays as a power law which depends on the mass and the energy injected (Ramirez-Ruiz et al., 2001, Rees and Mészáros, 1998, Sari and Mészáros, 2000). 2. The central engine of the source stays active for hours after the burst and injects the smooth and continuous energy at later times, several hours after the burst (MacFadyen et al., 2001, Ramirez-Ruiz, 2004, Rees and Mészáros, 2000). The difference between these two scenarios is the reverse shock, which is mildly relativistic in the first scenario and highly relativistic in the second one.

- **Normal decay (III)**: This is a phase with a decay around $1.0 < \alpha_3 < 1.5$ which was already expected before *Swift* and is consistent with the standard fireball afterglow model expanding into an ISM rather than a wind (Chevalier and Li, 2000, Mészáros and Rees, 1997, Sari et al., 1998). The explanation of this phase is related to the end of the energy injection at the external shocks that may be as the result of two different reasons: 1. The fall of the Lorentz factor of the forward shock up to the point of a minimal Lorentz factor that carries a significant initial energy or 2. The time that the central engine needs to be inactive (Granot and Sari, 2002, Sari et al., 1998).

- **Steeper decay (IV)**: This phase has a decay that is $\alpha_4 > 2$ and represents an achromatic steepening that happens due to a jet break. When the Lorentz factor of the ejecta becomes larger than θ_0^{-1} compared to the jet opening angle θ_0, the ejecta is collimated into a jet break.

- **Flares (V)**: Flares can be seen in every phase explained above (I-IV), and their shape can vary from little to very sharp. These flares cannot be explained with the external shock, therefore the best possibility is that they happened during the late internal shocks. It is thought that the central engine stays active for hours, but if we compare it to the shallow decay, here the energy injection is not continuous but episodically.

1.6   Fermi Observatory

The Fermi Gamma-ray Space Observatory is a NASA mission, launched on June 11, 2008. The goals of Fermi are:

- To study Gamma Ray Bursts, but also for high energy astrophysical phenomena in general

- To identify the composition of the dark matter

- To understand the acceleration mechanism of active galactic nuclei (AGN), pulsars, black holes and supernova remnants (SNR)

- To investigate the surrounding environment of these phenomena.

On-board the Fermi satellite there are two instruments: Gamma-ray Burst Monitor (GBM) and Large Area Telescope (LAT). GBM is fully dedicated to study GRBs in an energy range 8 keV–40 MeV (Bissaldi et al., 2009, Meegan et al., 2009). GBM has 12 sodium iodide scintillators (NaI), 2 bismuth germanate scintillators (BGO), a Data Processing Unit (DPU) and a Power Box on-board, Fig. 1.12.
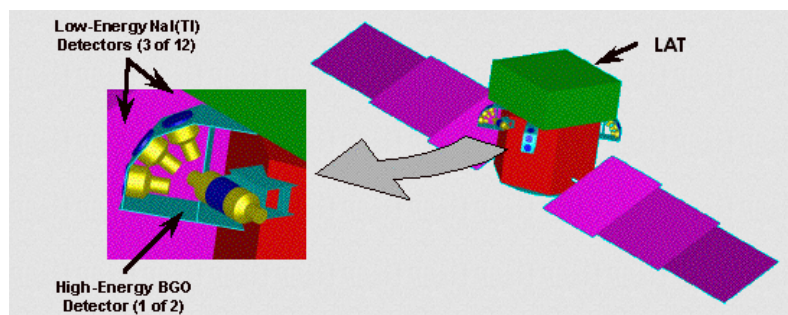
FIGURE 1.12: Fermi satellite, composed of two kinds of instruments: NaI detectors and BGO detectors. Credit: NASA/Fermi

The goals of GBM are:

- To detect GRBs from both instruments: GBM and LAT, providing in this way the analysis of spectra and the light curves

- To locate in real time a burst and to point the LAT instrument for further observation of the emission of the burst

- To quickly circulate in the community the location of GRBs, in order to follow-up from ground telescopes.

NaI

NaI detectors have an energy range of 8 keV – 1 MeV. The crystals of each NaI detector are hermetically sealed inside light-tight Aluminum housing with a glass window (see Fig. 1.13), seen by a photomultiplier tube (PMT). Whereas the crystal disks have a diameter and thickness of 12.7 cm and 1.27 cm respectively and are located on the front window side (which are packed in a reflective white cover of Tetratec) and along the perimeter (a Teflon cover).

The aim of NaI detectors is the determination of the location of GRBs.

BGO

BGO detectors have an energy range of 200 keV – 40 MeV and are positioned in the opposite sides of the spacecraft. The crystals of each BGO detector are sealed inside carbon-fiber reinforced plastic housing that is located on both sides of the Titanium ring. The crystals have a diameter and length of 12.7 cm and have two circular glass windows that are polished as mirrors with a cylindrical roughened surface. The crystals are between the two PMTs (see Fig. 1.14).
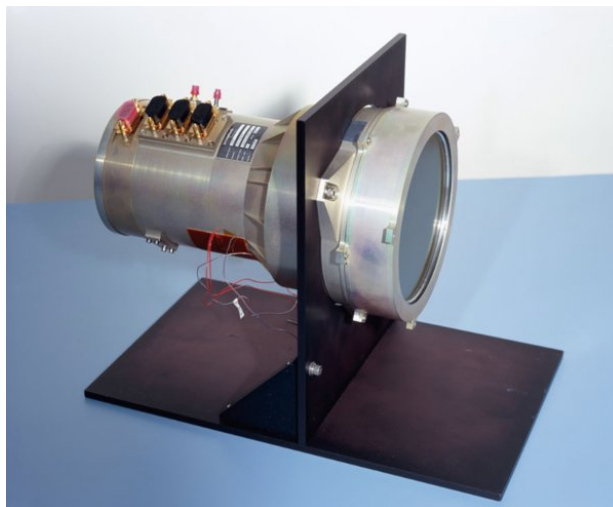
FIGURE 1.13: One of the NaI detectors. Credit: NASA/Fermi

FIGURE 1.14: One of the BGO detectors. Credit: NASA/Fermi

1.7 Theory of GRBs

1.7.1 Fireball Model

The best explanation of the physics of GRBs thus far is based on the standard model, also known as the fireball model. This model was presented by Cavallo and Rees, 1978 and by Rees and Mészáros, 1992, 1994. The mechanism of the fireball model starts with the understanding of the evolution of the bulk Lorentz factor, dependent on the time and mechanism of the creation of GRBs, considering here the prompt and afterglow emission.

The progenitors of GRBs create a huge amount of energy in a very short time and in a very small volume. In order to have this huge energy in a small volume, one should think that the beginning of the fireball consists of e^-, e^+(from pair creation), γ and a few baryons, and it should also be opaque in order to produce pair creation. These conditions make the fireball

expand relativistically ([Goodman](), 1986, [Paczyński](), 1986). If we consider that the initial radius of the fireball is R_{in}, where the bulk Lorentz factor is $\Gamma \sim 1$, then the bulk Lorentz factor will increase linearly with R until it reaches saturation, with a radius R_{sat}, $R_{sat} \sim \eta R_{in}$, where η represents the mean energy per baryon. Above the saturation radius the bulk Lorentz factor stays constant at its maximum value (see Fig. 1.15). The opacity of the fireball decreases during this time and the radius where it reaches unity is called photospheric radius R_{ph}. The radiation does not escape below this radius, whereas above it, it can. R_{is} is the beginning of the prompt emission, thus the creation of internal shock and after that the radiation of gamma emission. After that radius, the Lorentz factor starts to decrease. During the coasting phase itself, the bulk Lorentz factor remains unchanged. When the bulk Lorentz factor starts to decrease again we have the beginning of the afterglow emission, at the radius R_{es} (also called declaration radius R_{dec}). The bulk Lorentz factor decreases during the afterglow just like $\Gamma \sim R^{-3}$ for a radiative process and $\Gamma \sim R^{-3/2}$ for an adiabatic process.
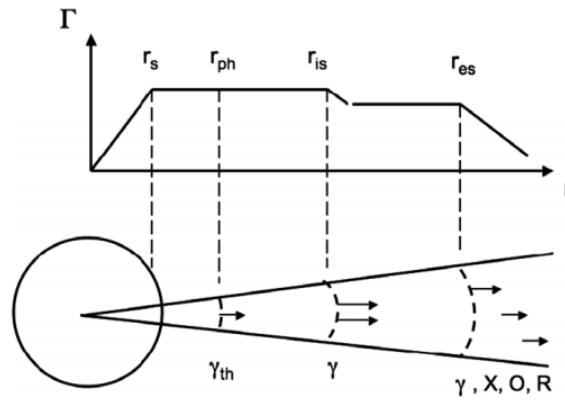
FIGURE 1.15: Schematic behaviour of the jet Lorentz factor for the fireball standard model. See the text for explanation. Credit: [Mészáros](), 2006

In terms of energy, during the first phase (before radiation of GRBs, before R_{is}), the thermal energy of the progenitors converts to kinetic energy of baryons. When the internal shocks appear beyond the photospheric radius we have the conversion of kinetic energy to a non-thermal radiation during the prompt phase (to the kinetic energy of accelerated particles). Whereas for the afterglow emission, we have two processes: a radiative and an adiabatic process. This implies that in the beginning of the afterglow we have a dissipation of the energy and in the end we have an adiabatic process.

1.7.2 Prompt emission

The emission mechanism of GRBs creates two processes, prompt emission and afterglow emission. The ultra-relativistic outflow that is created during the early phase of the fireball can generate several shells with different motions. During the movement of the shells, while the fireball has become optically thin (obvious after the photospheric radius), it is likely that a faster shell could reach a slower one. This produces a mildly relativistic shock (the internal shock) with a radiation of GRB and this kind of shock is called internal shock (Fig. 1.16). During this emission, the central engine should be active along the whole duration of the burst. The

light curves of GRBs are very variable and change from one GRB to another, without having a common rule for it. All this fast temporal variability can be well explained by the internal shocks as multiple emissions such as the sum of each emission given by every internal shock.
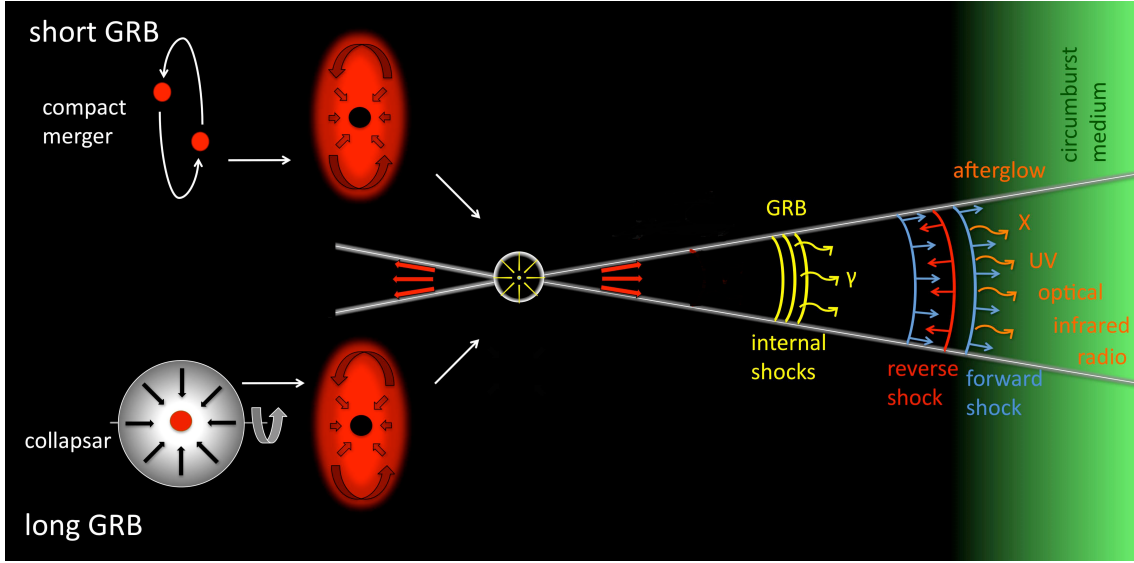
FIGURE 1.16: A schematic model of the fireball model of Gamma-ray Bursts. See the text for explanation. Credit: Gomboc, 2012

Spectral theory of prompt emission

Band et al., 1993, by analyzing 54 GRBs found an empirical law for the spectrum of the prompt emission of GRBs that is given by:

$$
N_E(E) = \begin{cases} A\left(\dfrac{E}{100\,keV}\right)^{\alpha} \exp\left(-\dfrac{E}{E_0}\right) & \text{for} \quad (\alpha - \beta)E_0 \geq E \\[2ex] A\left[\dfrac{(\alpha - \beta)E_0}{100\,keV}\right]^{\alpha - \beta} \exp\left(\beta - \alpha\right)\left(\dfrac{E}{100\,keV}\right)^{\beta} & \text{for} \quad (\alpha - \beta)E_0 \leq E, \end{cases} \tag{1.1}
$$

where A is the normalization, α and β are the photon spectrum indices in low and high energy respectively and their typical values are around $\alpha = 1$, $\beta = -2.3$. and $E_0 = 150\,keV$. The transition between the low and the high part of the spectrum is defined as $E_p = E_0(\alpha - \beta)$, where the E_{peak} (or E_p) is the peak of the spectrum and is calculated as $E_0(2 + \alpha)$. As seen in the Fig. 1.17, this spectrum presents the emitted power per energy, and usually reaches the maximum at a few MeV. This model is known as the Band model or simply as the GRB model. This is a non-thermal spectrum which is in agreement with the expectation of the theory.

1.7.3 Afterglow emission

When the outflow slows down in the external medium, the shells interact with the surrounding medium at the later times, thus creating at this moment the radiation in different wavelengths. This late radiation is called afterglow radiation and the shocks which created it are called
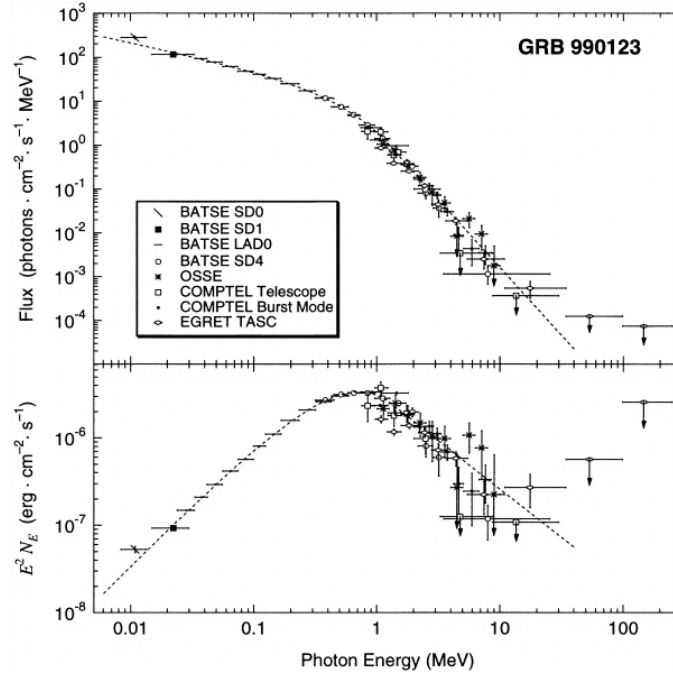
FIGURE 1.17: The presentation of the Band model for prompt emission for GRBs. The spectra are taken from CGRO detectors. Credit: Briggs et al., 1999

external shocks. The external shocks are categorized as two different types of shocks: a forward shock that propagates in the surrounding medium and a reverse shock that propagates into the ejecta (Fig. 1.16). Usually for lGRBs, the afterglow happens while GRB itself is still occurring. The physical mechanism that creates prompt and afterglow emissions is considered to be a Synchrotron Radiation and/or Inverse Compton Scattering (ICS).

Synchrotron radiation

Synchrotron radiation is created when charged particles move quickly inside a magnetic field. The movement of the particles during the synchrotron radiation is a spiral, meaning that the vectors of motion and the acceleration are perpendicular to each other. The synchrotron frequency ν_{syn} and the synchrotron frequency in the observer frame $\nu_{syn}(\gamma_e)$ are (Rybicki and Lightman, 1979):

$$
\begin{aligned}
\nu_{syn} &= \frac{q_e \mathbf{B}}{2\pi m_e c \gamma_e^2}, \\
\nu_{syn}(\gamma_e) &= \mathbf{\Gamma}\,\nu_{syn} \\
&= \frac{q_e \mathbf{B}}{2\pi m_e c \gamma_e^2 \mathbf{\Gamma}},
\end{aligned}
\tag{1.2}
$$

where the γ_e is the Lorentz factor of the relativistic electrons that also represents the electron energy, $\mathbf{B}$ is the strength of the magnetic field, $\mathbf{\Gamma}$ is the Lorentz factor of the emitting material and q_e and m_e are the charge and the mass of the electron. While the time of synchrotron

radiation is:

$$t_{syn} = \frac{3m_e c}{4\sigma_T \mathbf{U_B}\gamma_e} \frac{1}{\mathbf{\Gamma}} \quad \Rightarrow \quad t_{syn} \propto \gamma_e^{-1}\mathbf{\Gamma}^{-1}, \tag{1.3}$$

where the σ_T is the Thompson cross-section and $\mathbf{U}_B$ is the magnetic energy density which is equal to $B^2/8\pi$. By replacing γ_e in the Eq. 1.3 from the Eq. 1.2 we find out:

$$t_{syn} \propto \nu^{-1/2}\mathbf{\Gamma}^{-1/2}. \tag{1.4}$$

Blandford and McKee, 1976 proposed the density and the energy density of particles which are accelerated behind a relativistic shock, which by itself propagates in a uniform cold medium with a density n: 4γ and $4\gamma^2 n m_p c^2$ for particle density and energy density, respectively. By following this idea Sari et al., 1998 assumed that the acceleration of the electrons inside this shock should be done as a power law distribution ($N(\gamma_e) \propto \gamma_e^{-p}$ for $\gamma_m < \gamma_e$, but with a minimum Lorentz factor that is given by the formula:

$$\gamma_m = \epsilon_e \left(\frac{p-2}{p-1}\right)\frac{m_p}{m_e}\Gamma \quad \text{while} \quad \nu_m \equiv \nu_{syn}(\gamma_m), \tag{1.5}$$

where ϵ_e is a constant fraction of the shock that goes into the electrons. We should consider that in order to have an infinite energy for electrons, the spectral index should be $p > 2$.

While the total radiation power of the synchrotron emission is:

$$P_{syn} = \frac{4}{3}\sigma_T c \mathbf{U}_B \gamma_e^2, \tag{1.6}$$

and the power reaches the maximum at:

$$P_{\nu,max} \approx \frac{P_{syn}}{\nu_{syn}(\gamma_e)}$$
$$= \frac{m_e c^2 \sigma_T}{3q_e}\mathbf{\Gamma B}, \tag{1.7}$$

that is not dependent on γ_e. Sari et al., 1998 put forth the need of a critical factor γ_c, where it should be bigger than γ_e, given by the formula:

$$\gamma_c = \frac{6\pi m_e c}{\sigma_T \mathbf{\Gamma B}^2 t}, \tag{1.8}$$

where t is the time in the observer frame.

Then Sari et al., 1998 based on a $\gamma_c \equiv \nu_{syn}(\gamma_c)$ for electrons that cool down to γ_c, proposed the idea of the net spectrum radiation as three power law segments. The emission before the peak of the spectrum corresponds to the low-energy part of the spectrum, and this part is well known as a characteristic of the synchrotron emission, meaning that the Flux is $F_\nu \propto \nu^{1/3}$ (see Fig. 1.18). Also, the latest part of the emission corresponds to the part where the most energetic electrons at their synchrotron frequency emit all their energy $\gamma m_e c^2$, making the Flux, $F_\nu \propto \nu^{-p/2}$ (see Fig. 1.18). Whereas the peak of the spectrum that corresponds to the intermediate frequencies depends on the cooling regime: fast or slow cooling (see Fig. 1.18).

Fast cooling   This case happens when all the electrons are cooling rapidly so $\gamma_c < \gamma_m$. Hence the observed flux F_ν is given by (Sari et al., 1998):

$$F_\nu = \begin{cases} (\nu/\nu_c)^{1/3} \, F_{\nu,max} & \text{for} \quad \nu < \nu_c \\ (\nu/\nu_c)^{-1/2} \, F_{\nu,max} & \text{for} \quad \nu_c < \nu < \nu_m \\ (\nu_m/\nu_c)^{-1/2}(\nu/\nu_m)^{-p/2} \, F_{\nu,max} & \text{for} \quad \nu_m < \nu, \end{cases} \tag{1.9}$$

where $F_{\nu,max} = N_e(P_{\nu,max}/4\pi D^2)$ is the observed peak flux from a source at a distance D. The peak flux is at ν_c while the peak energy emitted is at ν_m.

Slow cooling   This case happens when only the electrons with $\gamma_c < \gamma_e$ can cool, while the electrons with $\gamma_c \sim \gamma_e$ cannot cool. The observed Flux F_ν of this case is given by:

$$F_\nu = \begin{cases} (\nu/\nu_m)^{1/3} \, F_{\nu,max} & \text{for} \quad \nu < \nu_m \\ (\nu/\nu_m)^{-(p-1)/2} \, F_{\nu,max} & \text{for} \quad \nu_m < \nu < \nu_c \\ (\nu_c/\nu_m)^{-(p-1)/2}(\nu/\nu_c)^{-p/2} \, F_{\nu,max} & \text{for} \quad \nu_c < \nu. \end{cases} \tag{1.10}$$

During this time the peak flux is at ν_m while the peak energy emitted is at ν_c. A self-absorption frequency (ν_a), is also needed, where the limit of the opacity is located. During this time, the absorption also becomes negligible due to the fireball. Above this frequency the fireball starts to be transparent, while prior to this, it is still optically thick. All the previous description is given schematically in the Fig. 1.18.
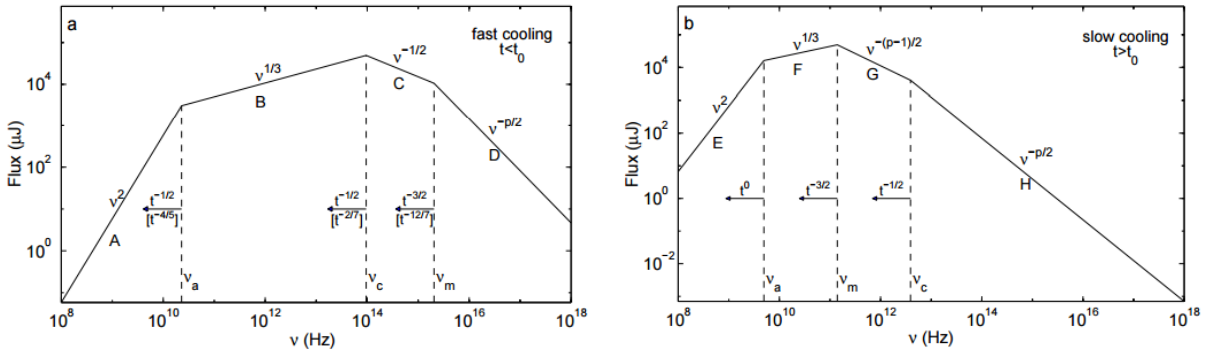
FIGURE 1.18: Credit: Mészáros, 2006

Closure relation

Following this idea Panaitescu and Kumar, 2000a, found different relations between temporal and spectral analysis. These relations analytically display the progenitor of GRBs. The GRB surrounding medium is another parameter providing a clue about their progenitor. If the surrounding medium is homogeneous, then the progenitor of GRBs is the merger of two compact objects, whereas if the surrounding medium is a wind ejected by the star that decreases with distance, then the progenitor is the collapse of a massive star.

By doing all the calculations, Panaitescu and Kumar, 2000a found the relations for homogeneous external medium in the fast and slow cooling. The fluxes of $F_\nu \propto \nu^{-\beta} t^{-\alpha}$, vary as:

<div align="center">

Homogeneous external medium s = 0

</div>

Fast cooling   Slow cooling

$$F_\nu \propto \nu_{9.7}^2 \, t_{d,-1} \tag{1.11}$$

$$F_\nu \propto \nu_{14.6}^{1/3} \, t_{d,-2}^{1/6} \tag{1.12}$$

$$F_\nu \propto \nu_{9.7}^2 \, t_{d,1}^{1/2} \tag{1.15}$$

$$F_\nu \propto \nu_{14.6}^{-1/2} \, t_{d,-2}^{-1/4} \tag{1.13}$$

$$F_\nu \propto \nu_{14.6}^{1/3} \, t_{d,-2}^{1/2} \tag{1.16}$$

$$F_\nu \propto \nu_{14.6}^{-p/2} \, t_d^{-[(3p-2)/4]} \tag{1.14}$$

$$F_\nu \propto \nu_{14.6}^{-[(p-1)/2]} \, t_d^{-[(3/4)(p-1)]} \tag{1.17}$$

$$F_\nu \propto \nu_{14.6}^{-p/2]} \, t_d^{-[(3p-2)/4]} \tag{1.18}$$

<div align="center">

Wind external medium s = 2

</div>

Fast cooling   Slow cooling

$$F_\nu \propto \nu_{9.7}^2 \, t_{d,-1}^2 \tag{1.19}$$

$$F_\nu \propto \nu_{14.6}^{-[(p-1)/2]} \, t_d^{-[(3p-1)/4]} \tag{1.23}$$

$$F_\nu \propto \nu_{12}^{1/3} \, t_{d,-1}^{-2/3} \tag{1.20}$$

$$F_\nu \propto \nu_{17.5}^{-p/2} \, t_{d,-1}^{-(3p/4)+\{p/[2(4-p)]\}} \tag{1.24}$$

$$F_\nu \propto \nu_{9.7}^2 \, t_{d,-1}^1 \tag{1.21}$$

$$F_\nu \propto \nu_{12}^{1/3} \, t_d^0 \tag{1.22}$$

1.8   The well-known correlations

Since the first discovery of GRBs different scientists independently from one another, found different correlations. In this section, I will indicate only correlations that are necessary in understanding the research that is explained in the following chapters. The range of the correlations explained here is from a significant range during my PhD study.

Amati relation

The first observations taken from BeppoSAX, Amati et al., 2002, took into account only GRBs with known redshift and considered the Band model as the typical model for characterizing the prompt emission of GRBs, and studied the intrinsic properties of GRBs. They found a tight correlation between the E_{peak}, the peak energy of the spectrum of GRBs, that reaches the peak at $E_p = E_0(2 + \alpha)$ and the E_{iso}, the isotropic energy that a GRB radiates during the prompt emission. This correlation is well known as "Amati relation". It was confirmed by many GRBs observed by different instruments (Amati, 2003, 2006, Lamb et al., 2004, Sakamoto et al., 2004)

but also extended in X-ray Flashes (XRFs) by (Sakamoto et al., 2006). Different authors have found other derivatives of this correlation as $E_{p,i}$-L_{iso} (Lamb et al., 2004, 2005) and $E_{p,i}$-$L_{p,iso}$ (Ghirlanda et al., 2005, Yonetoku et al., 2004). The significance of this correlation has been improved each time. The mathematical equation that gives this relation is given by:

$$E_{p,i} = K \times E_{iso}^m, \tag{1.25}$$

where K is the normalization, m is the power law index and the units of $E_{p,i}$ is in keV and E_{iso} is in $10^{52}\, erg$.

An example of the constants and the $E_{p,i} - E_{iso}$ plane will be given in Chapter 3.

Dainotti correlation

Using the *Swift* data, Dainotti et al., 2009 found a correlation between X-ray Luminosity ($L_X(T_a)$) and the time (T_a, in the rest frame) which corresponds to the time of the end of the plateau phase by following the procedure explained by Willingale et al., 2007. Luminosity at a given time t, is given by:

$$L_X(t) = 4\pi D_L^2 F_X(t) \cdot k, \tag{1.26}$$

where D_L is the distance luminosity given by formula (Pen, 1999):

$$D_L(z) = \left(\frac{c}{H_0}\right)(1+z)\, d_L(z)$$

$$\text{and} \tag{1.27}$$

$$d_L(z) = \int_0^z \frac{dz'}{\sqrt{\Omega_M(1+z')^3 + (1 - \Omega_M)}},$$

where c is the speed of light, assuming a flat universe with a Hubble constant H_0 and a parameter Ω_M. k is a correction of the cosmological energy shift (Bloom et al., 2001, Lamb and Reichart, 2000). By considering all the parameters and making all the pertinent calculations and approximations Dainotti et al., 2009, reached the point that the luminosity and the flux observed at the time T_a are:

$$L_X^* = \frac{4\pi D_L^2(z) F_X}{(1+z)^{1-\beta a}}$$

$$F_X = F_a \exp\left(-\frac{T_p}{T_a}\right), \tag{1.28}$$

where T_p is the transition time of the prompt emission (Willingale et al., 2007). This correlation was confirmed again by Dainotti et al., 2010 and calculated with a better precision by Dainotti et al., 2013 by considering this time the bias effect. Conclusively, the Dainotti correlation is given as: $L/(1+z)^{-0.05}$ - $T_a/(1+z)^{-0.85}$ (Dainotti et al., 2013).

1.9 How correlations are naturally presented into the model?

Almost all the correlations related with GRBs have the same aim: standardization of GRBs as cosmological tools. Every observer has attempted to find new correlations, linking in this way different parameters that came from observations. Some of them have theoretical meaning and some give new evidence or confirm the physics process of GRBs and their subclasses. The achievement of the standardization of GRBs will bring us the certainty of the cosmological parameters. All the authors that are indicated in the previous section had this goal, but until recently, none of them were able to prove the standardization of GRBs. The physics behind these correlations will allow us to go further in the emission mechanism of GRBs, and try to better understand it and reply to all the open questions in the GRB physics (Zhang, 2011). Some of these correlations were estimated to be used as a redshift indicator for GRBs with unknown redshift (Atteia, 2003), but the validity of this property is still under debate.

The idea of starting this project is precisely related to the standardization of GRBs as a cosmological tool and reaching further in the progenitors of different groups of GRBs. Thanks to fast capabilities and multi-wavelength instruments of *Swift* satellite, there are numerous GRBs observed thus far. The idea of this study, started as the continuation of a work on the Boër & Gendre relation (Gendre et al., 2008a). The first idea was to independently confirm the relation and to check for any inconsistency. During the *Swift* Era, the X-ray afterglow was completely explainable, and as a result the study of this relation went further, by studying this time the distribution of the luminosity at a given time. However, the conclusions of these works point toward no clustering in various groups, but instead in a loose and broad distribution (see for instance Melandri et al. (2014) for one of the latest of these works).

The work related to the data analysis would bring different ideas of new correlations. The first idea, related to the clustering of X-ray afterglows, diminished on the way, but opened other issues related to the data processing. We describe different problems that can go through due to an incorrect data analysis process by confirming that a manual data analysis can be different from automatic ones. Some are discussed in the hint of instrumental problems, by following the question: Do the instruments observing GRBs follow the same rules during an entire year?

The universe is constantly observed, providing us with information about different objects. On December 21, 2014, TAROT observed a peculiar GRB 141221A. This GRB was so bright in the optical part, making it a peculiar GRB. With all the data collected, it was worth undertaking an observational study for this GRB and letting free the theoretician to deeply search into other properties.

Chapter 2

Data analysis

2.1 Gamma-Ray data

2.1.1 Methods of detection

BAT/*Swift*

The BAT instrument onboard the *Swift* spacecraft is dedicated to the observation of gamma-rays and is based on two operation systems: scan-survey mode and the burst mode (Barthelmy et al., 2005). For the detection of a burst, BAT passes through two processes: 1. the burst trigger algorithm and 2. the image and location of the burst. After being sure that it has located a GRB, BAT produces the data of the burst. Since BAT monitors the sky continuously, it surveys for hard-x-ray transients as well.

When the trigger algorithm detects an event which increases the count rate on the detector plane, above the rate of the background and constant sources, it starts to compare it with the catalog that is on board. This catalog contains $32\,768$ different values as an on-board map of the detector plane. This comparison contains different steps, such as:

- The background intervals, that can be between 1 and $100\,\mathrm{sec}$

- The law of the extrapolation of the background such as: constant, linear and parabolic with time

- An interval test of the burst duration that is between $4\,\mathrm{msec}$ and $32\,\mathrm{sec}$, which is called the rate trigger

- The illuminated region of the detector plane

- 4 bands pass test in order to find the energy range for this event

This whole process does not take more than $5\,\mathrm{sec}$. After the algorithm validates the trigger, it sends the information and in the following $12\,\mathrm{sec}$ it generates an image, with a dimension

1024x512 pixels. To be sure that this is not a false trigger, the last check is to see the peak of this image. In case that the peak is compatible with a burst source, then the position of the burst inside a 14 arcmin sky pixel is determined. If there is no pixel to show that, then the information goes as a false trigger. This peak gives the location of the burst within an error of 1–4 arcmin (the size depends on the flux of the burst). Thus the burst trigger has started and the detection of the burst continues. Meanwhile, BAT sends the location of the burst in right ascension and declination with an error circle of 4 arcmin within 20 sec to the ground. This information is relayed thanks to the GCN Networks (Barthelmy et al., 2005).

Fermi

The Fermi satellite monitors the entire sky continuously, but the moment that it detects an increase of the count rate for two or more NaI detectors, compared to the usual background starts triggering that burst. The first observation starts from the GBM instrument and after 2 sec it is followed by LAT. After the detection of the burst its direction is determined by using the relative rates of NaI detectors by comparing them to the relative rates of 1634 directions that are in the spacecraft. The spacecraft coordinates are then converted into the right ascension and declination for the direction that has the best χ^2 fit. In real time the trigger information taken by GBM is transferred to the ground, in order that the ground telescopes continue the follow-up of the burst. This transfer is referred to as TRIGDAT data that contains the information of on-board localization, the background rates, the intensity of the burst and the hardness ratio. The trigger algorithm of GBM defines two phase timescales that overlap at half of the accumulated time, between 16 msec and 8.192 sec (above the 16 msec, since the 16 msec is called as offset). Whereas the energy range for the trigger algorithm includes 4 energy ranges: 50–300 keV, 25–50 keV, > 100 keV and > 300 keV (Meegan et al., 2009).

The GBM detector is constructed in a way that it cannot detect a burst with an angle larger than 60 degree. The data collected from the GBM are three different kinds:

- **TTE**: These are time tagged data consisting of individual events which are tagged with a time arrival that consists in a resolution $2\,\mu$s, energy with 128 channels and detector number. This kind of data is taken during the burst.

- **CTIME**: These files generate continuous information for the data with a high time resolution with an average time of 0.25 sec and an energy around 8 channels.

- **CSPEC**: These files generate continuous information for the data with a high spectral resolution with an average time of 4.096 sec and an energy around 128 channels.

2.1.2   Methods of analysis

Spectral analysis for GBM data can be done by using the standard tools provided `RMFIT`[1] and `FTOOLS`[2].

---

[1] http://fermi.gsfc.nasa.gov/ssc/data/analysis/rmfit/
[2] https://heasarc.gsfc.nasa.gov/ftools/

Firstly, it is necessary to download the data from the Fermi GSFC Data Center[3]. The downloaded data are different, which correspond to TTE, CTIME and CSPEC data.

TTE, CTIME and CSPEC data are given in these formats:

<div align="center">

`glg_tte_nx_bnyymmddfff_v0y.fit`

`glg_tte_nx_bn141221338`[4]`_v0y.fit`

`glg_tte_bx_bn141221338_v0y.fit`

`glg_lc_nx_bn141221338_v0y.gif`

`glg_cspec_nx_bn141221338_v0y.pha`

</div>

- **glg** represents the data from GBM detector

- **tte** represents the file that contains TTE data

- **lc** represents the file that contains CTIME data

- **cspec** represents the file that contains CSPEC data

- **nx** represents the corresponding number of the NaI detector, n for NaI and x can be between 0-9 and after that a and b

- **bx** represents the corresponding number for the BGO detector, b for BGO and x can be from 0-1

- **bnyymmddfff** represents the Fermi trigger name for every burst which is given in the format year (yy), month (mm), day (dd) and fraction of the day (fff)

- **v0y** is a version number of the file and can be different for different types of data

- **.fit** is the extension for a fit file

- **.gif** is the extension for a figure file

- **.pha** is the extension for a spectrum file.

The response files are located in the downloaded folder, with the extension `.rsp`. Whereas for spectral analysis, we should use the `tte` files.

Spectral analysis for Fermi data should be performed with the `RMFIT` program. After the selection of the necessary file, `rmfit` will open a window that shows a light curve. The window contains in addition several options and commands which are necessary for further steps.

The selection of the event file is done accordingly to the best oriented GBM detection, information that can be found by simply checking the raw light curves.

The raw light curves are automatically extracted with an origin of time set to the trigger time. Ongoing analyses are performed with time intervals based on the study, but first we check for

---

[3]http://fermi.gsfc.nasa.gov/ssc/data/access/

[4]Fermi trigger number for GRB 141221A

any previous time triggering data. In addition, the background extraction is established on an interpolation based on the observation before and after the burst. The background selection is also highly sensitive, as it can remove too much signal, thus modifying the measured flux. For this reason, a manual inspection has to be performed. The program allows for a custom selection of the fitting regions, thus reducing this potential weakness of the analysis using the `fit background` option.

Another important step for spectral analysis is the selection of the spectral range. The energy range depends on the instrument that is used to observe the burst, but from the aim of the study as well. The GBM instrument, on-board of Fermi satellite, is sensitive on the energy band 8–900 keV. Hence, the energy should be filtered on this energy range, by simply using the option `toggle`.

After completing all the previous steps, which are important for the fitting of the spectrum, the last step is to plot and to fit the spectrum. The fitting model depends on the interest of the study, as explained in Chapter 1 Section 1.7, the classical model of the prompt emission. The different models are available in the option `Spectral Fitting`, by changing the parameters of each model according to the study.
BGO 00 detector should be used for the 1-5 NaI detectors and GBO 01 detector should be used for the 6-12 NaI detectors.

2.2 X-ray data

2.2.1 Methods of detection

XRT/*Swift*

The observation of the burst continues after the BAT trigger with the XRT and UVOT instruments. XRT is dedicated to the rapid follow-up of the X-ray counterpart of the burst, in order to find a highly accurate position of the burst and to measure the light curve and spectrum in the X rays. Thus the XRT observation is based on 4 different modes, depending on the flux of the source. These modes are (Hill et al., 2004):

- **Imaging Mode (IM)**: It is the first mode selected when the space localization detects a target, to determine the location of the GRB with pronounced accuracy. The location of the burst is determined by using a centroiding algorithm that consists of two phases. The first phase identifies the wings of the burst by using a window on an isolated pixel above the lowest level discriminator and below the upper level discriminator. During this phase, the cosmic rays can also be identified and filtered out. On the second phase, this window slide until it reaches the center of the source. Due to an increase of count rates from the edge towards the core on the X-rays, this phase allows to find the center of the burst with an accuracy of about 2.5 arcsec, while the size of the window is 50x50 pixels (see Fig. 2.1). The location of the burst is determined for GRBs with a Flux range between 23 mCrab and 37 Crab.

- **Photodiode mode**: It is a mode designed for very bright sources with very high time resolution (0.14 ms). This mode alternatively uses one serial and parallel clock shifts and as a result we have a particularly rapid clocking of each pixel across the CCD. This is firstly done by clocking a row of pixels from the whole CCD into a serial register, with the limit that every row should be around 45 μsec and after that clocking a serial register (6.6 μsec) into the output of the mode. This process of transferring each row into a pixel, continues for every row.

  The Photodiode mode can produce a high resolution light curve and spectrum, and is designed for the beginning of the observation of the GRB, when the flux is high and the limit of flux is 60 Crab. According to the telemetry format, two sub-modes can operate: Piled-up (PU) and Low Rate (LR). In piled-up mode all pixels are sent down in a highly efficient way, while in Low rate mode only pixels above lower level discriminator are sent down. This mode has not worked from May 27, 2005.

- **Windowed Timing mode (WT)**: This mode gives the information in 1D while one single CCD row is the sum of 10 CCD rows and it can read out only the center of 200 columns of a CCD thus showing 8 arcmin of FoV. The resolution of this mode is very high (1.7 ms) and the flux limit is 600 mCrab (200 ct/s).

- **Photon Counting mode (PC)**: It is a 2D spatial information and in each single pixel we have the information of the total charge accumulated in that pixel. This mode does not have a very high time resolution (2.5 s) and the flux limit is 1 mCrab (0.5ct/s).

Phase 1 of the algorithm – Identification of the wings of the PSF.

Phase 2 – The iterative procedure moves the window from the wings of the PSF to the centroid of the Point Source
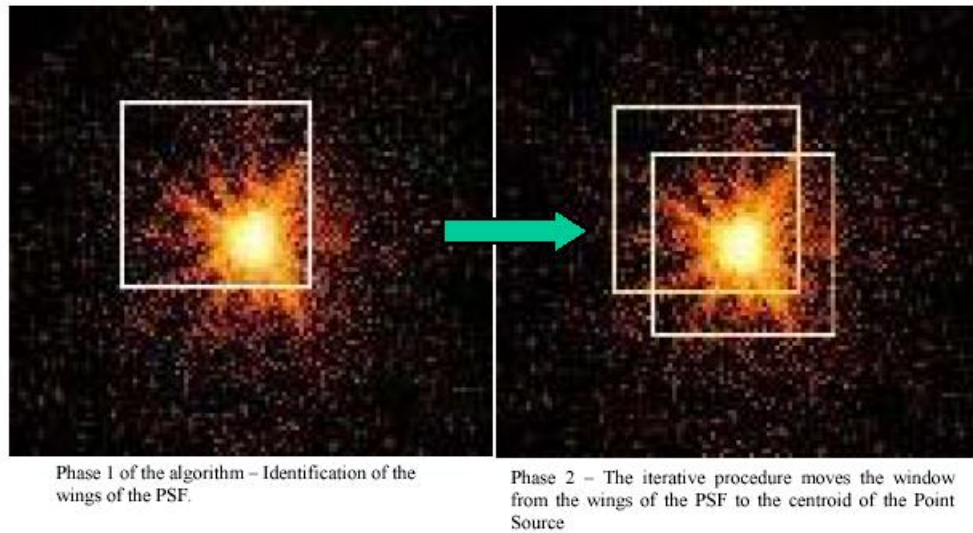
FIGURE 2.1: Centroiding Algorithm from XRT. Credit: NASA/*Swift*

The full detection of a single GRB can last for around one month. The monitoring of a target for such a long time consists of different observations that can last up to 2 days. One single observation is made of a group of snapshots. A snapshot is the minimum time needed to continuously observe a target and it can last up to 95 minutes (shorter than an orbit). The collection of all the observations together for the same target is called monitoring campaign. An example of snapshots and observations are given in the Fig. 2.2.
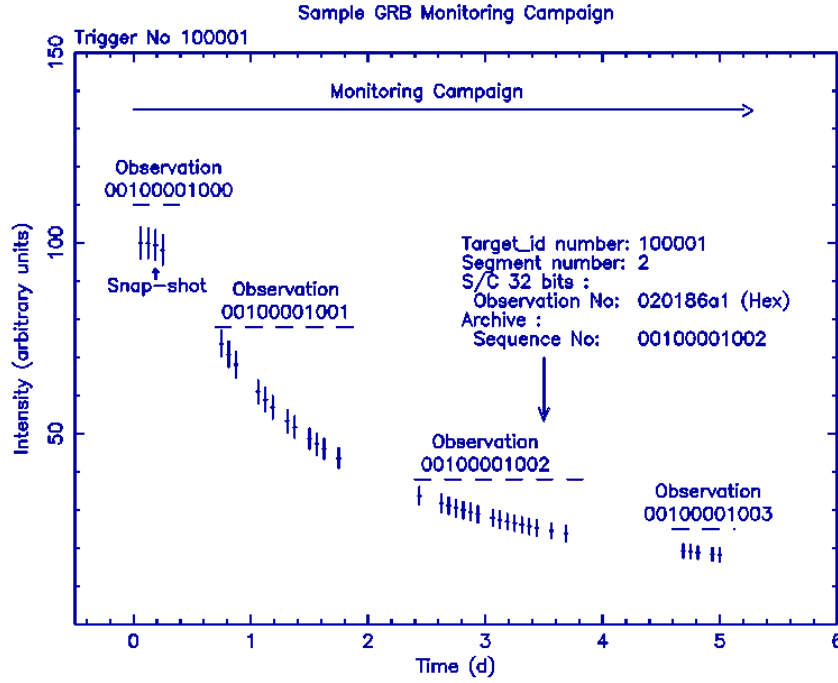
FIGURE 2.2: GRB monitoring campaign. Credit: NASA/*Swift*

2.2.2 Pile-up

Nowadays, the X-ray instruments use CCD (Charge-Coupled Device) detectors, which are constructed from semiconductors. CCD divides into pixels, where each pixel collects one charge (the charge which is liberated from the incident X-ray photon). In order to readout the charges collected into a CCD, they are transferred along a row, which is transferred down, if a row is empty. The quantum efficiency of this transfer must be more than 99.99%.

In X-ray astronomy, due to the increase of the efficiency of the instruments, the observation of bright sources has happened often, but sometimes it makes these sources pile-up. Pile-up happens when more than one x-ray photon is registered in a single pixel on a CCD. As a result, the total charges from the x-ray photons will be counted as one. The effects of pile-up are:

1. The loss of flux because the photons are read as one instead of several, therefore we will have the loss of photons thus the loss of flux

2. The increase of energy due to the overlap of photons

3. The distortion of the energy.

The way of checking and correcting the pile-up sources is explained in Vaughan et al., 2006. The flux loss due to the pile-up has been studied from (Ballet, 1999). Vaughan et al., 2006

numerically computed the significance of the pile up for different count rates. They assumed for a non-piled-up PSF[5] a King function (Eq. 2.1):

$$g(r) = \frac{\beta/2 - 1}{\pi r_0^2}(1 + (r/r_0)^2)^{-\frac{\beta}{2}},\tag{2.1}$$

where: $r_c = 6.49''$ and $\beta/2 = 1.59$ as measured for the XRT at $1.49\,\mathrm{keV}$. After the calculation they found that for low count rates $< 0.1\,\mathrm{count/sec}$ the efficiency is $\sim 99\%$ thus the loss is $\sim 1\%$ and for $1\,\mathrm{count/sec}$ the efficiency is $\sim 80\%$ thus the loss is $\sim 20\%$ (see Vaughan et al., 2006 for more details).

Vaughan et al., 2006 did a test with a mono-pixel event by examining the X-ray image as a function of the observed count rate. They created a light curve for each event, by using a bin size of $25\,\mathrm{s}$ and by defining three time intervals: a) "bright" time, when the observed count rate of the source was $> 5\,\mathrm{ct/s}$; b) "intermediate" time, when the count rate was $1\text{–}5\,\mathrm{ct/s}$; and "faint" time, when the count rate was below $< 1\,\mathrm{ct/s}$ that cover $60\,\mathrm{s}$, $113\,\mathrm{s}$ and $12.15\,\mathrm{ks}$ of exposure, respectively. An X-ray image was formed for each time interval and a radial profile was calculated and was compared with an analytical PSF model and constant background. For comparison with measured radial profiles, the two models were integrated in annuli by using the following formula:

$$M(r_{in}, r_{out}) = \int_{r_{in}}^{r_{out}} \left[N\left\{1 + (\frac{r}{r_c})^2\right\}^{-\beta/2} + B \right] 2\pi r\,dr,\tag{2.2}$$

where: $\left[N\left\{1 + (\frac{r}{r_c})^2\right\}^{-\beta/2} \right]$ represents the King profile PSF, B - the constant background level and r_{in} and r_{out} the inner and outer radius of the source.

Various tests were performed, by fitting the radial profiles of sources where the radius was an annulus. These tests were done for the faint, intermediate and bright cases. Another test was done for the effects of pile up, while the data this time were not divided into count rates but into flux intervals. In all the cases of the model fitting was used C-statistics (Cash, 1979).

All these tests reach the same conclusion: If a source is not piled up and bright, the extraction of the region should be 25 pixels (60") radius. A source is considered as piled-up, when the count rate is higher than $0.8\,\mathrm{ct/s}$, where the convergence between the corrected and uncorrected count rate for a pile-up source begins (see Fig. 2.3). After that, the correction is different for different levels of pile-up:

- An annulus region with 15 and 25 pixels should be used as inner and outer radius for the source with the count rate higher than $5\,\mathrm{ct/s}$.

- An annulus region with 9 and 25 pixels should be used as inner and outer radius for the source with the count rate between $1\text{–}5\,\mathrm{ct/s}$.

For cases where the count rate of the source is smaller than $1\,\mathrm{ct/s}$, a circular region should be used (the effect of pile-up begins to be effective above $0.8\,\mathrm{ct/s}$), thus the difference between

---

[5]the PSF describes the spread of photons around its position for a point source

0.8–1.0 ct/s is considered as a weak effect of pile-up. Any time that the extraction was performed with an annulus as a region, a normalization for counting the losses of the PSF was also performed. All the results are given in the Fig. 2.3, by showing the effect of pile-up as a function of source intensity.
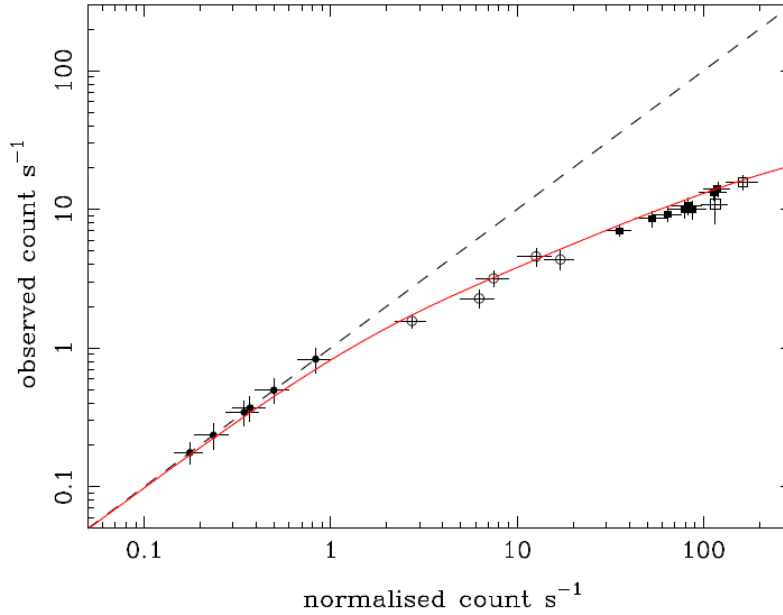
FIGURE 2.3: The relation between corrected and uncorrected count rate. The x-axis shows the situation of correction of pile-up by choosing an annulus region and on the y-axis the situation of a circle region. The dashed curve shows the expectation if a source is not piled-up and the solid curve shows the relation between mono-pixel count rates with and without pile-up, completed theoretically. Credit: Vaughan et al., 2006

2.2.3 Basic analysis

The basic of X-ray analysis is almost the same for every instrument on-board of different satellites. Here it will be explained in detail the way that is used by the XRT instrument on-board of the *Swift* satellite.

XRT

Different instruments that are on-board (e.g. FoM, on-board command and data handling) create different messages for each BAT trigger and send them to the ground via TDRSS. TDRSS broadcasts these messages within minutes via Gamma-Ray Burst Circular Network (GCN). GCN[6] is access free and after taking the information of a trigger, it will broadcast it in the network and the trigger will be followed from the ground telescopes. Fig. 2.4 shows a way of this broadcast from satellites to ground telescopes.

---

[6]http://gcn.gsfc.nasa.gov
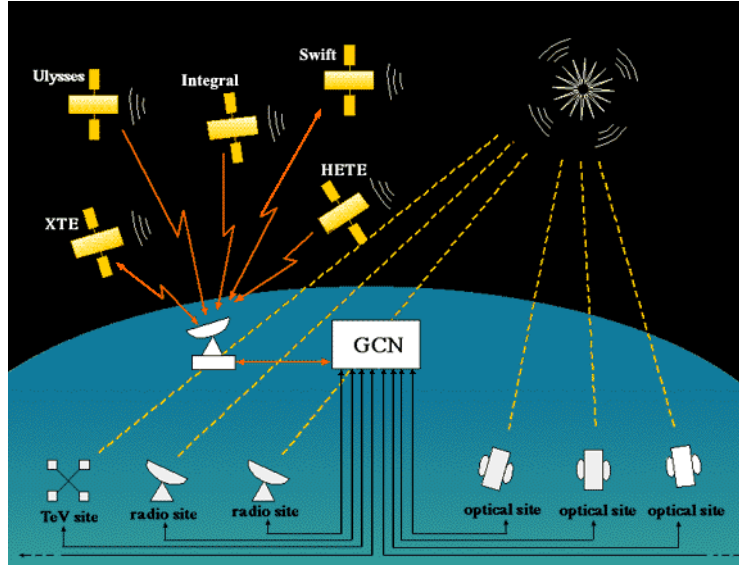
FIGURE 2.4: GCN network. Credit: NASA/*Swift*

After that the whole telemetry is sent to Malindi Ground Station and then all the data is processed at the Science Data Center (SDC) which produces the quick-look data and final archive data. When the processing of all data is completed and for almost one week it has no new processing, the quick-look data are removed from the quick-look area, meaning that at this time the observation is complete. Hence, the data are sent to the *Swift* archive at the HEASARC and in the European archive located in Italy and the UK. These archives are the places where we can download the data for a certain GRB and keep going with the data analysis process. All the XRT data analysis will be explained in detail in the following steps.

Bad columns

A few months after the launch of the *Swift* satellite, on May 27, 2005, the XRT CCD was hit by a micrometeorite. In this case the result was a few hot columns in the CCD, which have been masked out in order to prevent saturation of the telemetry. Another bad effect of this micrometeorite was the disability of the Photodiode mode, due to the way its CCD is read out.

A bad column is a dead column, which does not read the photons which have been collected on the pixels located on its position. Some of these bad columns are close to the center of the field of view (DETX: 291-294 for PC, 391-295 for WT and 319-321 for PC and WT). To see the bad column, the image should be plotted in detector coordinates or in sky coordinates but only for a single orbit at a time (see Fig. 2.5). This means that, it is possible that some GRBs are on top or exceedingly close to the bad columns, which can affect some loss of the count rates and thus the loss of the flux. Hence, during the extraction of light curves and spectra, it is necessary to correct the loss of the counts, by creating an exposure map and by using it during the spectral and/or temporal analysis.
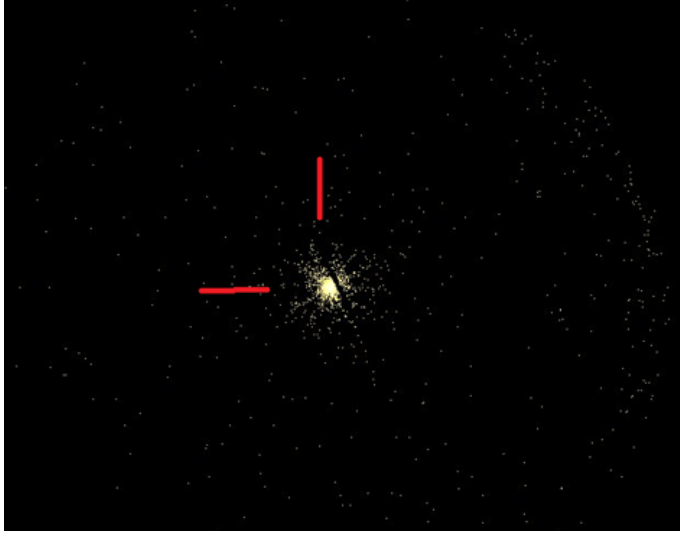
FIGURE 2.5: The image of GRB 141221A in XRT and a bad column that is passing near the center

Data reduction

Data received from the XRT instrument on-board of *Swift* that are sent to the Malindi Ground Station via telemetry dumps (TDRSS) are called Level 0 files (Fig. 2.6). These data are used to create Level 1 - FITS files at the Science Data Center (SDC), which contain: images and data from the XRT, but also from BAT and UVOT. Then these FITS files are sent through the pipeline which outputs different levels of science data (Level 2 files). The calibration of the data is done through a process that is completed through a pipeline, and consists of three main stages (Capalbi et al., 2005):
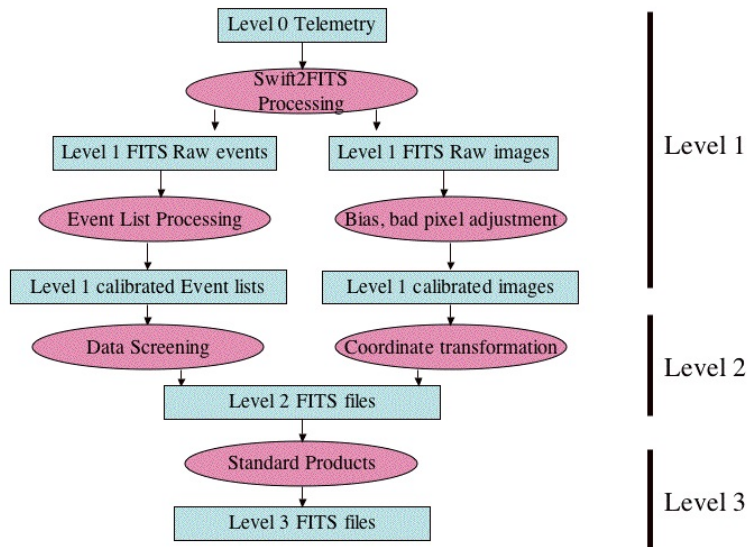
FIGURE 2.6: The different levels of `xrtpipeline`. Credit: NASA/*Swift*

- **Stage 1**: The stage of calibration of data where the calibration process depends on the operating modes since the information is telemetered differently in different operating systems. This process consists of:

  1. Calculation of the PHA (Pulse Height Amplitude) as the sum of all the PHA values from the center pixels and the surrounding ones of every mode, and assign a grade[7]

  2. Conversion of PHA value in the PI (Pulse Invariant) value

  3. Transformation of the raw coordinate from the detector to the sky coordinate by considering the attitude of the satellite

  4. Flagging of the bad pixels or columns

  5. Flagging of the hot and flickering pixels[8]

  6. Calculation of the start and end time of the frame that depends on the source position

  7. Subtraction of bias

  8. Creation of a filter file that contains a list of parameters which are related to housekeeping (HK) files and attitude files

  The output of this stage is the Level 1 calibrated event files.

- **Stage 2**: The stage of screening the data, which is done in different steps. The first step is the creation of a filter file related with instrument housekeeping (HK) and attitude files. The next two main steps are: the calculation of the Good Time Intervals (GTIs) and the filtering of data by using the GTIs and event files. The output of this stage is the Level 2 calibrated event files.

- **Stage 3**: The stage where all the scientific products are generated, such as images, light curves and spectra through a task called `xrtproducts` and after that through different tasks as: `ximage`, `xselect`, `xronos`, `xrtmkarf`, `xspec`. Along this stage the scientific products (Level 3 files) are created. During this stage for the creation of the spectrum, an exposure map file should be utilized. The exposure map file is necessary, in order to correct the loss of the flux due to the bad columns.

The calibration, screening and filtering process are realized by using the latest calibration files available in the *Swift* calibration database (CALDB[9]) by the time of the processing of the data.

All the above stages are well realized by simply running a command called `xrtpipeline` (Capalbi et al., 2005). `xrtpipeline` is a perl script consisting of 16 different tasks, which include all the items indicated in all of the above stages.

In this way, by running the `xrtpipeline`, the reduction of the needed data is complete. Firstly, one needs the data, that are available to download from NASA/GSFC *Swift* Data Center and the process continues by running the script in the most common/simplest way:

---

[7]grade is the shape description of charge spread in a CCD for certain events. The shape for a PC mode is a 3x3 matrix classified in 32 grades (the range 0-12 has better resolution), whereas the shape for WT mode is a 7x1 matrix classified in 15 grades (the range 0-2 has better resolution)

[8]hot pixels are considered pixels of a lower Poisson probability of the counts compared to the Poisson probability of the mean counts in the CCD

[9]http://heasarc.gsfc.nasa.gov/docs/heasarc/caldb/

```
xrtpipeline indir=./00622006000[10] steminputs=sw00622006000
outdir=./00622006000-xrt createexpomap=yes useexpomap=yes
       correctlc=yes >& ./00622006000-xrt/pipeline.log
```

How to understand the files format?

The output of `xrtpipeline` gave the XRT science files (events and images) in these formats:

```
Event:  sw[obs_id]x[mm][ww][pp]_[lev].[ext]
    Image:  sw[obs_id]x[mm]_[lev].[ext]
```

where:

- **sw** is a prefix which tells that these data are taken from *Swift* satellite.

- **[obs_id]x** is the observation id (identification of observation) that contains 11 digit numbers and is created from the Observation Segment and the Target ID. These two numbers are identified during the observation of the target, on-board of the *Swift*. The Observation Segment identifies the monitoring campaign and the Target ID identifies the target that is observed and is unique for every target that the instrument detects; whereas **x** identifies that data are observed from XRT instrument.

- **[mm]** displays the instrument operating systems expressed in two character strings. The operating systems are as explained above: pc-photon counting mode, wt-windowed timing mode, pu-piled up, lr- low rate and im-imaging mode.

- **[ww]** displays the window setting of the CCD for PC and WT, whereas for Photodiode modes identify where the bias has been subtracted, on-board or not. If the set is 'wN ', where the number is from 1-9 that corresponds to a specific CCD window setting for PC or WT. For WT there are 5 possibilities (w1-w5) and for PC are 4 (w1-w4). If the set is 'bN', it corresponds to the bias subtraction of the Photodiode mode. If the subtraction has been done on board the N is 1 and if not it is 0.

- **[pp]** displays how the instrument was during the observation: po-pointing mode, sl-slew and sd -settling.

- **[lev]** displays the file level (explained above). For event files the set is: uf-Level 1, ufre-Level 1a [11] and cl-Level 2. While for image files it is: rw-Level 1 and sk-Level 2.

- **[ext]** displays the file extension. Fore event files the set is .evt and for image files it is .img.

---

[10]the first XRT dataset of GRB 141221A, with an observation ID 00622006000 (see Chapter 3)

[11]Level 1a is an intermediate level for PC and WT, to accompany the proper arrival time with the events and to set the grade and PHA values while you reconstruct the events.

Temporal Analysis

The temporal analysis can be done independently using the free softwares: `FTOOLS`[2]`, CALDB`[9](available at the HEASARC repository). The process of data analysis should start by the reduction of data as explained in section 2.2.3, by simply running the command `xrtpipeline`. For further analysis we have to use the cleaned event file (PC or WT mode).

The first step is to do the extraction of the light curve. This is done by using the command `xselect`, which is a command line interface and all the steps below should be executed inside this command.

In order to choose the region of the source and the background, an image extraction is needed, and can be extracted by using the command `extract image` and followed by `plot image` command that leads to the opening of a SAOImage (an astronomical imaging and data visualization application).

The choice of the region is the first and one of the most important parts of data analysis. This is based on the PSF. The PSF is a 3-dimensional diffraction pattern of emitted light from an infinitely small point source and transmitted to the image plane into a corresponding point. This image plane can be represented as an intensity distribution, which has a high value that is called NA (Numerical Aperture) and a low value at the intensity zero. The FWHM (Full Width at the Half Maximum) is represented as the value of NA along the Rayleigh-limit which obviously contains 50% of the total Flux, as is illustrated in Fig. 2.7 A. If we see this diffraction pattern in the 2D plane, we would see some concentric rings, which correspond to a contour map of the source, like in Fig. 2.7 B. As we see this is a colored map where each color represents different values of intensity. Therefore the X-ray image which we observe is illustrated on the Fig. 2.7 C.

(A) Point Spread Function

(B) Contour map
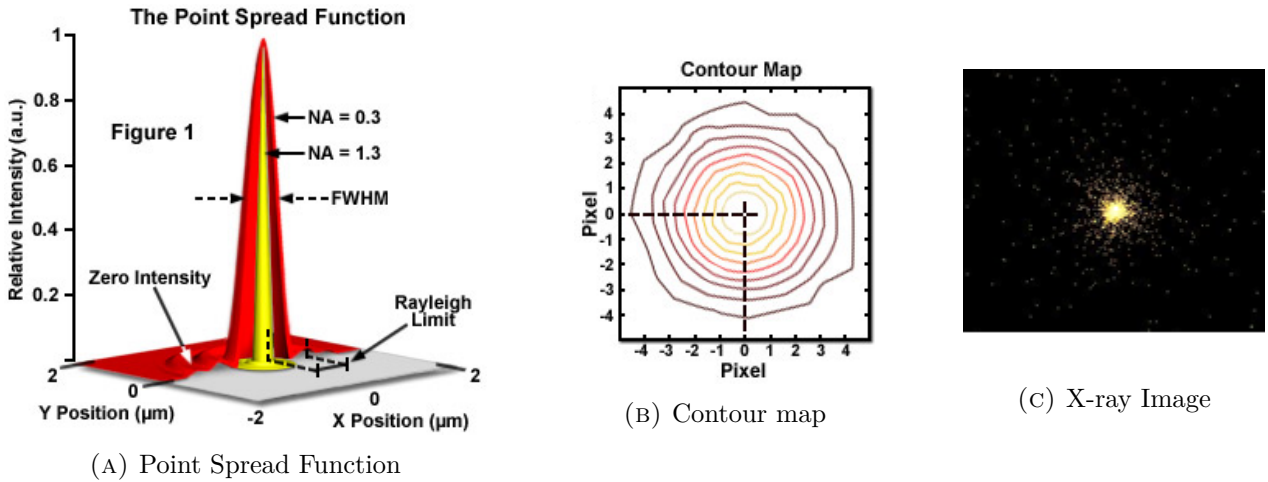
(C) X-ray Image

FIGURE 2.7: From the PSF to the X-ray image that we observe for different sources

The peak of PSF corresponds to the center of the source.
Thus, the region that should be chosen, it is necessary to cover the maximum of the Fluxes inside the source, that means to contain the complete PSF of a source. Furthermore, a large region would be dominated from the background counts, as a small region would make it lose

a lot of counts. Hence, the best region for the source detected by *Swift* satellite is explained below.

Generally, for bright sources where the pile-up is not present, the region is chosen as 25 pixels (maximum 30 pixels), whereas for faint sources 20 pixels (at least 15 pixels). While the background is chosen as 60 pixels (50 pixels) for bright (faint) sources, far away more than 20 pixels from the source. Even in the cases where we detect a faint burst, the decrease of the region should not go smaller than 15, because of its PSF.

For the pile-up sources, the region source is chosen as explained in section 2.2.2, while in the background the procedure is given above. Once the region is chosen, that should be the same and unchanged for further steps. After creating the region, it can be used by simply filtering it with the command `filter region` followed by the name of region/background. The command `clear region` can be used to remove the region. The XRT coordinates of GRB are found in the *Swift*-XRT GRB position web page[12]. This is the first important step of the data analysis, since an incorrect region of the source/background might lead to uncertain results.

The second step, the filtering of the energy band is necessary, and since I am explaining the data analysis for the XRT/*Swift* instrument, the filtering of energy should be between 0.3-10 keV, but that also depends on the purpose of the study. The filtering of the energy is done by using the command `filter pha_cutoff`, and putting them in the units of channel, not in keV (e.g. 300-1000 in channels). The command `clear pha_cutoff` can be used to remove the filtering energy.

Then, for some studies, we should also filter the time. This filter is compulsory, if you need a precise time for your study. To do so, you can use one of these commands: `filter time cursor`, which is a command that does not need a precise time, but you just choose the required approximate time by using the mouse cursor or `filter time scc`, where you can choose the precise time from the keyboard. In both cases, a file will be created which will give the good time intervals according to your necessity. Once this file is created it can be used for further filtering for the same observation, if the same time interval is required. To do so, the command `filter time file` should be used, followed by the name of `.gti` file as well. If you need full observation for your study, you simply ignore this stage.

This is an important step of the analysis, which one should be conscious of. If the early/late results are needed for the research, the proper analysis should be made for the time interval, where the study is required. This might have a serious effect on the study mostly for sources which are highly variable along the time.

After that, since all the important parameters are fixed, the last stage is to extract the light curve by using the command `extract curve` which leads to a second command of saving `save curve` followed by the name that you want, with an extension `.lc`. The same way can be followed for both modes, PC and WT. Since the cleaned event file is used for the extraction, the filter of grade is not needed. The filter of grade is used for unclean event files (e.g. an unfolded event), and it is different for PC and WT timing mode. `Filter grade` is the required command in this case, and it is 0-12 for PC mode and 0-2 for WT mode.

---

[12]www.swift.ac.uk/xrt_positions/

Occasionally, it is essential to bin the light curve, in order to have a better resolution of the last image. The binning of light curve is based on the following criteria:

- Instrumental limit which allows a minimum for the duration of the bin related to their readout mode. The duration of the bin should be longer than 2.51 sec for the PC mode and longer than 1.7 msec for WT mode.

- Statistical parameter which requires a minimum count rate for a source region. The minimum rate is 20 counts for PC mode and 30 counts for WT mode. This limit allows us to use the Gaussian statistics and avoid in this way the big errors.

- Significance of the detection of the burst which has to be more than 3σ in order to consider a background contamination in the source of less than 0.3%.

Usually the bin size used is given in seconds and can be changed simply by using the command `binsize` followed by the number which tells the bin size in seconds. A binned light curve has a better significance than an unbinned one, where the error bars are significantly high.

The extraction of the light curve should be in the same way for the source and background, by using all the stages above with the same properties.

The plot and fit of light curves can be done in `xspec` or in any other program which is able to create high level data visualization.
If the plot and the fit of the light curve is completed with `xspec` then first we should subtract the background from the source by using the command `lcmath`, which asks for a scaling factor, which corresponds to the surface ratio between source and background. As explained in Section 2.2.3, we should correct for the effect of the bad column by using the exposure map file. For the light curve with a bin size smaller than 10 sec (means that the correction is made for a single snapshot), the correction can be done by using the command `xrtlccorr`, whereas for the light curves with a bin size bigger than 10 sec, the exposure map is created from the beginning by running the `xrtpipeline`, or by creating it separately as:

```
xrtexpomap infile=sw00622006000xpcw3po_cl.evt
    artfile=sw00622006000sat.fits hdfile=sw00622006000xhd.hk
             outdir=sw00622006000xpc_expo.img
```

In order that we have a proper file to be used for the plot and fit in `xspec`, we first need to create an ASCII file from the extraction file of the light curve. The ASCII file should be in this format:

```
 TSTART   TSTOP   Count_Rate*(TSTOP-TSTART)   Error_Count_Rate*(TSTOP-TSTART).
```

The file should be written only in this way, because `xspec` is built for spectral fits, which plots spectra as count/sec/keV against keV. Hence, the light curve should be written in the units count/sec/sec in order to have a light curve in terms of count/sec against time in sec. The file should be different for each snapshot.

The generation of `pha` and `rsp` files are required in order to read the light curve in `xspec`. The `rsp` file is a Response Matrix File R(E,I)) which describes how a photon with energy E is redistributed in the output detector channels (PHA or PI) I. These files are generated from the command `flx2xsp`, which enables the creation of the light curves with fixed numbers of counts per bin by using the ASCII file.

The rebinning of light curve is completed by using the command `grppha`. The real value of this rebinning will be explained in the next section of the spectral analysis. After going through all these steps, our light curve is ready to be plotted and fit in `xspec` although the fitting model depends on the propose of the study and the canonical behaviour of light curves. This means that not every GRB shows all different parts of the canonical behaviour.

For the second case (you do not use the `xspec` for the fit), a `qdp` file is necessary, which gives you the data of the light curves for the source and background, which can be taken after the extraction of the light curve in `xselect` and includes the time, the count rates and the errors of count rates. The program should first make the subtraction of the background from the source continuing with the conversion of time from *Swift* seconds (since 2001 UTC in decimal) in the time after the trigger[13]. This conversion is done by subtracting the trigger time from the starting time of each observation (ΔT) and after then subtracting the extraction time of each point with ΔT, without forgetting the effect of binsize as a sum with *binsize*/2. We can continue the fitting process with the same idea as the fitting in `xspec`.

The light curve can be in terms of count rates or Fluxes. To convert from count rate to flux, a conversion factor called Energy Conversion Factor (ECF) is required. Thus the conversion of light curves in the Flux units is done by multiplying the light curves in the count rates units with the ECF. The way in which the ECF is found will be explained in the next section. This factor is really important and may consequently change the significance of the results. The dependence of this factor from the best fitting model, makes it an independent parameter from the instrument. Furthermore, the ECF cannot be the same for a burst with spectral evolution. Thus, the ECF is required to be found separately for every part where there is no spectral evolution.

Spectral analysis

The first step of the spectral analysis is the same as for the temporal one, the extraction of the spectrum. For spectral analysis, the region of the source and the background should be the same as for temporal analysis, thus the first step is the same as explained above (the extraction of the image). The filtering of the energy is not needed for the spectral analysis during this step, since it will happen later.

The time interval required for the spectral analysis is created in the same way as in the temporal analysis, by using the command `filter time cursor` or `filter time scc`.

The binning of the spectrum in this step is not essential. After doing all of these things, we keep going with the extraction of the spectrum by running the command `extract spectra` and

---

[13]correspond to trigger time (sec) + the time of the burst explosion (sec)

leading by a second command `save spectra` which saves the extraction, followed by the name of the spectrum with an extension `.pha` or `.pi`.

The second step is to generate an Ancillary Response File `ARF`. `ARF` file contains information of the effective area of the telescope as a function of energy, and it is needed for further spectral analysis. Along this step, it is also necessary to perform an exposure time, in order to make the correction for the bad columns. The command used is `xrtmkarf expofile=...`.

The third step is the binning of the spectrum by running the command `grppha`. During the binning of the spectrum it is also necessary to have a redistribution matrix file `RMF` file that is located in the calibration directory. For the version of `RMF` it is better to use the proper version that was given by running the `xrtmkarf`. An important thing during the binning is to exclude the bands of energy outside the XRT instrument, meaning it is better to put the energy range 0.3 - 10 keV. In this way, the filtering of the energy is completed for the spectrum. It is best that during this step we exclude only the energy range that is not used from the XRT instrument. The energy range between 0.2 - 0.3 keV usually is not taken into account in order to not have contamination from the Earth limb radiation. If the filtering of the energy is needed in another range, then it can be acquired from `xspec`.

The binning depends on the statistics that are utilized. Usually two statistics are used: χ^2 statistic (Lampton et al., 1976) and C-statistic (Cash, 1979). The χ^2 statistic is a fit statistic which quantifies how well the data match the model by measuring the difference between the data and the model. The χ^2 statistic considers that the data are Gaussian, hence the improved binning is more than 20 counts per bin (Humphrey et al., 2009), whereas the less counts per bin brings the Poisson distribution of the data. For observation with few counts it is better to use C-statistic, since the use of χ^2 will make the data very smooth and some information may be lost. The C-statistic creates an unbinned spectrum based on a maximum likelihood method for Poisson distributed data.

After all these steps, the spectrum file will be compatible for fitting in `xspec`. The X-ray fit is suitable to fit with a single power law absorbed twice, the first one fixed in the absorption value of our galaxy in the direction of the burst and second is letting free to vary in the distance of the burst.

The χ^2 statistic tells, how likely is the data to assume that the model is true. To predict for a good fit according to the model that is used, it is necessary to check two parameters:

- **Reduced-χ^2 (χ^2_ν)**: The smaller the value, the better the fit, since in this way the difference between the model and the fit is smaller. The value of χ^2 for a good fit (this also depends on the degrees of freedom) should be around 0.8–1.2. This means that the observed and the expected distributions are similar: $\left(\dfrac{\chi^2}{dof} \approx 1 \right)$

- **Residuals**: The residuals are expressed in the terms of sigma, where the sigma is calculated as the square root of the counts in the predicted model. The size of error bar is 1. The residuals should be centered on zero and should have a constant throughout the range of the fit value. Thus, the residuals should be neither systematically high nor low.

- **Null-hypothesis probability**: The comparison between the χ^2 that is measured from the fit with the theoretical χ^2 distribution for the same degrees of freedom. The probability of getting χ^2 larger or as large as the one observed, if the model is correct. If this probability is very small then the model is not a good fit.

If there is a problem with any of these items, the model should be rejected and another one should be used (Arnaud et al., 2015).

After finding the best fit of the spectrum, we can find different parameters. If you want to build a light curve in the terms of flux, you will need the ECF parameter. ECF is found as the ratio of the Flux of the model of the burst and Count Rates. This coefficient is different for different energy ranges that you use, as the Flux is different for different energy range.

2.2.4   Background subtraction

In the X-ray, the data are collected as individual events. While doing the analysis we should consider both the source and the background. Usually the X-ray background is a combination of the cosmic X-ray background, the noise and different sources like solar flares, cosmic rays, etc. There are different ways to choose a background:

- **background taken in a blank sky**: in this way, we choose the background of almost 20 pixels further than the burst and in a blank area, not contaminated from other sources that might be in the same FoV

- **local background**: to choose the source and background in the same position, the region of background should be much bigger than the one of the source.

In both cases, in order to have better analysis, we should subtract the background from the source. The standard theory to do this is:

$$CR_{net} = CR_S - \frac{R_S \, t_S}{R_B \, t_B} CR_B,$$ (2.3)

where CR_{net} is the net count rate of the source, CR_R the observed count rate of the source, CR_B the observed count rate of the background, R_S, R_B the regions of source and background respectively and t_S, t_B the exposure times of source and background.

2.2.5   Existing pipelines

As *Swift* is observing a large number of GRBs, it is worth having all the scientific results for every burst and to work with them. In fact this job is taken into account and is regularly done by the UK *Swift* Science Data Center. All the results of this work are published and are free to access through the web page: `http://www.swift.ac.uk`. The procedure followed for doing the temporal and spectral data analysis is explained in Evans et al., 2009, 2007. The XRT online repository provides all of the scientific results required for a further work for every GRB, only

in the X-ray part.

Another pipeline is completed individually by Margutti, 2008–2009 for the X-ray afterglows of GRB. The results are not easy to access, but the method used is clearly explained in Margutti, 2008–2009.

The differences between the XRT official team and the individual work of R. Margutti are in these points:

- The regions for event extraction in able to maximize signal-to-ratio

- The weight of the ARFs

- The fitting statistic

- The protection from the local minimum

- The method of finding the conversion factor, in order to be able to translate the count rate light curves into the flux light curves.

Chapter 3

GRB 141221A

The previous chapters have set the theoretical and historical view of the GRB phenomenon, and how to reduce the data that led to these results. As stated before, the purpose of this thesis is to study GRBs through correlations, implying the reduction of a very large sample of data. This part will be explained in the Chapter 4. I would however show in this Chapter how the complete use of the methods and theories listed before can give insights on any peculiar GRB. For this purpose, I selected GRB 141221A, which is analyzed in detail in this Chapter and has been published in MNRAS (see Appendix A).

GRB 141221A is a burst detected by *Swift* at 08:07:10 UT, which is called T_0, on December 21, 2014 (Sonbas et al., 2014). The duration of the burst was ($T_{90} = 36.9 \pm 4.0\,$s Ukwatta et al., 2014, making it a typical lGRBs), allowed ground telescope to start the observation while the prompt was still active. It is a gamma-ray burst observed from infrared to soft gamma-ray bands.

In the analysis for this GRB, all errors are quoted at the 90% confidence level (except when otherwise stated), and the Universe model used is a flat ΛCDM model with $H_0 = 70$ km s^{-1} Mpc^{-1}, $\Omega_m = 0.3$ and $\Omega_\Lambda = 0.73$.

3.1 Observations

3.1.1 High Energy data

***Swift*-BAT and Fermi GBM**: GRB 141221A triggered both instruments (Ukwatta et al., 2014, Yu, 2014), at nearly the same time (08:07:10 UT for Swift, 08:07:11.22 UT for Fermi). The recorded duration is, however, longer in the BAT compared to GBM (23.8 s), as one can expect from the larger effective area (and hence better sensitivity) of BAT/*Swift*.

***Swift*-XRT**: the XRT observed the burst position between $T_0 + 64\,$s and $T_0 + 34.9\,$ks (Beardmore et al., 2014, Maselli et al., 2014), mostly in PC mode. The afterglow was clearly detected in X-rays.

3.1.2 Optical and infrared data

Various ground instruments detected GRB 141221A. I give a brief prescription of all these instruments, while all available measurements and the corresponding filters are listed in Table 3.1.

***Swift*-UVOT**: the observations started at $T_0 + 84\,\text{s}$ (Marshall and Sonbas, 2014). The afterglow is clearly detected.

TAROT La Silla: the observations at TAROT-La Silla (Boër et al., 2003) started at $T_0 + 31.2\,\text{s}$ and lasted for about 41 minutes, until the beginning of sunrise (Klotz et al., 2014). The burst is not detected between $31\,\text{s}$ and $68\,\text{s}$, with a limiting magnitude $R_{lim} = 16.6$. After that time, the burst is clearly detected for the remainder of the observation.

Skynet PROMPT-CTIO: the observations with Skynet PROMPT-CTIO (two 14 inch telescopes), at Cerro Tololo, Chile (Reichart et al., 2005), started at $T_0 + 45\,\text{s}$ and lasted for 27.25 min (Trotter et al., 2014a,b). 44 exposures were taken in the V and I bands ranging from 5 to $160\,\text{s}$. The optical afterglow was clearly detected with a rising light curve at t = 2 min and peaks at I = 14.8. Skynet observed the afterglow again at $T_0 + 23.0\,\text{h}$ for 1.5 h, taking 64 exposures of 160 s each in V and I bands.

REM: The Rapid Eye Mount (REM Chincarini et al., 2003) observations started at $T_0 + 60\,\text{s}$ and lasted for one hour until the beginning of the twilight (Covino, 2014). The afterglow was detected in all filters (grizJHK).

GROND: GROND (Greiner et al., 2008) observations started at $T_0 + 142\,s$ (Schweyer et al., 2014), and continued for 18 minutes. The afterglow was clearly detected.

LCOGT-McDonald: LCOGT-McDonald (Brown et al., 2007) detected the afterglow as well. The observations started at $T_0 + 2.3\,\text{h}$ (Guidorzi et al., 2014), and were done with SDSS r' and i' filters.

KECK II telescope: spectroscopic observations with the Keck II telescope were performed from $T_0 + 1.78\,\text{h}$ to $T_0 + 2.15\,\text{h}$. Several lines were detected (Mg II doublet and Fe II) putting this burst at a redshift of z = 1.452 (Perley et al., 2014).

MITSuME Akeno: Finally, MITSuME (Yatsu et al., 2007) observed the afterglow at $T_0 + 9.1\,\text{h}$ (Ono et al., 2014). The observations were made in three filters g', Rc and Ic.

3.2 Data reduction

3.2.1 Interstellar Extinction

Around 1784, a few astronomers observed an absence of stars in different parts of the sky, but without understanding why. Almost two and a half century later, astronomers were able to explain this effect as dust clouds that absorb, causing people to believe that there were black sections in the sky. This is what is called interstellar extinction. The two different effects that

TABLE 3.1: Optical data converted in AB System and corrected from Galactic extinction. Credit: Bardho et al., 2016

Mid time (sec)	Filter	Magnitude AB System	Telescope	Reference[a]	Mid time (sec)	Filter	Magnitude AB System	Telescope	Reference[a]
65.46	R	< 16.76	TAROT	(1)	57.00	V	< 16.72	Skynet	(1)
71.46	R	16.18 ± 0.2	TAROT	(1)	69.00	V	$17.00^{+0.95}_{-0.54}$	Skynet	(1)
77.46	R	15.84 ± 0.2	TAROT	(1)	84.00	V	$16.66^{+0.24}_{-0.19}$	Skynet	(1)
83.46	R	15.66 ± 0.2	TAROT	(1)	101.00	V	$15.93^{+0.12\,b}_{-0.10}$	Skynet	(1)
89.46	R	15.76 ± 0.30	TAROT	(1)	123.00	V	$16.21^{+0.08}_{-0.08}$	Skynet	(1)
119.60	R	15.63 ± 0.03	TAROT	(1)	150.00	V	$16.25^{+0.08}_{-0.08}$	Skynet	(1)
160.10	R	15.52 ± 0.03	TAROT	(1)	177.00	V	$16.23^{+0.08}_{-0.07}$	Skynet	(1)
200.70	R	15.56 ± 0.03	TAROT	(1)	205.00	V	$16.19^{+0.08}_{-0.07}$	Skynet	(1)
241.00	R	15.58 ± 0.03	TAROT	(1)	242.00	V	$16.28^{+0.05}_{-0.05}$	Skynet	(1)
281.30	R	15.55 ± 0.03	TAROT	(1)	290.00	V	$16.49^{+0.07}_{-0.06}$	Skynet	(1)
351.70	R	15.76 ± 0.09	TAROT	(1)	337.00	V	$16.44^{+0.06}_{-0.05}$	Skynet	(1)
446.30	R	16.33 ± 0.02	TAROT	(1)	384.00	V	$16.61^{+0.07}_{-0.06}$	Skynet	(1)
611.00	r'	16.54 ± 0.1	GROND	(2)	451.00	V	$16.77^{+0.04}_{-0.04}$	Skynet	(1)
760.60	R	16.79 ± 0.02	TAROT	(1)	539.00	V	$16.96^{+0.05}_{-0.05}$	Skynet	(1)
861.20	R	16.84 ± 0.08	TAROT	(1)	627.00	V	$16.96^{+0.05}_{-0.05}$	Skynet	(1)
1074.40	R	17.11 ± 0.08	TAROT	(1)	636.00	V	$17.35^{+0.26}_{-0.26}$	UVOT	(3)
1327.50	R	17.38 ± 0.08	TAROT	(1)	716.00	V	$17.19^{+0.06}_{-0.06}$	Skynet	(1)
2011.00	R	17.98 ± 0.08	TAROT	(1)	804.00	V	$17.40^{+0.07}_{-0.07}$	Skynet	(1)
48.00	I	$17.05^{+0.65}_{-0.42}$	Skynet	(1)	931.00	V	$17.49^{+0.06}_{-0.05}$	Skynet	(1)
68.00	I	$15.97^{+0.12}_{-0.11}$	Skynet	(1)	1098.00	V	$17.77^{+0.07}_{-0.07}$	Skynet	(1)
85.00	I	$15.46^{+0.07}_{-0.06}$	Skynet	(1)	1266.00	V	$17.98^{+0.10}_{-0.09}$	Skynet	(1)
102.00	I	$15.25^{+0.06}_{-0.06}$	Skynet	(1)	1433.00	V	$18.19^{+0.13}_{-0.12}$	Skynet	(1)
123.00	I	$15.19^{+0.04}_{-0.03}$	Skynet	(1)	1600.00	V	$18.43^{+0.17}_{-0.15}$	Skynet	(1)
150.00	I	$15.23^{+0.03}_{-0.03}$	Skynet	(1)	85523.00	V	$22.23^{+3.83}_{-1.10}$	Skynet	(1)
177.00	I	$15.26^{+0.03}_{-0.03}$	Skynet	(1)	611.00	g'	17.01 ± 0.1	GROND	(2)
205.00	I	$15.45^{+0.04}_{-0.04}$	Skynet	(1)	611.00	z'	16.07 ± 0.1	GROND	(2)
242.00	I	$15.52^{+0.03}_{-0.03}$	Skynet	(1)	611.00	J	15.68 ± 0.1	GROND	(2)
290.00	I	$15.60^{+0.03}_{-0.03}$	Skynet	(1)	611.00	H	15.39 ± 0.1	GROND	(2)
337.00	I	$15.62^{+0.03}_{-0.03}$	Skynet	(1)	611.00	K	15.29 ± 0.1	GROND	(2)
384.00	I	$15.77^{+0.04}_{-0.04}$	Skynet	(1)	561.50	b	17.73 ± 0.21	UVOT	(3)
451.00	I	$15.85^{+0.02}_{-0.02}$	Skynet	(1)	421.00	u	18.47 ± 0.07	UVOT	(3)
539.00	I	$16.11^{+0.03}_{-0.03}$	Skynet	(1)					
611.00	i'	16.35 ± 0.1	GROND	(2)					
627.00	I	$16.26^{+0.04}_{-0.03}$	Skynet	(1)					
716.00	I	$16.45^{+0.04}_{-0.04}$	Skynet	(1)					
804.00	I	$16.54^{+0.04}_{-0.04}$	Skynet	(1)					
931.00	I	$16.71^{+0.03}_{-0.03}$	Skynet	(1)					
1098.00	I	$16.99^{+0.04}_{-0.04}$	Skynet	(1)					
1265.00	I	$17.27^{+0.06}_{-0.06}$	Skynet	(1)					
1433.00	I	$17.36^{+0.07}_{-0.06}$	Skynet	(1)					
1600.00	I	$17.75^{+0.10}_{-0.09}$	Skynet	(1)					
85609.00	I	$21.45^{+0.67}_{-0.43}$	Skynet	(1)					

[a]References for the data: (1) this work, (2) Schweyer et al. (2014), (3) Marshall and Sonbas (2014)

[b]This point presents an instrumental bias and has not been taken into account during the analysis

this extinction cause are absorption and scattering of the light. The extinction appears to be different for different wavelengths. The shorter the wavelength, the higher the extinction (see Fig. 3.1).

The Dark Cloud B68 at Different Wavelengths (NTT + SOFI)

ESO PR Photo 29b/99 (2 July 1999)

© European Southern Observatory
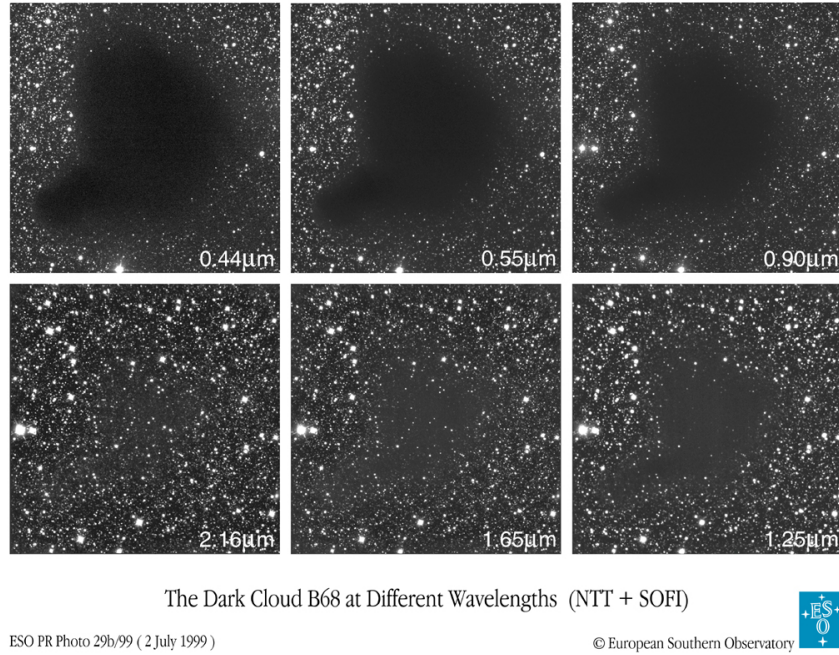
FIGURE 3.1: The observation of the dark cloud B68 with different filters and the effect of the extinction in each of these filters. Credit: ESO

The blue light is affected more by the extinction than the red light. As a result, the stars that are binding large amounts of dust look redder than they are in reality. This effect is called the interstellar reddening and is characterized by the R_V quantity that is given by:

$$
\begin{aligned}
E(B - V) &= (B - V)_{obs} - (B - V)_{int} \\
&= A_B - A_V \qquad \Rightarrow \qquad A_V = R_V * E(B - V),
\end{aligned} \tag{3.1}
$$

where $(B - V)_{obs}$ and $(B - V)_{int}$ are the observed and intrinsic color access respectively, the A_B and A_V are the extinction in the respective bands, B and V and R_V is the ratio of total to selective extinction with a value ≈ 3.1.

Taking the V band as the zero point for every observation, we have to correct for the interstellar extinction by finding the A_λ (for each wavelength) that depends on the direction of the source following the method of Schlafly and Finkbeiner, 2011.

3.2.2 Optical/IR data

The TAROT data were reduced using the standard procedure already discussed in Klotz et al., 2008. We convert the observed signal from the clear filter to the R filter by calibrating the magnitude of the afterglow against nearby stars of similar colour.

Subsets of the Skynet images were stacked to maximize the signal-to-noise ratio (SNR). Calibration of these images was performed using three stars in the field from the AAVSO APASS DR7 catalogue. The *BVg'r'i'* magnitudes from APASS were converted to *BVRI* Vega magnitudes using transformations provided by AAVSO (A. Hendon, private communication). Standard bias, dark, and flat corrections were applied to all images. Consecutive images were grouped and stacked in a way which maximizes the SNR of the afterglow while minimizing the loss of temporal resolution. The afterglow and a single primary calibration star were photometered in each stacked image and the resulting calibration offset was recorded. A master calibration stack was then generated for each filter by combining all available images. For each master calibration stack, the primary calibration star was photometered as well as the two secondary calibration stars. By comparing the offset obtained from the secondary calibration stars to that obtained from the primary calibration star, a calibration correction is calculated and applied to all afterglow photometry.

The remaining data have been gathered from the literature and are compiled in Table 3.1. Fig. 3.2 displays the resulting light curves.
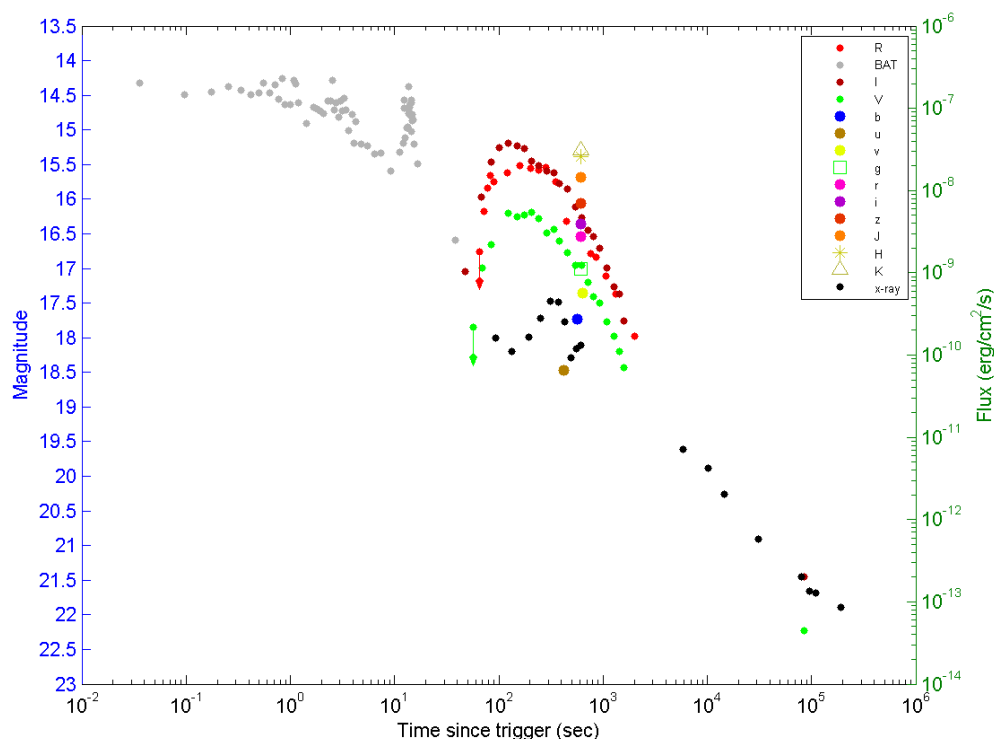
FIGURE 3.2: Light curve of GRB 141221A. The left axis refers to optical and infrared data, while the right axis relates with X-ray data only.

To further study GRB 141221A we have reduced all the measurements in the same system. The AB system is preferred because the conversion of AB magnitudes to flux densities is straightforward. The most important one, it is that the zero-point of the AB system is the same for all the wavelengths, while for the Vega system is different for different wavelengths. In order to do this conversion, we used different manuals that have the proper coefficients of conversions

for different filters depending on their instruments (Fukugita et al., 1995). The conversions are done only for TAROT, Skynet and UVOT data, that are using the Vega system. All the coefficients used in this case are shown in Fig. 3.2.

TABLE 3.2: Coefficients for conversion from Vega to AB system.

Filter	Instrument	Coefficient AB to Vega
R	TAROT (Bessel)	0.229
I	Skynet (Bessel)	0.452
V	Skynet (Bessel)	0.034
v	UVOT	0.025
b	UVOT	-0.095
u	UVOT	0.969

Whereas the formula for conversion is:

$$\text{mag(AB)} = \text{mag(Vega)} + \text{coeff(AB to Vega)} \tag{3.2}$$

The second correction is made for the Galactic extinction (Interstellar extinction that is explained in the above subsection), by using the value E(B-V) = 0.024 (Schlafly and Finkbeiner, 2011). This leads to the corrections listed in Table 3.3.

TABLE 3.3: Corrections to the magnitudes due to the Galactic extinction.

Filter	A_λ
u	0.117
b	0.092
V	0.075
v'	0.104
g'	0.091
R	0.074
r'	0.063
I	0.041
i'	0.047
z'	0.035
J	0.019
H	0.012
K	0.080

After that, we need to convert instrumental measurements to flux density:

$$m = -2.5 * log(F_\nu) + 23.926, \tag{3.3}$$

where, the flux density F_ν is expressed in units of μJy and the 23.926 is the zero-point of the AB system.

The final magnitude and flux density light curves are presented in Figures Fig. 3.2 and 3.3 respectively.
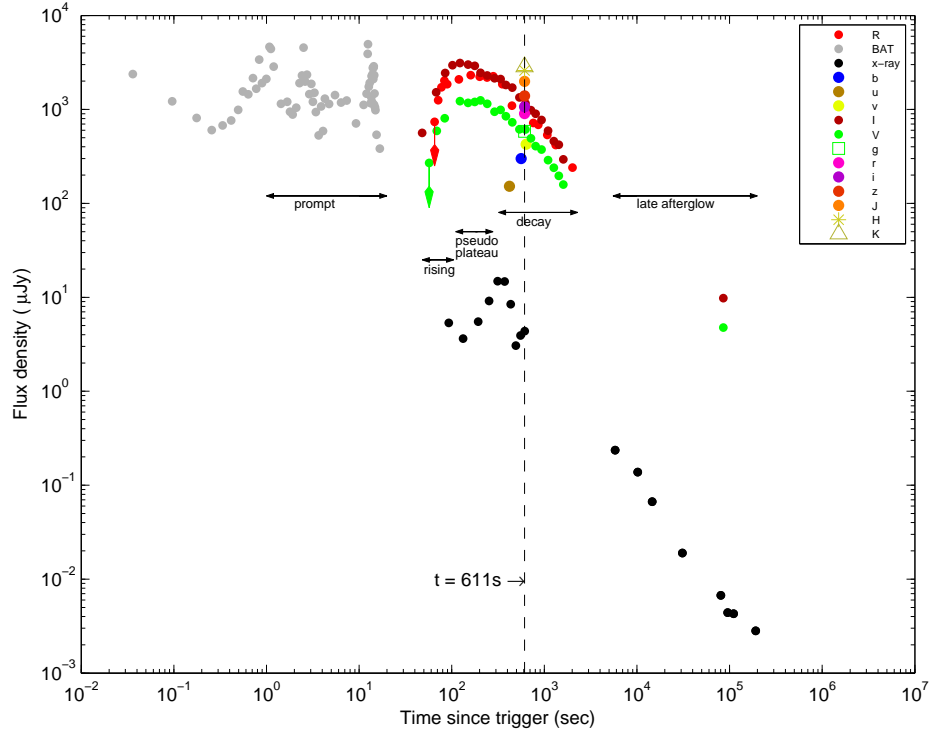
FIGURE 3.3: Flux density light curve of GRB 141221A. The vertical dashed line represents the epoch where the SED was extracted (see text for details). Credit: Bardho et al., 2016

3.2.3 Fermi data

GBM data for GRB 141221A were downloaded from NASA/Goddard Space Flight Center (GSFC) Fermi GBM Archive. The extraction of GBM data was done by using only the NaI detectors with the brightest signal in the 8 keV - 1 MeV band. In the case of GRB 141221A, these detectors were NaI 01 and NaI 02. We are using the task `RMFIT(v432)` for data reduction, using the time tagged event files (TTE) of each detector.

As the high-energy light curve of this event of two pulses, we performed all analysis both on each pulse separately and on the full time interval to check for spectral variations. For that purpose, we used the 8.0-900.0 keV energy band.

3.2.4 X-Ray data

The data for GRB 141221A were downloaded from the NASA/Goddard Space Flight Center (GSFC) *Swift* Data Center and were processed using `HEASoft(v6.16)` and XRTDAS software version 0.13.1, with the latest calibrations files available in June 2015. I used the task `xrtpipeline` to create the clean event file and to apply the latest calibration. The monitoring campaign for this GRB consists of 4 observations.

After that I performed a screening for bad pixels and piled-up data using the methods and corrections indicated in Romano et al., 2006 and Vaughan et al., 2006. We found that the flare observed in PC mode is piled-up during the interval $T_0 + 138.2$ s $– T_0 + 619.7$ s. In this case I

corrected this part by using the method explained in Vaughan et al., 2006, by using an annulus as the region of the source with an inner radius 9 pixels and an outer radius 25 pixels. Whereas the region of the source for late afterglow, where the pile-up was missing, was taken 22 pixels and the region of background was chosen more than 20 pixels farther than the region of the source, and with a radius 60 pixels, see Fig. 3.4. Lastly, I restricted the analysis to events with energy between 0.3 and 10.0 keV. This led to a net exposure of 50.53 s in the WT and 26 251.72 s in the PC.
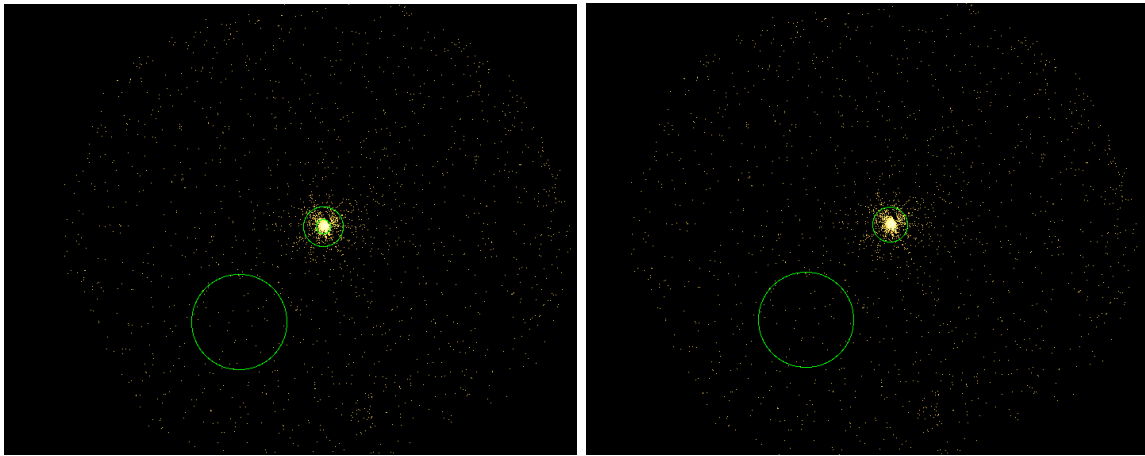
FIGURE 3.4: The regions of the source and background for GRB 141221A. In the left is the region for the flare and in the right the region for the late afterglow.

3.3 Data analysis

3.3.1 Prompt data

As already indicated, the prompt light curve has a duration (T_{90}) of about 23.8 s in Fermi-GBM and about 37 s in *Swift*-BAT, and consists of two pulses (see Fig. 3.5). For the spectral analysis of prompt emission I used the Fermi/GBM instead of *Swift*/BAT data, because of the much larger energy band of the former instrument (8-1000 keV for NaI detectors, while for BAT is 15-150 keV).

I used `xspec` version 12 (Arnaud, 1996) to fit the spectrum with a Band model (Band et al., 1993). I first fit each pulse separately (named Intervals 1 and 2 respectively), and then fit the complete spectrum. I also took an average of the two pulse results. All the results are displayed in Table 3.4, together with a reminder of the GCN result (Yu, 2014). The low signal prevented us from fitting all the Band parameters separately, and in all cases we had to fix the β parameter to a value of -2.3.

One fit is shown in the Fig. 3.6.

Knowing E_{peak} and the distance of this burst, I have calculated $E_{p,i} = 374 \pm 70$ keV and $E_{iso} = 2.4 \times 10^{52}$ erg. We note that these values follow the $E_{p,i} - E_{iso}$ relation (Amati, 2006, Amati et al., 2002), as can be seen in Fig. 3.7.
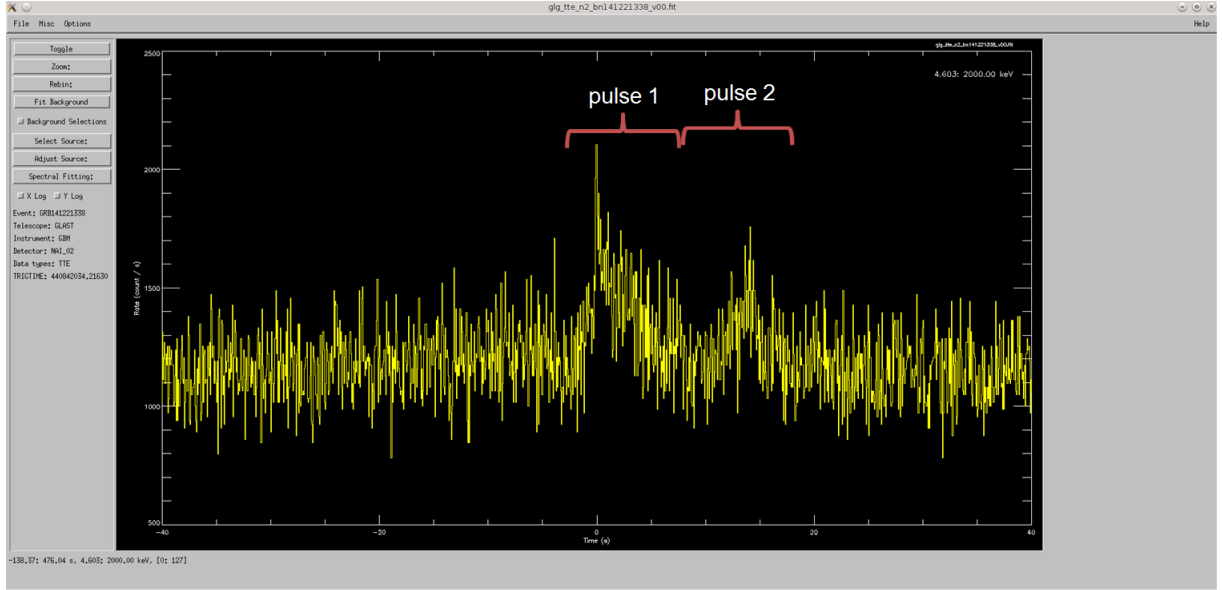
FIGURE 3.5: The two pulses shown from the observation of Fermi satellite for GRB 141221A.

TABLE 3.4: Results of the prompt spectral fitting. Non constrained parameters are fixed to the value indicated between square brackets. Credit: Bardho et al., 2016

Interval	time (sec)	exposure time (sec)	α	β	C-Stat	d.o.f	$E_{p,i}$ (keV)	E_{iso} (10^{52} ergs)
1	$-1.024 - 8.704$	9.728	[-1.00]	[-2.30]	431.57	241	353 ± 42	1.88 ± 0.11
2	$8.704 - 17.408$	8.704	-0.82 ± 0.38	[-2.30]	523.84	253	247 ± 77	0.83 ± 0.09
2	$8.704 - 17.408$	8.704	[-1.00]	[-2.30]	523.98	254	297 ± 61	0.88 ± 0.10
Total	$-1.024 - 17.408$	18.432	-1.24 ± 0.11	[-2.30]	558.20	240	531 ± 164	3.13 ± 0.25
Total	$-1.024 - 17.408$	18.432	[-1.00]	[-2.30]	558.97	241	328 ± 35	2.71 ± 0.14
averaged	$-1.024 - 17.408$	18.432	[-1.00]	[-2.30]	477.77	247.5	325 ± 52	2.74 ± 0.21
GCN	$-1.024 - 17.408$	18.432	-1.07 ± 0.13	—	—	—	374 ± 70	2.43 ± 0.29

3.3.2 Afterglow spectrum

XRT spectrum

I started by analysing the XRT spectrum alone, independently of the optical data. This is because at high energy (above $2\,\mathrm{keV}$), the spectrum is not influenced by the surrounding medium and the column density, and thus the X-ray spectrum allows to derive the intrinsic power-law index. I extracted three spectra, one in WT mode and two in PC mode (during the flare, and after the flare), and fit these with a power-law model absorbed twice (one let free to vary at the distance of the burst, the second fixed to the galactic value in the direction of the burst, $N_H^{gal} = 2.27 \times 10^{20} cm^{-2}$). The data are consistent with no spectral variation, though we can note that the error bars are large due to the low flux of the afterglow. The results of these fits are presented in Table 3.5.

The spectra for flare, late afterglow and full PC observation are presented in Fig. 3.8, 3.9 and 3.10.
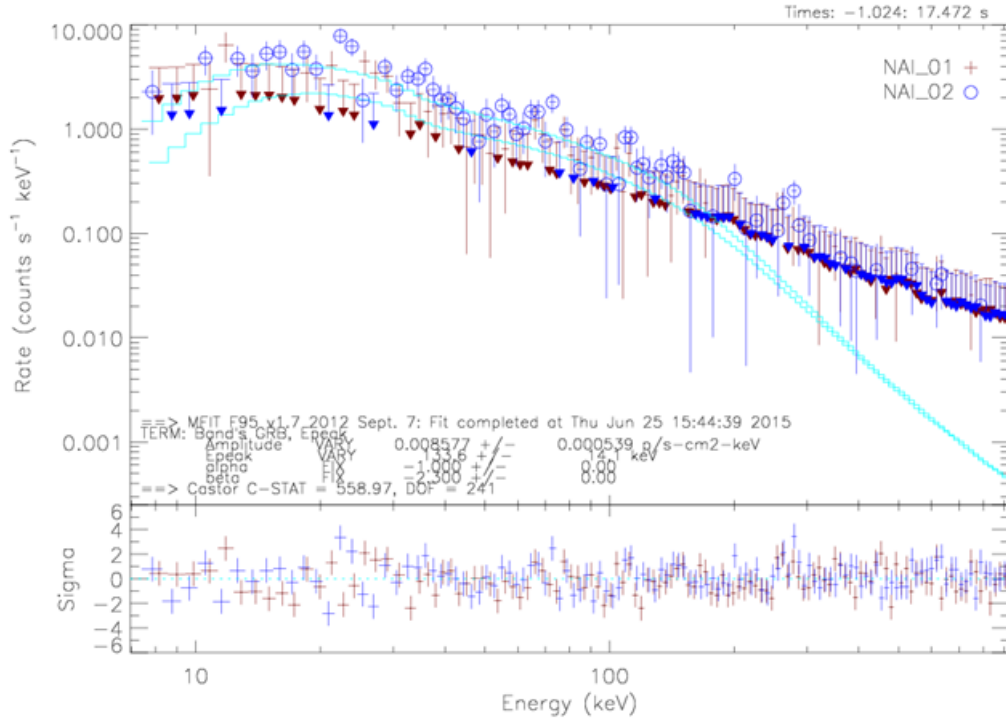
FIGURE 3.6: The spectrum of the prompt emission, included two pulses (indicated as total in Tab. 3.4).
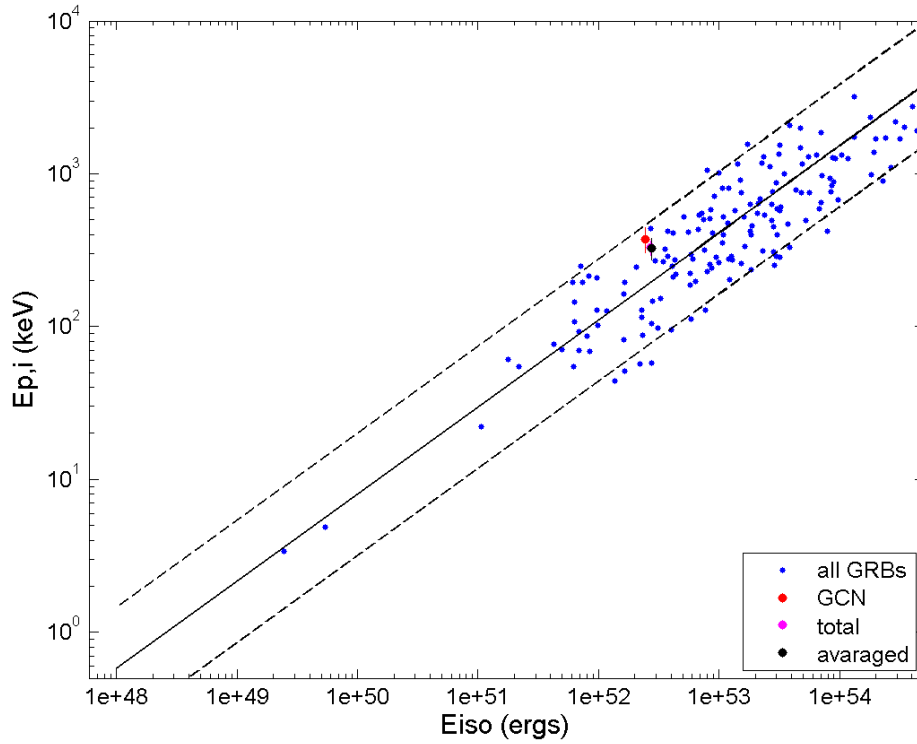
FIGURE 3.7: GRB 141221A compared to the whole sample of GRBs until June 2013. The solid line is $E_{p,i} = 110 * E_{iso}^{0.57}$, while the dashed lines are the 2 sigma standard deviation (Amati, 2006).
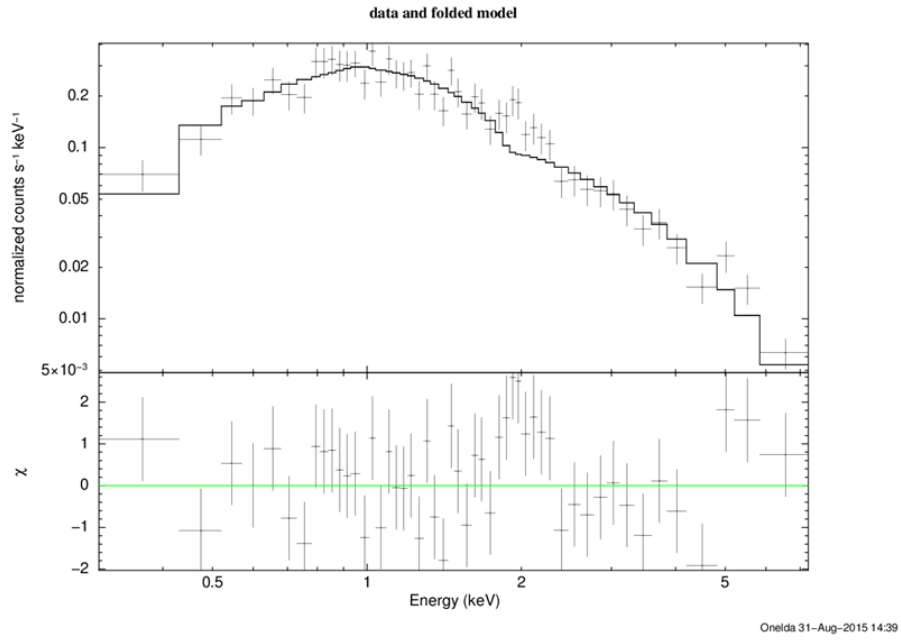
FIGURE 3.8: The X-ray spectrum of the first observation, only during the PC mode.
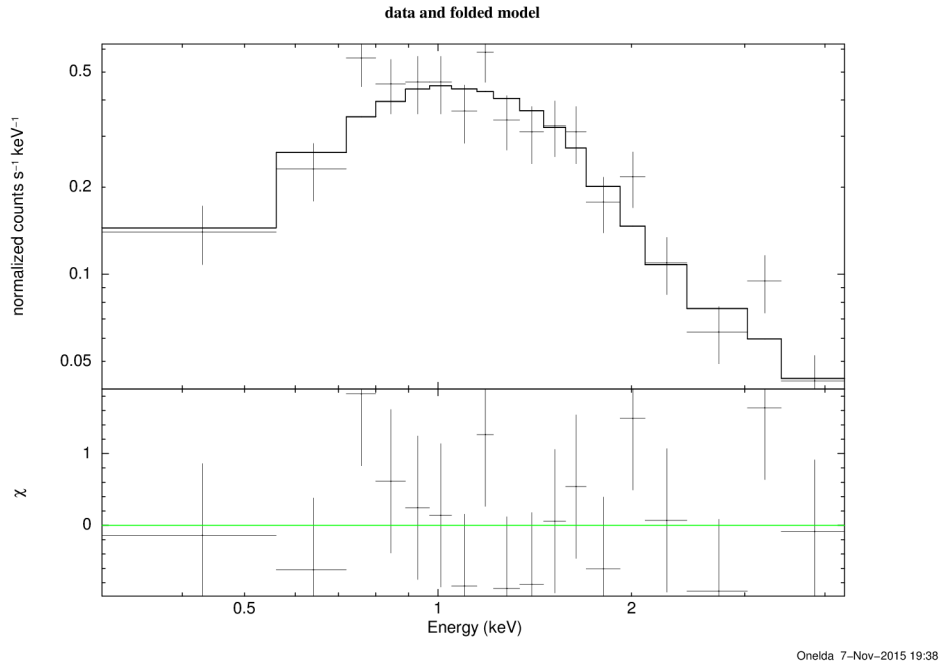
FIGURE 3.9: The X-ray spectrum of the flare during the PC mode.

TABLE 3.5: X-ray spectral analysis, independent of the optical measurements. See text for details. Credit: Bardho et al., 2016

Interval (sec)	mode	N_H^{int} (10^{22} cm^{-2})	β_x	χ_ν^2	d.o.f.
60 - 90	WT	$0.27^{+2.3}_{-0.27}$	$0.7^{+0.7}_{-0.5}$	1.02	6
100 - 1000	PC	$0.9^{+0.5}_{-0.4}$	$1.0^{+0.4}_{-0.4}$	0.96	15
3000 - 11000	PC	$0.5^{+0.6}_{-0.4}$	$1.0^{+0.4}_{-0.4}$	0.89	7
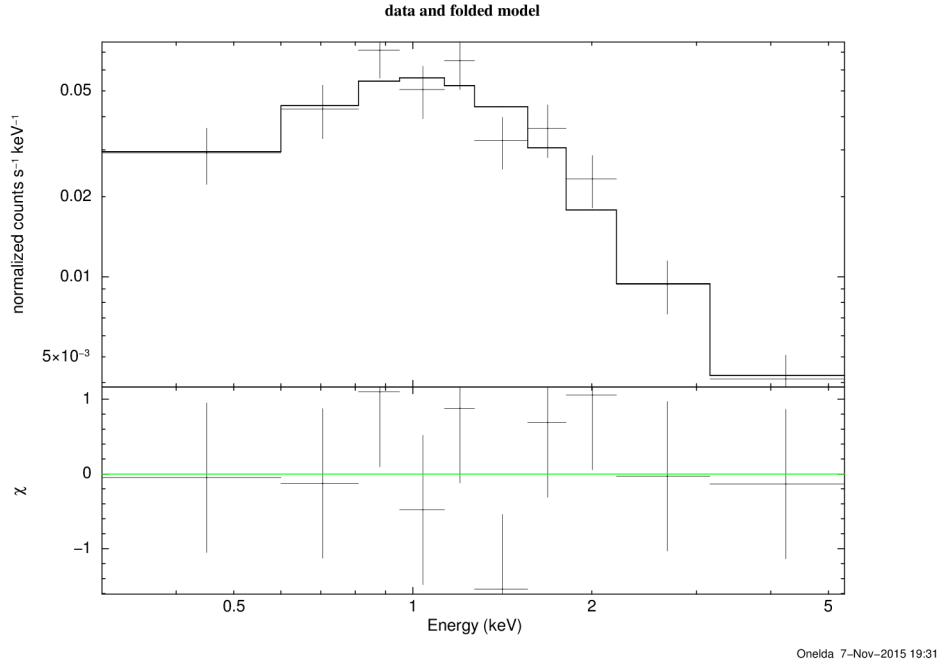
FIGURE 3.10: The X-ray spectrum of the late afterglow during the PC mode.

To check for spectral variation, I did analysis of the hardness ratio (using the hard and soft bands of 2.0-10.0 keV and 0.5-2.0 keV respectively) presented in Fig. 3.11. Checking the last figure we clearly confirm that we do not have spectral variations. While we see at the end of the flare a possible hardening of the spectrum, the error bars are still consistent with no spectral variation at the 3σ level.

Spectral Energy Distribution

Since the aim of this study was the study of GRB 141221A in all wavelengths, and thanks to all instruments that provide for us all the data needed, it was worth checking also the Spectral Energy Distribution (SED) for this GRB. The extraction of SED was done where the observations were the most numerous, at about 611 s post burst (see Fig. 3.3). This corresponds to the end of the flare in X-ray and the decay phase of the optical band. In X-ray, I used the data taken between 350 and 619.7 seconds, and normalized them to the underlying afterglow flux. This last point is important: as there is no hint of flare in the optical light curve, it should not be linked to the X-ray flare. The non-variability of the hardness ratio makes us confident
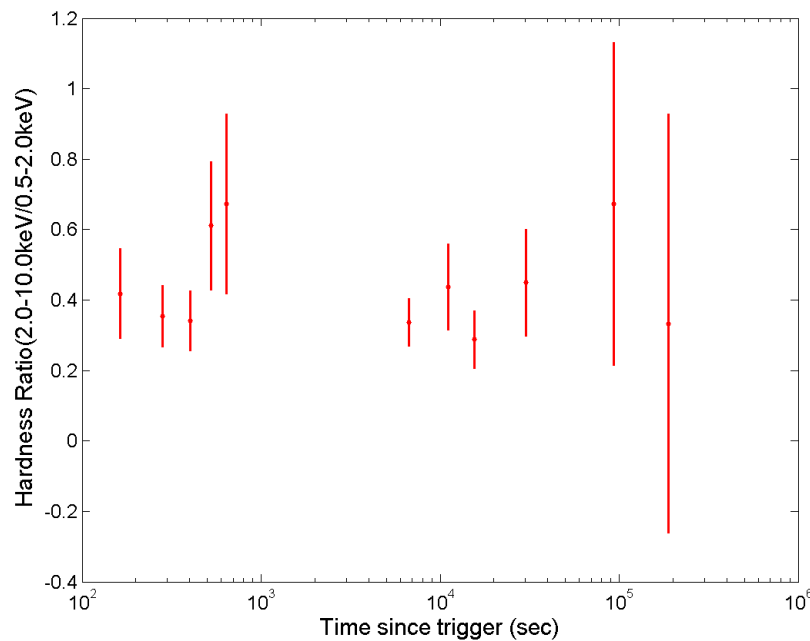
FIGURE 3.11: Hardness ratio of the X-ray observation. We used the hard and soft bands of 2.0-10.0 keV and 0.5-2.0 keV respectively, only in PC mode. Credit: Bardho et al., 2016

that this renormalization is enough to correct for the presence of the flare. Whereas for the optical data are used all data from the GROND and I and V filters from Skynet. All data (including the optical data) were then imported into `xspec` for the spectral fitting. To create the response matrix and ancillary files, in order we do the plot and fit of the SED in the `xspec`, we created a Python script.

To model the SED, I consider a single power law, double power law and the thermal components (see Table 3.6). In all cases, I added foreground absorption by our own Galaxy (this absorption was fixed to the measured values by Kalberla et al., 2005, the optical extinction being corrected before the insertion into `xspec`), and by the distant host galaxy. I consider the three standard extinction laws, i.e. the Milky Way (MW), the Large Magellanic Cloud (LMC) and the Small Magellanic Cloud (SMC) ones. In all cases, the high energy power-law index was allowed to vary freely only within the measured X-ray confidence interval. I first considered a simple power law extincted model. Even if the fit quality seems good (see Table 3.6), an analysis of the residuals shows that this model does not fit the data correctly: exhibits a lack of emission in the soft X-ray part of the SED (see Fig. 3.12). I then inserted a thermal component into the model, and redid the analysis. This time, both the quality indicator of the fit and the residuals are in agreement with a good solution (see Fig. 3.13). I also tested the hypothesis of a cooling break, i.e. a broken power law with the two spectral indices linked together by a difference of 0.5 ($\beta_X = \beta o + 0.5$), which also provides an acceptable fit.

As can be seen, the addition of the optical data strongly constrains the spectral index of the power law to a very low value. On the other hand, from this fit we cannot discriminate between a Galactic and an LMC law of extinction. I present the best-fitting SED (assuming a power-law

TABLE 3.6: Results of the spectral analysis of the SED. β_o is the power law index in case of a single power law. In case of a broken power law, this is the spectral index of the low energy segment, the high energy segment being linked to it by the relation $\beta_X = \beta_o + 0.5$. See text for details. Credit: Bardho et al., 2016

Model	Extinction law	$N_{H,host}$ ($\times 10^{22}$ cm^{-2})	R_V (mag)	$E(B-V)$ (mag)	β_o	Temperature or break energy (keV)	χ^2_ν	d.o.f
pow	MW	0.4 ± 0.3	3.08	0.12 ± 0.02	$0.63^{+0.03}_{-0.02}$	—	0.7674	16
	LMC	0.4 ± 0.3	3.16	0.12 ± 0.02	0.63 ± 0.02	—	0.9855	16
	SMC	0.4 ± 0.3	2.93	0.12 ± 0.02	$0.63^{+0.03}_{-0.02}$	—	1.3111	16
pow+bbody	MW	$1.3^{+1.9}_{-1.0}$	3.08	0.11 ± 0.02	0.63 ± 0.03	$0.14^{+0.17}_{-0.04}$	0.607	14
	LMC	$1.3^{+1.9}_{-1.0}$	3.16	0.12 ± 0.02	0.64 ± 0.03	$0.13^{+0.16}_{-0.05}$	0.862	14
	SMC	1.3 ± 0.9	2.93	0.12 ± 0.02	0.63 ± 0.03	$0.14^{+0.17}_{-0.05}$	1.229	14
cooling break	MW	$0.8^{+0.5}_{-0.4}$	3.08	$0.14^{+0.05}_{-0.04}$	0.5 ± 0.2	< 0.17	0.645	15
	LMC	$0.6^{+0.5}_{-0.3}$	3.16	$0.18^{+0.02}_{-0.06}$	$0.3^{+0.3}_{-0.1}$	$0.012^{+0.8}_{-0.01}$	0.7	15
	SMC	0.7 ± 0.3	2.93	$0.17^{+0.03}_{-0.05}$	$0.37^{+0.03}_{-0.09}$	$0.03^{+1.6}_{-0.028}$	1.15	15
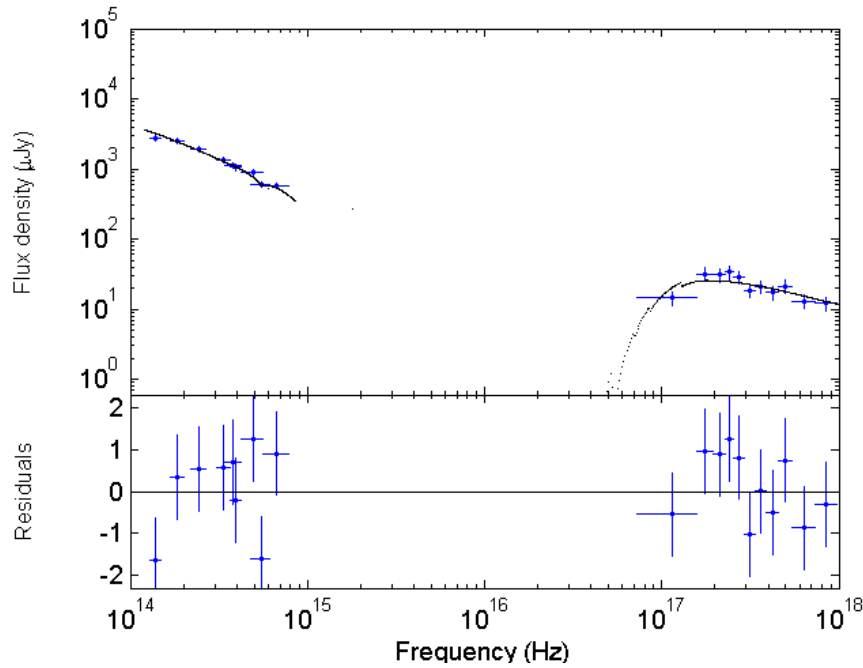
FIGURE 3.12: The fit result for SED. using the LMC extinction law, fit with a simple power law. Credit: Bardho et al., 2016
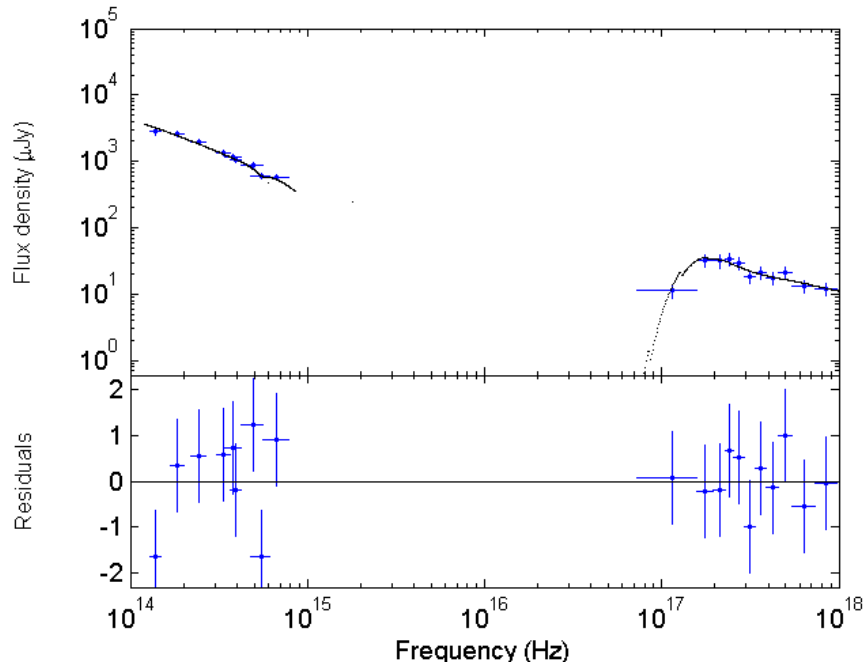
FIGURE 3.13: The best fit result for our SED. using the LMC extinction law. Credit: Bardho et al., 2016

model with an additional thermal component) in Fig. 3.13, using the LMC law, which is more common for GRBs compared to the MW law (Stratta et al., 2004).

3.3.3 Temporal decay

X-ray

The X-ray temporal analysis was already done for the extraction of the SED. The light curve presents a prominent flare, peaking at about 340 seconds (Fig. 3.14), followed by a normal rising in the late afterglow.

The remainder of the afterglow light curve is well fit by a simple power law, as can be seen in Table 3.7.

TABLE 3.7: Best fit temporal decay indices for the I, R, V and X-ray bands. Number in parentheses are not constrained by the fit. See text for details. Credit: Bardho et al., 2016

time (sec)	filter	model	α_1	α_2	α_3	t_{break} (sec)	$t_{break,2}$ (sec)	χ^2_ν	d.o.f
48 - 337	I	broken power law	-1.6 ± 0.9	0.5 ± 0.2	—	110 ± 13	—	1.67	6
337 - 85609	I	broken power law	1.0 ± 0.2	1.6 ± 0.4	—	918 ± 160	—	1.53	9
281 - 2011	R	2 broken power law	1.6 ± 0.4	0.4 ± 3.2	1.3 ± 0.9	540 ± 514	906 ± 696	1.36	1
69 - 205	V	broken power law	(-1.6)	0.1 ± 1.2	—	(109)	—	0.10	1
205 - 85523	V	broken power law	0.7 ± 0.1	1.3 ± 0.3	—	641 ± 125	—	0.70	12
5800 - 191504	X-ray	power law	1.4 ± 0.2	—	—	—	—	1.31	6

FIGURE 3.14: The light curve of the X-ray, where we can see clearly the flare.

Optical

TABLE 3.8: Simple power law decay fit of the I, R, V bands. See text for details. Credit: Bardho et al., 2016

Filter	α	χ^2_ν	d.o.f
I	1.12 ± 0.10	3.83	11
V	0.91 ± 0.10	2.57	14
R	1.04 ± 0.22	10.6	6

The optical light curves are more complex than the X-ray one. They present a rise, a pseudo-plateau and a decay. I split the study in two parts, namely the rising and the decaying parts. These indications are shown schematically in the Fig. 3.3.

For the rising part, I used a broken-power-law model. This gives us the end time of the fast rise and the start of the pseudo-plateau phase. In a few cases, the lack of data prevented an accurate measure, and we indicate these as numbers in parentheses in Table 3.7. This is the case of the R band, which we attribute to an instrumental bias (see below).

For the decay, I first tried a simple-power-law model. As one can see in Table 3.8, this model is strongly rejected in all bands. Then, I inserted a break in the power laws, obtaining good fits in the V and I bands (see Table 3.7).

However, this model, surprisingly, still does not fit the R band. In that band, we need a double-broken-power-law in order to obtain a correct fit. At that point, the degrees of freedom are then too low to ensure a correct measurement of the errors.

This double-broken-power-law model mimics the standard *Swift* X-ray light curve (i.e. a steep-flat-steep shape), but is not seen in the other bands. We explain this feature by the fact that these R band measurements come from the TAROT telescope, which was unfiltered to maximize its sensitivity. We have normalized the magnitudes to the Cousin R band assuming a template afterglow spectrum that does not contain any break. The TAROT CCD camera is sensitive from the I to the V bands (the B sensitivity is very low). As one can see in Table 3.7, a spectral break that appears partly in the observation window will not be accounted for. This can introduce an error in the reduced R magnitude that will depend on the position of the break. If the break is in the blue part of the spectrum, then the R magnitude will be underestimated, and vice-versa for the opposite case. The crossing of the spectral break would then translate into a steep-flat-steep shape in the light curve during the whole time of the crossing. This is not observed for the other bands (I and V) as standard filters have been used. The fits in the V and I bands (decay) are presented in Fig. 3.15.
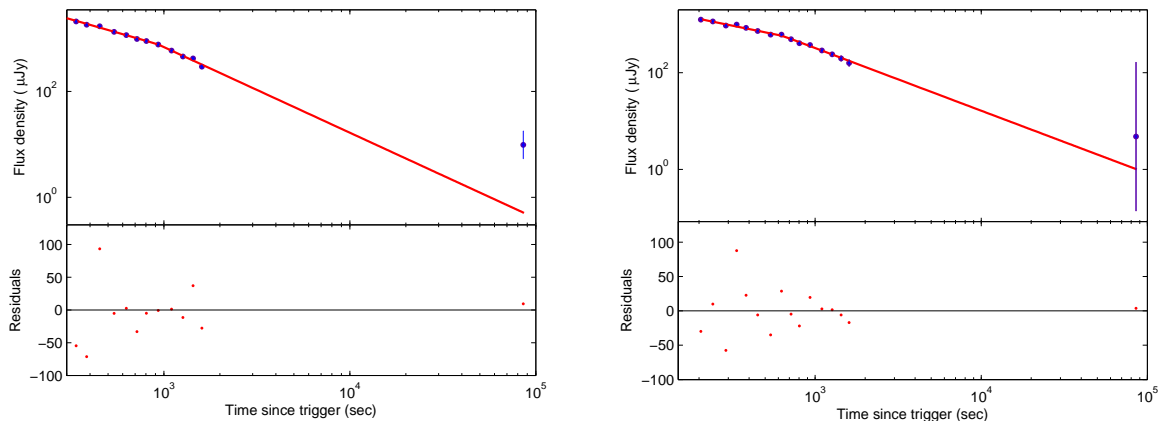
FIGURE 3.15: The best fit in the I (left) and V (right) bands with a power law decay, starting from the end of the pseudo-plateau. The lower parts of each figure show the residual of the fits.
Credit: Bardho et al., 2016

3.4 A very unusual burst

3.4.1 The thermal component

We first consider the possibility that the thermal component seen in the SED is real. This would not be the first time such a component has been observed in the *Swift* era (Sparre and Starling, 2012, Starling et al., 2012). It has been explained either as the shock breakout of the supernova on to the surface of the progenitor or the emission of a hot cocoon protecting the jet during its travel into the progenitor (Butler, 2007). We note incidentally that this last explanation was also proposed to describe the early emission of ultralong GRBs (Gendre et al., 2012, Piro et al., 2014), even if, as in this case, the burst does not belong to that class of events. As no supernova has been reported for GRB 141221A, we do favour the hypothesis of the hot cocoon.

If this component is really present, then the SED indicates that the optical and X-ray emissions are linked together, and are thus due to the same emission mechanism. Indeed, at late times, all

the temporal decay indices are compatible, within errors. However, the SED is extracted before the final break of the I band, and thus this should also apply to earlier measurements. We do not see any evidence of a break in the X-ray light curve: this can be explained by the presence of the flare, which masks out the actual evolution of the afterglow. Moreover, the break times of the I and V magnitudes are compatible, within errors.

This light curve break is then achromatic, which is consistent with a jet break (Rhoads, 1997, 1999). We obtain a value of $p = 1.28 \pm 0.06$ which is extremely low. In addition, the jet break time is also extreme (about 750 s, while a common pre-*Swift* value was of the order of the days Gendre et al., 2006). This would lead to a jet opening angle of 1.3 degrees (assuming the standard law of Sari and Piran, 1999), and could explain why in most cases no jet break is observed for Swift bursts: the break is looked for around a few hours (or days) after the trigger, and not at that earlier time.

In addition to this surprising value of the jet opening angle (that would put strong constraints on the Star Formation Rate of massive stars in the Universe), the only argument against this hypothesis is the R band behaviour, that does not follow the V and I bands. In the previous section, we have explained this behaviour by the fact that the break time was not identical in all bands. If we suppose a constant break time, we cannot explain the R band behaviour.

3.4.2 The rising and early decay of the afterglow

We now assume that the thermal component is not real, and instead use a broken power model of the SED. At a late time, all the temporal decay indices are compatible, within errors. Now, the SED tells us that the X-ray and optical emissions are not linked to the same emission mechanism at the time of the SED (611 s). We can then assume that the various breaks we see are due to the passing through of a specific frequency into the observation bands, and that at a late time ($>$ about 1000 s), the crossing of this frequency has ended and all the emission is due to the same emission mechanism.

The temporal break times in the I and V bands indicate that this specific frequency is decreasing with time, and, as already explained, the R band behaviour is also compatible with that hypothesis. This leads us to exclude the passing through of the cooling frequency in a wind medium, as this frequency increase with time in such a case (Chevalier and Li, 1999, Panaitescu and Kumar, 2000a). If we still assume the wind medium, the only remaining option is the injection frequency, ν_m. However, the spectral index before the crossing ($0.3^{+0.3}_{-0.1}$) would lead to a value of p lower than 1, which is not physical. We thus can conclude that these breaks cannot be explained in the case of the wind medium.

The situation is different in case of the interstellar medium (ISM). There, we can logically assume that the last two breaks are linked to the injection and cooling breaks, respectively. The injection and cooling frequencies varies with $t^{-1.5}$ and $t^{-0.5}$ respectively. Taking into account the errors on the break times, all break measurements are compatible with this explanation. After the cooling break, the spectral and temporal indices are all compatible with a value of $p \sim 2.5 \pm 0.3$. The early spectral index (before the cooling break, as measured in the optical) should be $\beta = 0.7 \pm 0.2$, compatible with the measurement ($0.3^{+0.3}_{-0.04}$). The temporal decay indices are in agreement within the error boxes with the one expected (1.1 ± 0.3).

In that scenario, the end of the "pseudo-plateau" phase is the injection break, i.e. the peak of the afterglow. Again, the variation of the break time between the V and I bands is consistent with this hypothesis. Then, the temporal decay indices of the "pseudo-plateau" should become negative. This does not agree with the model. We explain this by the contribution of a small reverse shock that masks the peak of the emission. We can then, assuming the surrounding medium density to be equal to 1, and the efficiency of the fireball in radiating its energy 30 per cent, compute the microphysics parameters of the fireball, using the work of Panaitescu and Kumar, 2000b. Doing so, we obtain the fireball total energy ($E = 8 \times 10^{52}$ erg), the magnetic parameter ($\varepsilon_B = 5 \times 10^{-2}$) and the electron parameter ($\varepsilon_e = 3 \times 10^{-3}$). These numbers are relatively normal (see e.g. Gendre et al., 2008a), albeit ε_B is slightly higher than usually seen. We thus have a complete description of the afterglow of this burst. We note, however, the total absence of a stellar wind in that model.

Chevalier et al., 2004 have pointed out the complex surrounding medium of a GRB. However, assuming that the progenitor for all long GRBs is a stellar object (Woosley, 1993), we still should observe a small portion of the light curve where a wind environment should be present. Here, from about 200 seconds after the trigger to the end of the observations, the medium is compatible with an ISM only. It is a well-known fact that most of *Swift* bursts are compatible with an ISM, but a degeneracy prevents excluding the wind medium hypothesis (Chevalier et al., 2004). Here, we have the proof that the wind medium is rejected from nearly the start of the afterglow, leaving only extreme constraints on the stellar physics in order to suppress the stellar wind from the progenitor. It is beyond the scope of this paper to introduce such a stellar model; however, GRBs are known to have weak stellar winds (e.g. Gendre et al., 2004, 2012), and thus such a model would be very useful. We conclude this section by noting that the intrinsic values of E_{B-V} and N_H are low, and thus again compatible with a low density around this GRB.

3.4.3 Absorption and Extinction

From our analysis, it turns out that we obtain a better solution using an LMC extinction law, because the observed GROND g-band is best fit by 2175 Å absorption feature present in LMC (and MW). We can note that best-fitting solutions with LMC or MW dust have already been observed (e.g., Kann et al., 2006, 2010, Krühler et al., 2008), even if other models may be more appropriate (Stratta et al., 2004). However, given that these data were obtained from the preliminary photometry quoted in Schweyer et al., 2014, and that it does not have appreciable influence on the fit parameters, we prefer to leave this argument for a future work when better data will be available.

All the spectral models we tried favour a slightly dusty environment with $E(B-V) \sim 0.1 - 0.2$ (see Table 3.6). These values are not unusual (Greiner et al., 2011, Kann et al., 2010, Zafar et al., 2011), most of all at the distance of GRB 141221A (Covino et al., 2013, Kann et al., 2006). The observed $N_{H,host}$ is also in agreement with those found for other bright bursts, especially when compared with the best-fitting optical extinction in the redshift interval $1 < z < 2$ (e.g. Covino et al., 2013, Watson et al., 2013). Like many other bursts, the metals-to-dust ratio ($N_{H,host}/A_V$) is in the range $1 - 3 \times 10^{22}\, cm^{-2}\, mags^{-1}$ (Covino et al., 2013, Krühler et al., 2011, Zafar et al., 2011).

We finally note that the extinction is not enough to set the optical to X-ray spectral slope below the value $\beta_{\mathrm{O-X}} = 0.5$ (see Table 3.6), and thus we cannot consider GRB 141221A as a dark GRB (Jakobsson et al., 2004, Rossi et al., 2012).

3.5   Conclusions

We have analysed the observations of GRB 141221A made in optical and high-energy bands by various instruments, including TAROT and Skynet. In X-ray bands, the burst is very similar to all the previous ones observed, with a late flare. In optical bands, however, the light curve shows a rising part, a pseudo-plateau phase, and various temporal breaks. We explained these breaks as due to the passing through of several specific frequencies into the optical bands. We need a minimal contribution by a reverse shock to completely explain both the optical and X-ray light curves and spectra.

An alternative hypothesis would be the presence of a thermal component, to explain the observed optical/X-ray SED. In this case the last temporal break observed would be due to a jet effect. This, however, would lead to various properties being, while not formally forbidden by the model, extreme and, in addition, would lead to the presence of a thermal emission in the soft X-ray band. All these facts are unusual and difficult to explain.

Clearly, both solutions are challenging for GRB models. In the former case, all the data points towards an absence of stellar winds during the whole phenomenon, which is in contradiction with the current models. In the latter case, the microphysics parameters obtained by the model are very unusual, and in some cases not really taken into account by the model. GRB 141221A should thus be added to the short list of very constraining bursts against which each new model should be tested.

Chapter 4

Prompt and afterglow properties

During the pre-*Swift* era, a clustering of light curves was observed in the X-ray, optical and infrared afterglow of gamma-ray bursts. We used a sample of 254 GRB X-ray afterglows to check this fact for the data in the *Swift* era. Following the same procedure as X-ray data analysis given as an example of GRB 141221A, we manually performed the spectrum of every GRB inside our sample. We corrected fluxes for distance, time dilation and losses of energy due to the cosmological effects in order to compare our results with those of the previous works.

We used a flat ΛCMD model of Universe, with $\Omega_m = 0.3$. All errors are quoted at 90 % confidence level.

4.1 Sample Criteria

In order to reach the goal of this study, we had to choose a comprehensive sample with the following properties:

- **GRBs until February 2013**: The study began in September 2013 and the deadline for GRBs was set until February 2013, in order to be sure that all of the information required for every GRB related to our study was known, and that the processing of the sample was stabilized.

- **Long GRBs**: To be consistent with previous work, we chose only long GRBs for our sample.

- **GRBs with known redshift** (until the time we began this study): This condition allows us to use the normalization of the GRBs at redshift 1.

Thus, with all the above criteria, I reached a sample of 254 lGRBs, all with measured distance.

We excluded the GRBs which satisfy the three conditions for short GRBs, explained in the Siellez et al., 2014: 1. Duration in the rest frame smaller than 2 seconds, 2. Spectral index smaller than 2 and 3. GRBs without a plateau phase. This is due to the discussion about some

GRBs, which may be qualified as long ones. We ensured that our sample is not contaminated by short GRBs.

The redshift of the GRBs was taken from Greiner's webpage http://www.mpe.mpg.de/~jcg/grbgen.html, whereas their duration was taken from Holland's webpage http://www.stsci.edu/~sholland/grb/.

232 out of 254 GRBs in the sample are *Swift* bursts and the remaining are pre-*Swift*. We considered the pre-*Swift* burst, because this is a continuation of the work started by Gendre et al., 2008a, but also because there is no contamination of these bursts, since they already show a clustering. We tested only *Swift* bursts, for the influence they may have on the clustering.

The spectral analysis was performed individually for every GRB of the sample, whereas the results for temporal analysis were taken from *Swift*-XRT GRB light curve repository[1].

4.1.1 Time restriction for X–ray afterglow light curves

The X-ray afterglow of GRBs is the most important phase of this study and the spectral data analysis was only performed for this part.

After the launch of the *Swift*, the X-ray afterglow light curves are illustrated by their canonical behaviour. In this case, we used only the X-ray late afterglow, which corresponds to the data of the beginning of the late decay, after the end of the plateau phase. One example is shown in the Fig. 4.1.
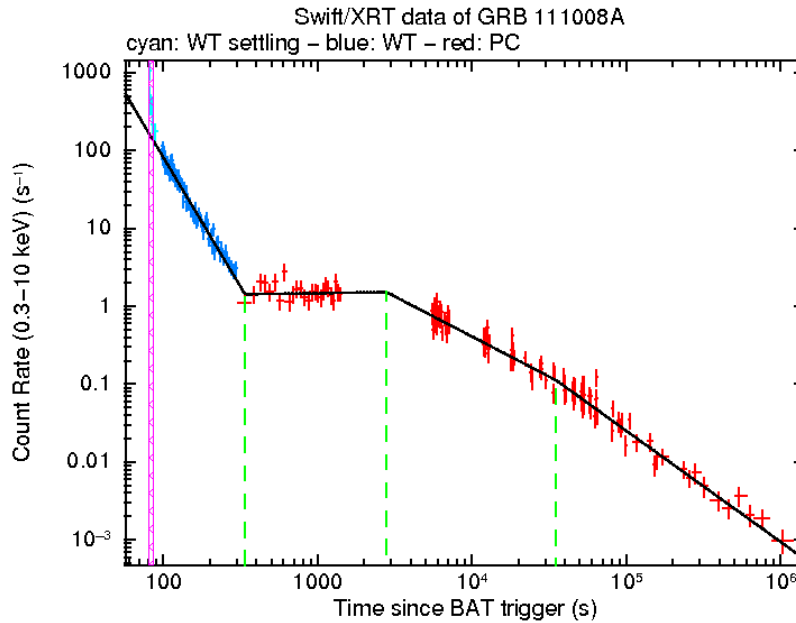
FIGURE 4.1: GRB 111008A which shows the typical canonical behaviour of the X-ray afterglow light curves. Credit: *Swift*/U.K. site

The canonical behaviour is clearly seen for many GRBs but, in several cases, one or more segments are missing. Based on this fact, by screening, I could determine when all of the parts

---

[1] http://www.swift.ac.uk/xrt_curves/

were located inside a canonical shape. These cases are illustrated in different types and Fig. 4.2 represents a typical case.
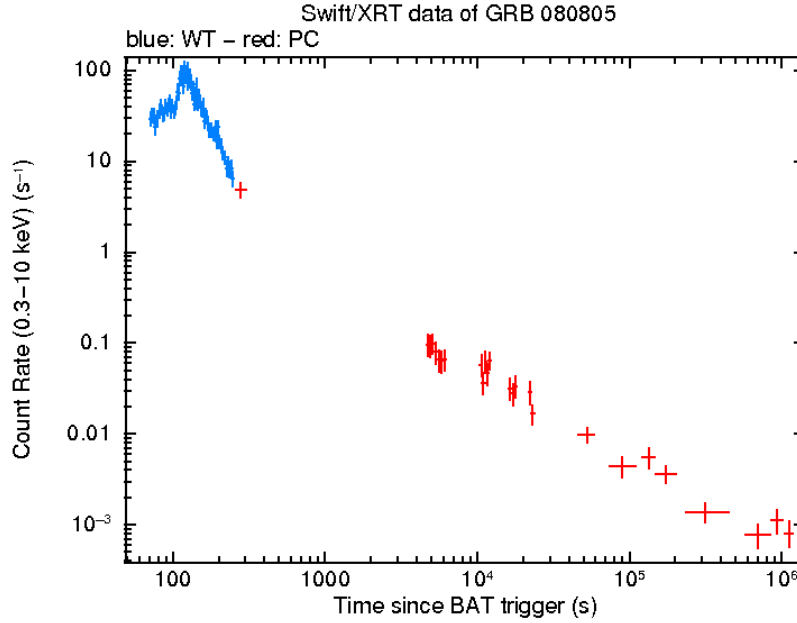
FIGURE 4.2: GRB 080805: we do see only the late decay and the plateau is missing. Credit: *Swift*/U.K. site

In other cases, the light curve displays only one break between the two decaying slopes. I considered the last decay as the late afterglow, see for example Fig. 4.3, which illustrates two different cases of this break.
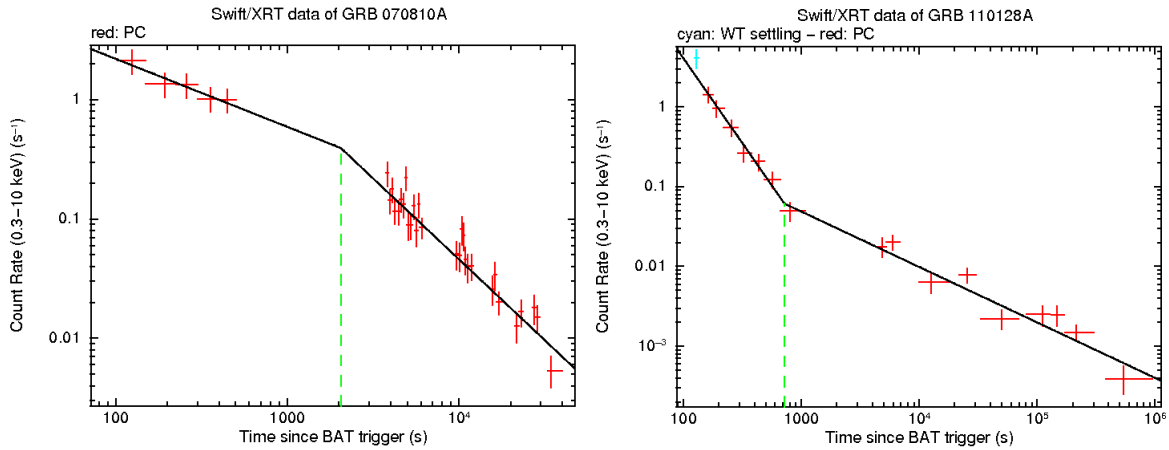
FIGURE 4.3: Two different GRBs which show only one break. Credit: *Swift*/U.K. site

The X-ray afterglow of some GRBs illustrates only one phase of the canonical X-ray afterglow light curve, meaning that there is only one single power law. I considered this as the late afterglow in this case, but only after being sure that it was not the continuation of the prompt emission. The latter examination was made by checking *Swift* Burst Analyzer - BAT-XRT light curves[2], which shows that prompt emission and X-ray afterglow emission are present in the

---

[2]http://www.swift.ac.uk/burst_analyser/

same plot. Two different examples are displayed in the Fig. 4.4 and Fig. 4.5.
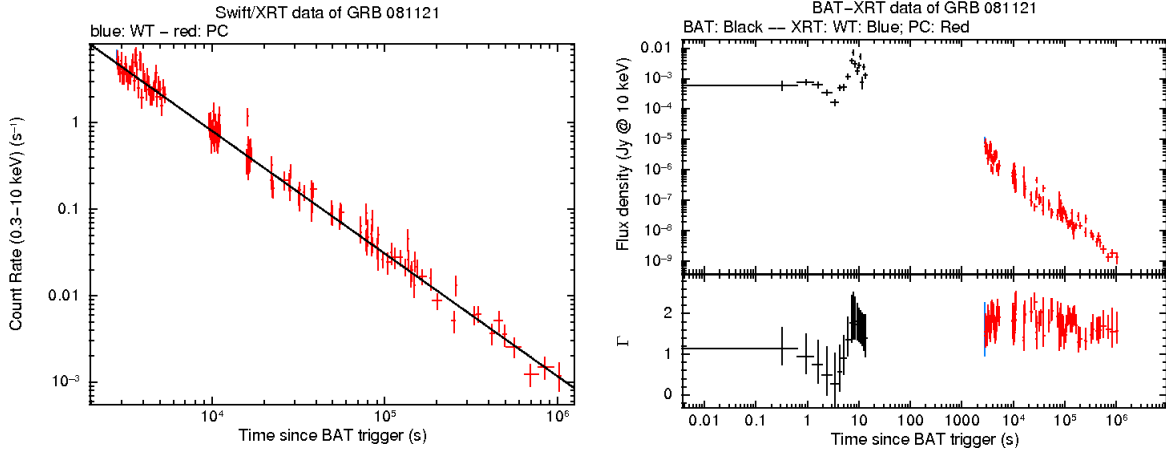
FIGURE 4.4: GRB 081121 which is fit only by a power law in the X-ray afterglow light curves (figure on the left) and the check for not being the continuation of the prompt emission (figure on the right). Credit: *Swift*/U.K. site
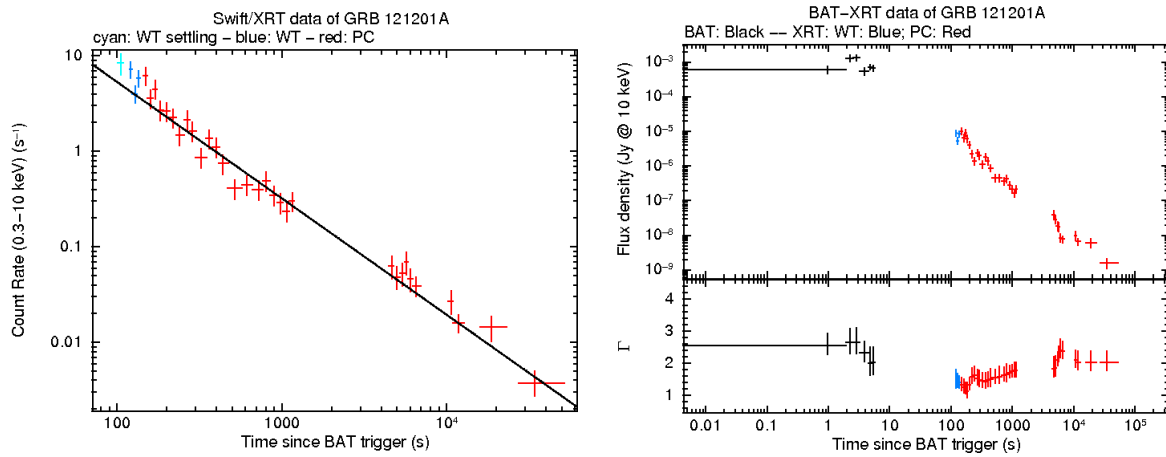
FIGURE 4.5: GRB 121201A which is fit only by a power law in the X-ray afterglow light curves (figure on the left) and the check for not being the continuous part of the prompt emission (figure on the right). The difference with the previous figure is that for this GRB even in the earlier X-ray emission, there is no link with prompt emission. Credit: *Swift*/U.K. site

These plots illustrate that the X-ray emission determined by a single power law is not the continuation of the prompt emission, and it is worth considering it as a late afterglow. I studied late afterglow, and usually the flare is not present. When this was the case, I excluded it.

4.2 Normalization of X–ray afterglow light curves

4.2.1 Boër & Gendre relation

In 2000 Boër and Gendre, 2000 found evidences for a clustering in the X-ray afterglow light curves, by using long GRBs observed with BeppoSAX, GRBs with known redshift. They used

normalized light curves:

- **Distance corrections**: The first normalization made by Boër and Gendre, 2000 was the distance normalization. Since at that time the value of Hubble constant was uncertain, they normalized all GRBs at redshift 1 ($z = 1$); therefore in this case it was able to use the flux at a common redshift rather than using the luminosity. The second normalization was done by assuming a flat universe with $\Omega_m = 0.3$ and the third one by using the k-correction. This also has the advantage to minimize the error made when applying the k-correction.

- **Correction for time dilation**: The same correction was also made for the time in order to be consistent with the normalization at a common distance in the rest frame.

- **Energy band**: The light curves were used inside an energy band $2.0 - 10.0\,\text{keV}$ in order to neglect the absorption due to the ISM.

Boër and Gendre, 2000 found evidence about a clustering in two classes for X-ray afterglow light curves from BeppoSAX data. This work was extended by Gendre and Boër, 2005, Gendre et al., 2008a. After the launch of *Swift*, Gendre et al., 2008a used only the late afterglow light curve, starting at the end of the plateau phase. Fig. 4.6 displays this clustering which consists of three different groups: Gr. I - bright afterglows with a mean Flux $= 7.0 \times 10^{-12} erg\,s^{-1}\,cm^{-2}$, Gr. II - dimmer afterglows with a mean Flux $= 3.1 \times 10^{-12} erg\,s^{-1}\,cm^{-2}$ and faint afterglows that correspond to the Gr. III or outliers/outsiders (a detailed study of this group can be found in Dereli, 2015, Dereli et al., 2015).
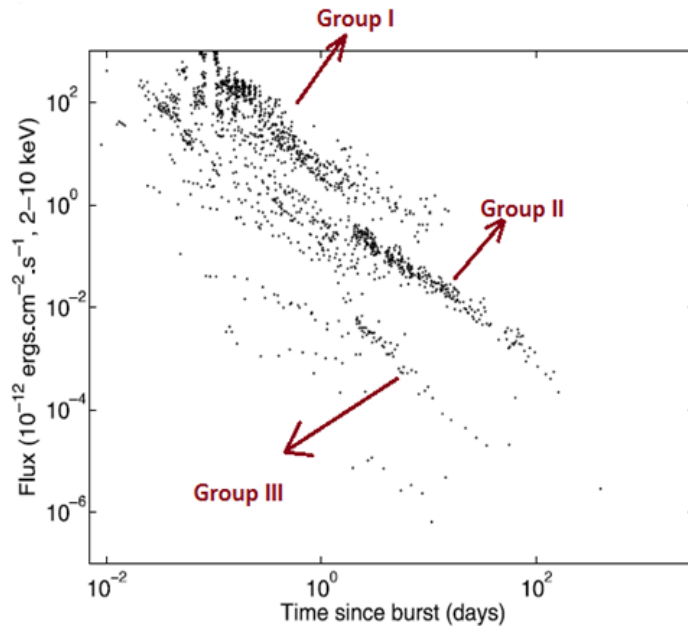
FIGURE 4.6: The presentation of clustering. Credit: Gendre et al., 2008a

Independently from these works Kouveliotou et al., 2004 found the same clustering in X-ray afterglows. This clustering was also seen in optical (Liang and Zhang, 2006, Nardini et al., 2006) and infrared (Gendre et al., 2008b).

4.2.2   k-correction

It is necessary to know what energy the GRBs release in their co-moving rest frame. The factor that accounts for the redshift of the GRB is k-correction. Bloom et al., 2001 calculated this effect. They started by considering the relation of the bolometric energy (E_{bol}) and fluence (S_{bol}) as:

$$E_{bol} = \frac{4\pi D_L^2}{1+z} \, S_{bol},\tag{4.1}$$

where D_L is the luminosity distance to the source at redshift z, given in the Eq. 1.27. If we want to determine the energy limits for a fixed band pass, then the Eq. 4.2, will express the isotropic energy and be written as:

$$E_{[E_1,E_2]} = \frac{4\pi D_L^2}{1+z} \, S_{[E_{min},E_{max}]} * k,\tag{4.2}$$

where E_1, E_2 represent the energy band fixed for this study; E_{min}, E_{max} represent the minimum and maximum of the energy the detector uses and k represents the k-correction, which is given by the formula:

$$k(z) = \frac{\int_{E_{min}/(1+z)}^{E_{max}/(1+z)} E \, N_E(E) \, dE}{\int_{E_{min}}^{E_{max}} E \, N_E(E) \, dE},\tag{4.3}$$

with $N_E(E)$, being the energy spectrum of the GRB. For the observer the fluence is: $S_{obs} \equiv S_{[E_{min},E_{max}]} = \int_{E_{min}}^{E_{max}} E N_E \, dE$.

The calculation of the Eq. 4.3 for the late X-ray afterglow emission of GRBs, if the spectral behaviour is considered as a single power law of index β; $N_E(E) = A \, E^{-\beta}$, leads to the k-correction:

$$k(z) = (1+z)^{\beta-2},\tag{4.4}$$

and the same formula but with normalization to redshift (z = 1) would be:

$$k(z=1) = \left(\frac{1+z}{1+1}\right)^{\beta-2}.\tag{4.5}$$

This formula is not the same for the prompt emission of the GRB, since its spectral behaviour is modeled by the Band function in the Eq. 1.1.
The error for the k-correction is given by:

$$\Delta k(z) = k(z) \, ln(1+z) * \Delta\beta.\tag{4.6}$$

Hence we reduce the uncertainties of the measurements, and increase the accuracy of the results. The error of the k-correction of this situation is:

$$\Delta k(z=1) = k(z=1) \, ln\left(\frac{1+z}{2}\right) * \Delta\beta.\tag{4.7}$$

Let us consider that we have a burst observed at z = 2, with a spectral index $\beta = 1.0 \pm 0.4$. The absolute k-correction for this burst will be $k = 0.33 \pm 0.15$, with an uncertainty around 44%; whereas the k-correction normalized at the z = 1 will be $k = 0.67 \pm 0.11$ with an uncertainty

of 16%. This simple example clearly shows the need to use a median redshift rather than the rest frame. As we can see from the above formula, the k-correction is highly sensitive to β and directly linked with its error. This is not a surprise since the k-correction is directly linked to the distribution of the energy, thus to the spectral index β.

4.2.3 Correction for the time dilation

The time dilation is one of the known cosmological effects from celestial objects. It describes the difference of the elapsed time between the rest frame and the observer frame. This relation is expressed by the formula:

$$t_{rest} = \frac{t_{obs}}{1+z},\tag{4.8}$$

where the t_{rest} and t_{obs} represent the time in the rest frame and in the observer frame respectively, for the same object. We used normalization for this correction as well. The normalization is the same as the one explained above, all GRBs normalized at a common distance. Thus we calculated the time of each GRB (the observer time), but at $z = 1$ which is shown by the following formula:

$$\begin{aligned} t_{obs}(z=1) &= t_{rest} * (1+z)_{(z=1)} \\ &= t_{rest} * (1+1), \end{aligned}\tag{4.9}$$

$$\Downarrow$$

$$t_{obs}(z=1) = \frac{t_{obs}}{1+z} * (1+1).\tag{4.10}$$

As we can see the time does not depend on the spectral index, thus the error of time and the error of time normalized at z = 1 does not depend on it.

4.2.4 Energy Correction Factor

The time when the light curves are included in the analysis is important. The process of spectral analysis was done by following the procedure explained in Chapter 2. The region size of the source was smaller than the one explained in Chapter 2 when another source was present near the burst. Subsequently, in order to avoid another contamination, we slightly reduced the size of the source region. Consequently, we reduced the escalation of the flux for the burst studied, by considering the flux coming from other nearby sources. The decrease of the region does not affect much our results, but we might lose some photons from the burst of interest. This loss will mostly take effect in the later times, when the Signal to Noise ratio decreases.

We used the online results from the *Swift* - XRT GRB light curve repository[1] in order to save time. The online results provide the opportunity to have the light curves in the term of the count rate or the flux. The light curves in the count rate units are the best format of our study. This allows us to make further corrections of these light curves that depend on the spectral analysis. The spectral analysis was done by restricting the energy band between 2.0–10.0 keV, where the absorption by the Interstellar Medium is negligible.

The Energy Correction Factor (ECF) gives the flux of the burst for a given energy from the number of the counts along this energy range:

$$ECF = \frac{Flux_{obs,[E1,E2]}}{CR_{[E1,E2]}}, \tag{4.11}$$

where E_1, E_2 represent the minimum and maximum energy of the required band pass (in our case it was $E_1 = 2.0\,\text{keV}$, $E_2 = 10.0\,\text{keV}$). The flux is found after fitting the spectrum with the best fit.

This coefficient allows us to convert the light curves from count rate units to the flux units:

$$F_{lc,obs} = CR_{lc,d} * ECF, \tag{4.12}$$

where $F_{lc,obs}$ represents the light curve in the Flux units and $CR_{lc,d}$ represents the light curve downloaded from the *Swift*-XRT GRB light curve repository, in units of count rate.

4.3 Distance correction

The last correction we had to make is related with the flux. The normalization of this flux at a common redshift z = 1 was the last step after having found the observed flux of every GRB. The relation between the flux (F) and the luminosity (L) is:

$$L = F * 4\pi D_L^2(z), \tag{4.13}$$

where D_L is the luminosity distance given at Eq. 1.27. Therefore observed flux at the z = 1 is:

$$
\begin{aligned}
F_{obs}(z = 1) &= \frac{L}{4\pi D_L^2(z = 1)} \\
&= F * \frac{4\pi D_L^2(z)}{4\pi D_L^2(z = 1)} \\
&= \frac{F_{lc,obs} * k(z) * 4\pi D_L^2(z)}{4\pi D_L^2(z = 1) * k(z = 1)},
\end{aligned}
\tag{4.14}
$$

where $F_{lc,obs}$ and k are given in the Eq. 4.12 and Eq. 4.7 respectively. After making all the calculations, the observed flux at z = 1 is:

$$F_{obs}(z = 1) = F_{lc,obs} * \left(\frac{d_L(z)}{d_L(z = 1)} \right)^2 * \left(\frac{1+z}{1+1} \right)^{\beta}. \tag{4.15}$$

4.4 Data analysis results

The results for 57 GRBs out of 254 GRBs of this large sample are drawn from Gendre et al., 2008a, whereas the remaining are performed from my spectral analysis, done manually for every GRBs. All these parameters are shown in Table 4.1. In some cases, the afterglow of a GRB was too faint, thus it was not able to fit with a proper model. In these cases we used a default

spectral index = 0.8, an intrinsic column density around $0.5 \times 10^{21} cm^{-2}$ and a normalization 1, creating in this way a theoretical model with default parameters. This method was needed to find the ECF of the GRB, and later on for the creation of the light curves in terms of fluxes and to find the flux at one day for the respective GRBs. In the Table 4.1 the parameters for the GRBs fit with the last method are shown in square brackets.

TABLE 4.1: All the parameters for the 254 GRBs.

Name	**Redshift**	**log(T_a)** (sec)	β	N_H^{int} $(10^{22}\,cm^{-2})$	χ_ν^2	**dof**
GRB 970228[3]	0.695	...	1.0 ± 0.3	...	...	...
GRB 970508[3]	0.835	...	1.4 ± 0.3	...	...	...
GRB 971214[3]	3.42	...	1.1 ± 0.4	...	...	...
GRB 980425[3]	0.0085	...	(1.1)	...	...	...
GRB 980613[3]	1.096	...	(1.1)	...	...	..
GRB 980703[3]	0.966	...	1.7 ± 0.3	...	...	...
GRB 990123[3]	1.60	...	1.0 ± 0.1	...	...	...
GRB 990510[3]	1.619	...	1.2 ± 0.1	...	...	...
GRB 991216[3]	1.02	...	0.7 ± 0.2	...	...	...
GRB 000210[3]	0.846	...	0.9 ± 0.2	...	...	...
GRB 000214[3]	0.47	...	1.0 ± 0.3	...	...	...
GRB 000926[3]	2.066	...	0.7 ± 0.2	...	...	...
GRB 010222[3]	1.477	...	1.0 ± 0.06	...	...	...
GRB 011121[3]	0.36	...	(1.1)	...	...	...
GRB 011211[3]	2.14	...	1.3 ± 0.3	...	...	...
GRB 020405[3]	0.69	...	1.0 ± 0.2	...	...	...
GRB 020813[3]	1.25	...	0.83 ± 0.06	...	...	...
GRB 021004[3]	2.33	...	1.01 ± 0.07	...	...	...
GRB 030226[3]	1.98	...	0.9 ± 0.3	...	...	...
GRB 030328[3]	1.52	...	1.1 ± 0.2	...	...	...
GRB 030329[3]	0.168	...	1.0 ± 0.2	...	...	...
GRB 031203[3]	0.105	...	0.8 ± 0.2	...	...	...
GRB 050126[3]	1.29	$2.34^{+3.30}_{-1.00}$	0.7 ± 0.7	...	...	...
GRB 050215B	2.62	4.0	[0.8]	[0.05]	...	...
GRB 050223[3]	0.5915	...	1.4 ± 0.7	...	...	...
GRB 050315[3]	1.949	4.39 ± 0.27	0.91 ± 0.09	...	...	...
GRB 050318	1.44	4.00	0.91 ± 0.07	0	0.80	47
GRB 050319[3]	3.24	4.67 ± 0.27	0.96 ± 0.09	...	...	...
GRB 050401[3]	2.9	$3.87^{+0.24}_{-0.18}$	1.0 ± 0.3	...	...	...
GRB 050408	1.2357	4.00	$1.12^{+0.17}_{-0.15}$	$1.27^{+0.33}_{-0.26}$	1.02	34
GRB 050505[3]	4.27	$4.39^{+0.48}_{-0.24}$	1.0 ± 0.1	...	...	...
GRB 050525[3]	0.606	$2.92^{+0.14}_{-1.23}$	1.1 ± 0.1	...	...	...
					Continued on next page	

---

[3]Results taken from Gendre et al., 2008a

Table 4.1 – continued from previous page

Name	Redshift	$\log(T_a)$ (sec)	β	N_H^{int} $(10^{22}\,cm^{-2})$	χ_ν^2	dof
GRB 050603[3]	2.821	$4.83^{+0.30}_{-1.14}$	0.7 ± 0.1	...	...	...
GRB 050730[3]	3.967	4.13 ± 0.08	0.62 ± 0.05	...	...	...
GRB 050801	1.38	4.00	$0.79^{+0.15}_{-0.17}$	0	0.77	4
GRB 050802[3]	1.71	3.96 ± 0.10	0.81 ± 0.09	...	...	...
GRB 050814[3]	5.3	$3.93^{+0.56}_{-0.70}$	0.7 ± 0.1	...	...	...
GRB 050819	2.5043	4.48	[0.8]	[0.05]	...	...
GRB 050820A	2.612	3.79	$0.94^{+0.05}_{-0.14}$	$0.23^{+0.15}_{-0.14}$	0.95	205
GRB 050822	1.434	4.23	$1.10^{+0.18}_{-0.16}$	$0.58^{+0.26}_{-0.21}$	1.02	27
GRB 050824[3]	0.83	$4.82^{+1.84}_{-0.54}$	0.82 ± 0.20	...	...	...
GRB 050826[3]	0.297	...	1.1 ± 0.4	...	...	...
GRB 050904	6.29	5.0	[0.8]	[0.05]	...	...
GRB 050908[3]	3.344	$3.31^{+0.86}_{-1.29}$	0.65	...	...	
GRB 050915A	2.5273	4.00	0.72 ± 0.26	0	0.5	4
GRB 051001	2.4296	4.18	[0.8]	[0.05]	...	...
GRB 051006	1.059	3.48	0.44 ± 0.35	0	1.16	60
GRB 051016B[3]	0.9364	$3.51^{+0.64}_{-0.84}$	0.91 ± 0.2	...	...	...
GRB 051022	0.8	5.40	$1.14^{+0.18}_{-0.17}$	$3.41^{+0.59}_{-0.52}$	0.89	50
GRB 051109A[3]	2.346	$3.93^{+0.15}_{-0.23}$	1.0 ± 0.2	...	...	...
GRB 051109B[3]	0.08	$3.67^{+0.27}_{-0.40}$	0.7 ± 0.4	...	...	...
GRB 051111[3]	1.55	...	1.1 ± 0.4	...	...	...
GRB 051117B	0.481	4.00	[0.8]	[0.05]	...	...
GRB 060108[3]	2.03	4.40 ± 0.20	0.93 ± 0.30	...	...	...
GRB 060111A	2.32	3.6	$1.07^{+0.17}_{-0.15}$	$1.3^{+0.60}_{-0.48}$	0.99	27
GRB 060115[3]	3.53	$3.86^{+1.61}_{-1.00}$	1.3 ± 0.3	...	...	...
GRB 060123	0.56	...	$1.0^{+0.12}_{-0.13}$	$0.20^{+0.42}_{-0.14}$	0.85	25
GRB 060124	2.296	4.18	$0.99^{+0.09}_{-0.08}$	$0.28^{+0.31}_{-0.28}$	0.81	84
GRB 060202	0.783	3.6	$2.12^{+0.20}_{-0.18}$	$1.94^{+0.27}_{-0.23}$	1.13	47
GRB 060210[3]	3.91	$4.46^{+0.33}_{-0.29}$	1.0 ± 0.09	...	...	...
GRB 060218[3]	0.0331	$5.01^{+0.63}_{-0.48}$	0.51 ± 0.05	...	...	...
GRB 060223A[3]	4.41	$2.73^{+0.32}_{-0.36}$	0.9 ± 0.3	...	...	...
GRB 060319	1.172	4.19	$1.08^{+0.22}_{-0.20}$	$1.80^{+0.56}_{-0.44}$	0.8	28
GRB 060418[3]	1.489	$3.44^{+0.14}_{-0.18}$	0.51 ± 0.90	...	...	...
GRB 060502A	1.51	4.42	$1.30^{+0.71}_{-0.60}$	$0.85^{+1.08}_{-0.77}$	0.6	3
GRB 060505	0.089	4.6	[0.8]	[0.05]	...	...
GRB 060510B[3]	4.94	$4.55^{+0.60}_{-0.54}$	1.7 ± 0.4	...	...	...
GRB 060512[3]	2.1	$3.85^{+0.34}_{-1.00}$	0.91 ± 0.20	...	...	...
GRB 060522[3]	5.11	$2.86^{+0.46}_{-0.25}$	1.1 ± 0.2	...	...	...
GRB 060526[3]	3.221	$3.84^{+0.47}_{-0.33}$	0.7 ± 0.3	...	...	...
GRB 060604[3]	2.1357	4.55 ± 0.29	1.3 ± 0.2	...	...	...
GRB 060605[3]	3.78	4.16 ± 0.13	1.0 ± 0.1	...	...	...

Continued on next page

Table 4.1 – continued from previous page

Name	Redshift	$\log(T_a)$ (sec)	β	N_H^{int} $(10^{22}\,cm^{-2})$	χ^2_ν	dof
GRB 060607A[3]	3.082	4.75 ± 0.03	0.86 ± 0.09	...	...	...
GRB 060614[3]	0.125	5.00 ± 0.09	0.8 ± 0.2	...	...	...
GRB 060707[3]	3.425	$3.58^{+0.47}_{-0.71}$	1.2 ± 0.5	...	...	...
GRB 060708	1.92	3.90	$1.06^{+0.15}_{-0.14}$	$0.18^{+0.25}_{-0.18}$	1.08	35
GRB 060714[3]	2.711	$3.20^{+0.21}_{-0.41}$	1.4 ± 0.3	...	...	...
GRB 060719	1.5320	4.00	$1.22^{+0.26}_{-0.23}$	$1.71^{+0.79}_{-0.54}$	0.99	22
GRB 060729[3]	0.54	5.11 ± 0.04	1.39 ± 0.05	...	...	...
GRB 060814	1.9229	3.75	$1.12^{+0.09}_{-0.08}$	$1.08^{+0.14}_{-0.13}$	1.03	96
GRB 060904B	0.703	3.72	$1.28^{+0.23}_{-0.21}$	$0.37^{+0.17}_{-0.14}$	0.99	21
GRB 060906	3.686	4.08	$0.76^{+0.43}_{-0.38}$	$0.4^{+2.0}_{-0.4}$	1.14	8
GRB 060908	1.8836	2.90	$0.80^{+0.33}_{-0.35}$	0	0.7	3
GRB 060912A	0.937	3.85	0.61 ± 0.27	$0.31^{+0.82}_{-0.20}$	0.94	45
GRB 060927	5.47	3.23	$1.05^{+0.22}_{-0.21}$	$0.06^{+0.05}_{-0.06}$	0.7	7
GRB 061007	1.261	5.02	$0.94^{+0.34}_{-0.33}$	0	0.99	50
GRB 061021	0.3463	3.64	$0.99^{+0.11}_{-0.10}$	$0.07^{+0.04}_{-0.04}$	1.093	56
GRB 061110A	0.758	4.86	$0.95^{+0.77}_{-0.55}$	$0.52^{+1.25}_{-0.48}$	0.99	62
GRB 061110B	3.44	3.30	$0.96^{+0.41}_{-0.34}$	$1.93^{+2.69}_{-1.93}$	1.13	6
GRB 061121	1.314	2.93	$0.92^{+0.08}_{-0.07}$	$0.62^{+0.14}_{-0.12}$	0.91	106
GRB 061126	1.1588	5.06	0.69 ± 0.26	0	0.6	4
GRB 061210	0.4095	5.3	[0.8]	[0.05]	...	...
GRB 061222A	2.088	3.49	$1.07^{+0.13}_{-0.12}$	$4.07^{+0.86}_{-0.73}$	1.15	56
GRB 061222B	3.355	3.70	[0.8]	[0.05]	...	...
GRB 070103	2.6208	3.27	$1.14^{+0.33}_{-0.30}$	$4.07^{+2.08}_{-1.56}$	0.84	10
GRB 070110	2.352	4.66	$1.03^{+0.45}_{-0.43}$	0	0.72	40
GRB 070125	1.547	5.07	$0.97^{+0.27}_{-0.28}$	0	0.62	4
GRB 070129	2.3384	4.12	$1.02^{+0.16}_{-0.15}$	$1.24^{+0.64}_{-0.52}$	0.86	23
GRB 070208	1.165	3.06	$1.09^{+0.24}_{-0.22}$	$0.77^{+0.39}_{-0.28}$	1.11	12
GRB 070306	1.497	4.5	$1.20^{+0.25}_{-0.23}$	$3.74^{+1.15}_{-0.89}$	0.84	21
GRB 070318	0.836	3.86	$1.16^{+0.17}_{-0.16}$	$0.75^{+0.18}_{-0.15}$	0.8	39
GRB 070411	2.954	2.00	$1.26^{+0.30}_{-0.26}$	$2.03^{+3.26}_{-2.03}$	1.03	11
GRB 070419A	0.97	4.48	[0.8]	[0.05]	...	...
GRB 070419B	1.9591	3.90	0.56 ± 0.11	$0.64^{+0.40}_{-0.34}$	0.94	50
GRB 070508	0.82	3.07	$0.90^{+0.24}_{-0.22}$	$0.91^{+0.40}_{-0.31}$	0.93	15
GRB 070521	1.350	3.19	$1.03^{+0.15}_{-0.14}$	$1.94^{+0.28}_{-0.25}$	1.2	55
GRB 070529	2.4996	3.19	$0.72^{+0.44}_{-0.35}$	$1.14^{+2.80}_{-1.14}$	1.14	5
GRB 070611	2.04	4.55	[0.8]	[0.05]	...	...
GRB 070714A	1.58	4.00	[0.8]	[0.05]	...	...
GRB 070721B	3.626	3.97	$0.61^{+0.12}_{-0.10}$	$1.15^{+0.82}_{-0.71}$	0.93	42
GRB 070802	2.45	3.91	$1.23^{+0.67}_{-0.54}$	$0.71^{+2.20}_{-0.71}$	0.82	50
GRB 070810A	2.17	3.22	$1.12^{+0.22}_{-0.20}$	$0.85^{+0.55}_{-0.45}$	0.80	17

<div align="center">

Table 4.1 – continued from previous page

Name	Redshift	$\log(T_a)$ (sec)	β	N_H^{int} $(10^{22}\,cm^{-2})$	χ_ν^2	dof
GRB 071003	1.60435	4.54	0.83 ± 0.13	0	1.19	13
GRB 071010A	0.98	4.83	$0.56^{+0.60}_{-0.47}$	$0.51^{+1.58}_{-0.51}$	0.7	3
GRB 071010B	0.947	3.70	$0.46^{+0.36}_{-0.39}$	0	0.73	3
GRB 071021	2.4520	4.00	$0.80^{+0.28}_{-0.25}$	$0.97^{+1.21}_{-0.89}$	0.84	12
GRB 071025	5.2	3.55	1.17 ± 0.09	$2.80^{+1.33}_{-1.19}$	0.85	80
GRB 071031	3.19	3.19	$0.74^{+0.24}_{-0.23}$	0	0.7	107
GRB 071112C	0.8230	4.00	$0.85^{+0.37}_{-0.32}$	$0.21^{+0.42}_{-0.21}$	0.91	6
GRB 071117	1.331	3.59	$1.04^{+0.26}_{-0.22}$	$1.19^{+0.60}_{-0.43}$	0.8	14
GRB 071122	1.14	2.90	0.92 ± 0.30	0	0.7	4
GRB 080129	4.349	4.10	$0.97^{+0.97}_{-0.52}$	$17.59^{+60.40}_{-17.59}$	0.96	8
GRB 080207	2.0858	2.41	$1.28^{+0.17}_{-0.16}$	$10.50^{+1.85}_{-1.63}$	0.85	45
GRB 080210	2.641	3.84	1.08 ± 0.15	0	1.2	16
GRB 080310	2.42	4.00	$0.85^{+0.16}_{-0.15}$	$0.32^{+0.50}_{-0.32}$	1.03	27
GRB 080319B	0.937	3.48	$0.80^{+0.12}_{-0.11}$	$0.05^{+0.08}_{-0.05}$	0.8	38
GRB 080319C	1.95	3.66	$1.30^{+0.69}_{-0.57}$	$0.73^{+1.18}_{-0.73}$	0.83	3
GRB 080330	1.51	4.00	$1.15^{+0.25}_{-0.22}$	$0.42^{+0.26}_{-0.22}$	0.89	19
GRB 080411	1.03	4.26	$1.24^{+0.05}_{-0.04}$	$0.42^{+0.26}_{-0.22}$	0.89	19
GRB 080413A	2.433	4.00	[0.8]	[0.05]	...	...
GRB 080413B	1.10	2.81	$0.94^{+0.09}_{-0.08}$	$0.36^{+1.28}_{-0.36}$	0.8	119
GRB 080430	0.767	4.15	$1.03^{+0.12}_{-0.11}$	$0.37^{+0.09}_{-0.08}$	0.93	48
GRB 080514B	1.8	4.48	0.83 ± 0.17	0	1.09	11
GRB 080515	2.47	5.00	[0.8]	[0.05]	...	...
GRB 080603A	1.688	3.95	$1.36^{+0.32}_{-0.28}$	$0.62^{+0.51}_{-0.40}$	0.84	13
GRB 080603B	2.69	3.6	0.86 ± 0.21	0	0.62	9
GRB 080604	1.416	5.00	[0.8]	[0.05]	...	...
GRB 080605	1.6398	3.26	$0.90^{+0.17}_{-0.15}$	$0.69^{+0.47}_{-0.35}$	0.94	21
GRB 080607	3.036	3.37	1.11 ± 0.12	$2.45^{+0.63}_{-0.55}$	0.92	49
GRB 080707	1.23	3.90	$1.10^{+0.41}_{-0.36}$	$0.39^{+0.64}_{-0.39}$	0.89	4
GRB 080710	0.845	3.78	$1.06^{+0.17}_{-0.15}$	$0.07^{+0.09}_{-0.07}$	1.03	35
GRB 080721	2.591	3.29	$0.94^{+0.09}_{-0.08}$	$0.22^{+0.32}_{-0.22}$	1.17	98
GRB 080804	2.2045	2.7	$0.85^{+0.10}_{-0.06}$	$0.02^{+0.19}_{-0.02}$	0.82	54
GRB 080805	1.505	3.76	$0.89^{+0.34}_{-0.30}$	$1.05^{+1.46}_{-0.84}$	1.1	4
GRB 080810	3.35	3.83	$1.15^{+0.21}_{-0.19}$	$0.74^{+0.98}_{-0.74}$	0.72	13
GRB 080825B	4.3	4.6	$1.56^{+0.47}_{-0.44}$	0	0.91	3
GRB 080905B	2.374	3.54	$0.92^{+0.15}_{-0.14}$	$2.18^{+0.71}_{-0.56}$	0.81	36
GRB 080906	2.1	4.09	$0.89^{+0.21}_{-0.18}$	$0.86^{+0.94}_{-0.64}$	1.09	15
GRB 080916A	0.689	4.52	$0.40^{+0.21}_{-0.18}$	0	1.06	66
GRB 080916C	4.35	4.23	$0.6^{+0.33}_{-0.32}$	0	0.85	73
GRB 080928	1.692	3.97	1.17 ± 0.17	0	0.83	9
GRB 081007	0.5295	4.44	$1.38^{+0.51}_{-0.43}$	$0.60^{+0.37}_{-0.27}$	0.89	6

</div>

<div align="center">

Table 4.1 – continued from previous page

</div>

Name	Redshift	log(T_a) (sec)	β	N_H^{int} ($10^{22}\,cm^{-2}$)	χ_ν^2	dof
GRB 081008	1.9685	2.81	$0.99^{+0.14}_{-0.13}$	$0.30^{+0.33}_{-0.28}$	0.92	40
GRB 081028	3.038	4.90	$0.86^{+0.34}_{-0.32}$	0	0.82	3
GRB 081029	3.8479	4.26	1.18 ± 0.30	$1.05^{+1.74}_{-1.05}$	1.12	9
GRB 081109	0.9787	2.85	$1.00^{+0.16}_{-0.14}$	$0.96^{+0.29}_{-0.22}$	0.90	44
GRB 081118	2.58	2.85	$1.43^{+0.28}_{-0.27}$	0	0.98	87
GRB 081121	2.512	3.30	$0.88^{+0.13}_{-0.11}$	$0.12^{+0.36}_{-0.12}$	0.83	36
GRB 081203A	2.05	3.95	0.89 ± 0.12	0	0.94	14
GRB 081221	2.26	2.84	$1.31^{+0.11}_{-0.10}$	$4.97^{+0.71}_{-0.63}$	0.94	14
GRB 081222	2.77	2.85	1.02 ± 0.08	$0.39^{+0.24}_{-0.22}$	1.2	83
GRB 081228	3.4	2.3	1.09 ± 0.40	0	1.16	53
GRB 081230	2.0	4.11	$0.98^{+0.36}_{-0.35}$	0	0.7	51
GRB 090102	1.547	3.08	0.74 ± 0.09	$0.50^{+0.19}_{-0.16}$	1.04	61
GRB 090113	1.7493	2.73	$0.84^{+0.41}_{-0.37}$	$1.64^{+1.75}_{-1.22}$	1.09	105
GRB 090313	3.375	4.3	$1.00^{+0.20}_{-0.18}$	$2.37^{+1.22}_{-1.00}$	1.2	20
GRB 090323	3.57	4.70	$1.18^{+0.34}_{-0.33}$	0	1.05	3
GRB 090328A	0.736	4.70	0.37 ± 0.29	0	0.5	3
GRB 090407	1.4485	3.86	$1.22^{+0.14}_{-0.13}$	$1.68^{+0.39}_{-0.32}$	1.1	42
GRB 090417B	0.345	3.74	$1.04^{+0.13}_{-0.12}$	$2.03^{+0.23}_{-0.21}$	1.07	124
GRB 090418A	1.608	3.41	$0.91^{+0.20}_{-0.18}$	$0.98^{+0.20}_{-0.18}$	0.83	81
GRB 090424	0.544	3.21	$0.95^{+0.13}_{-0.12}$	$0.38^{+0.09}_{-0.08}$	0.90	45
GRB 090516	4.109	4.00	$1.11^{+0.10}_{-0.09}$	$1.48^{+0.71}_{-0.64}$	0.8	6
GRB 090519	3.85	3.07	$0.38^{+0.40}_{-0.38}$	0	0.87	3
GRB 090529	2.625	4.55	[0.8]	[0.05]	...	...
GRB 090530	1.266	4.79	$1.02^{+0.42}_{-0.38}$	$0.48^{+0.55}_{-0.41}$	0.81	90
GRB 090618	0.54	3.21	0.88 ± 0.05	0.17 ± 0.03	0.82	189
GRB 090715B	3.0	5.02	0.51 ± 0.40	$0.007^{+0.005}_{-0.007}$	0.8	41
GRB 090726	2.71	3.34	$1.28^{+0.29}_{-0.26}$	$0.71^{+1.03}_{-0.71}$	0.82	13
GRB 090812	2.452	3.60	$1.06^{+0.31}_{-0.28}$	$1.23^{+1.07}_{-0.80}$	0.7	10
GRB 090814A	0.696	3.02	$0.78^{+0.12}_{-0.11}$	0	1.2	37
GRB 090902B	1.822	4.60	$0.80^{+0.17}_{-0.16}$	$1.44^{+0.65}_{-0.49}$	1.02	35
GRB 090926A	2.1062	4.93	$0.99^{+0.64}_{-0.41}$	$0.20^{+1.19}_{-0.20}$	0.75	54
GRB 090926B	1.24	2.90	$0.70^{+0.22}_{-0.20}$	$2.08^{+0.75}_{-0.60}$	1.11	19
GRB 091003	0.8969	4.70	$0.74^{+0.36}_{-0.33}$	$0.20^{+0.25}_{-0.20}$	1.06	10
GRB 091018	0.971	2.76	1.07 ± 0.12	$0.17^{+0.09}_{-0.08}$	1.1	41
GRB 091020	1.71	3.4	$1.09^{+0.09}_{-0.08}$	$0.50^{+0.13}_{-0.12}$	0.95	78
GRB 091024	1.092	3.8	$0.40^{+0.20}_{-0.18}$	$1.06^{+1.18}_{-0.98}$	1.08	45
GRB 091029	2.752	3.44	$1.10^{+0.11}_{-0.10}$	$0.54^{+0.32}_{-0.31}$	1.26	354
GRB 091109A	3.076	3.00	$0.87^{+0.29}_{-0.23}$	$0.51^{+1.47}_{-0.51}$	0.88	11
GRB 091127	0.490	4.51	0.67 ± 0.09	$2.95^{+0.04}_{-0.03}$	0.98	80
GRB 091208B	1.063	3.10	$0.80^{+0.24}_{-0.21}$	$0.63^{+0.47}_{-0.32}$	0.96	12

<div align="right">

Continued on next page

</div>

Table 4.1 – continued from previous page

Name	Redshift	$\log(T_a)$ (sec)	β	N_H^{int} $(10^{22}\,cm^{-2})$	χ^2_ν	dof
GRB 100219A	4.6667	3.30	0.50 ± 0.18	0	1.03	9
GRB 100302A	4.813	4.42	$0.76^{+0.41}_{-0.26}$	$0.28^{+3.68}_{-0.28}$	1.2	6
GRB 100316D	0.059	4.00	[0.8]	[0.05]	...	...
GRB 100414A	1.368	4.00	0.27 ± 0.27	0	0.98	72
GRB 100418A	0.6235	4.83	$0.94^{+0.60}_{-0.50}$	$0.14^{+0.42}_{-0.14}$	1.09	50
GRB 100424A	2.465	4.00	[0.8]	[0.05]	...	...
GRB 100425A	1.755	3.6	$1.04^{+0.17}_{-0.16}$	0	1.04	11
GRB 100513A	4.772	4.85	[0.8]	[0.05]	...	...
GRB 100615A	1.398	3.47	$1.23^{+0.21}_{-0.19}$	$12.26^{+1.97}_{-1.15}$	0.86	41
GRB 100621A	0.542	3.78	1.34 ± 0.13	$2.22^{+0.25}_{-0.23}$	1.1	88
GRB 100728A	1.567	3.07	$0.75^{+0.77}_{-0.07}$	$1.48^{+0.32}_{-0.27}$	1.12	111
GRB 100728B	2.106	3.55	$1.06^{+0.22}_{-0.21}$	$0.37^{+0.47}_{-0.37}$	0.84	19
GRB 100814A	1.44	5.28	$1.26^{+0.41}_{-0.36}$	$0.41^{+0.44}_{-0.34}$	0.7	6
GRB 100901A	1.408	4.89	0.99 ± 0.19	0	0.7	7
GRB 100906A	1.727	4.04	$0.93^{+0.13}_{-0.12}$	$0.78^{+0.61}_{-0.48}$	1.06	52
GRB 101219B	0.55	4.78	$1.06^{+0.30}_{-0.29}$	0	0.86	59
GRB 101225A	0.847	4.74	[0.8]	[0.05]	...	...
GRB 110106B	0.618	4.04	$1.16^{+0.67}_{-0.56}$	$0.41^{+0.56}_{-0.34}$	0.7	3
GRB 110128A	2.339	3.60	0.75 ± 0.29	$0.36^{+1.20}_{-0.20}$	0.87	64
GRB 110205A	2.22	3.70	1.09 ± 0.11	$0.27^{+0.21}_{-0.19}$	1.31	52
GRB 110213A	1.46	3.17	$1.01^{+0.82}_{-0.08}$	$0.50^{+0.22}_{-0.19}$	0.93	94
GRB 110213B	1.083	4.6	$1.21^{+0.71}_{-0.59}$	$0.78^{+1.15}_{-0.66}$	0.82	54
GRB 110422A	1.77	3.87	0.90 ± 0.12	$1.32^{+0.38}_{-0.33}$	0.98	58
GRB 110503A	1.613	3.30	0.92 ± 0.07	$0.12^{+0.10}_{-0.09}$	0.76	115
GRB 110715	0.82	5.06	$1.19^{+0.50}_{-0.39}$	$1.12^{+1.40}_{-0.86}$	0.96	9
GRB 110731A	2.83	3.93	0.78 ± 0.14	0	0.7	14
GRB 110801A	1.858	4.00	$1.09^{+0.17}_{-0.15}$	$0.40^{+0.35}_{-0.29}$	1.26	22
GRB 110808A	1.348	2.60	$2.08^{+0.30}_{-0.28}$	0	1.5	88
GRB 110818A	3.36	3.90	$1.05^{+0.26}_{-0.24}$	$1.05^{+1.39}_{-1.05}$	1.2	165
GRB 110918A	0.982	5.00	$0.76^{+0.15}_{-0.14}$	$0.20^{+0.13}_{-0.11}$	1.06	38
GRB 111008A	4.9898	3.92	$0.99^{+0.12}_{-0.11}$	$2.44^{+1.49}_{-1.26}$	1.27	36
GRB 111107A	2.893	2.65	0.90 ± 0.22	0	0.94	111
GRB 111123A	3.1516	4.00	$1.29^{+0.22}_{-0.19}$	$1.35^{+1.26}_{-1.00}$	1.08	20
GRB 111209A	0.677	5.18	1.06 ± 0.29	0	0.73	79
GRB 111211A	0.478	4.70	[0.8]	[0.05]	...	...
GRB 111228A	0.714	3.86	$1.08^{+0.17}_{-0.15}$	$0.33^{+0.13}_{-0.11}$	0.92	26
GRB 111229A	1.3805	3.43	$0.88^{+0.16}_{-0.15}$	$0.36^{+0.37}_{-0.27}$	0.98	28
GRB 120118B	2.943	3.43	$0.97^{+0.27}_{-0.24}$	$5.05^{+3.24}_{-2.13}$	1.05	15
GRB 120119A	1.728	4.39	$0.36^{+0.26}_{-0.25}$	0	1.3	86
GRB 120326A	1.798	4.85	$1.14^{+0.37}_{-0.32}$	$0.63^{+0.83}_{-0.61}$	1.16	5

Table 4.1 – continued from previous page

Name	Redshift	$\log(T_a)$ (sec)	β	N_H^{int} $(10^{22}\,cm^{-2})$	χ^2_ν	dof
GRB 120327A	2.813	3.42	$0.66^{+0.37}_{-0.23}$	$0.23^{+2.79}_{-0.23}$	0.8	5
GRB 120404A	2.876	3.48	$1.05^{+0.19}_{-0.18}$	$0.58^{+0.66}_{-0.56}$	0.87	17
GRB 120422A	0.283	5.08	[0.8]	[0.05]	...	...
GRB 120521C	6.00	4.30	[0.8]	[0.05]	...	...
GRB 120711A	1.405	3.86	$0.87^{+0.11}_{-0.10}$	$1.19^{+0.32}_{-0.27}$	1.07	67
GRB 120712A	4.1745	3.30	$1.30^{+0.21}_{-0.19}$	$1.06^{+1.38}_{-1.06}$	1.11	20
GRB 120714B	0.3984	3.85	[0.8]	[0.05]	...	...
GRB 120722A	0.9586	4.00	[0.8]	[0.05]	...	...
GRB 120724A	1.48	4.40	0.70 ± 0.27	0	0.5	4
GRB 120729A	0.80	3.6	$0.86^{+0.12}_{-0.11}$	0	0.94	28
GRB 120802A	3.796	3.06	1.03 ± 0.14	0	0.91	16
GRB 120811C	2.671	3.30	$1.05^{+0.48}_{-0.40}$	$0.59^{+1.16}_{-0.59}$	0.83	6
GRB 120815A	2.358	3.30	0.70 ± 0.12	0	1.04	25
GRB 120907A	0.970	3.17	$0.81^{+0.13}_{-0.12}$	$0.15^{+0.13}_{-0.11}$	0.84	40
GRB 120909A	3.93	4.3	$1.24^{+0.22}_{-0.20}$	$1.30^{+1.78}_{-1.30}$	1.00	17
GRB 120922A	3.1	3.39	$0.97^{+0.14}_{-0.13}$	$0.43^{+0.69}_{-0.43}$	0.84	34
GRB 121024A	2.298	4.53	0.52 ± 0.35	0	0.66	54
GRB 121027A	1.773	5.10	$1.14^{+0.26}_{-0.23}$	$1.10^{+0.56}_{-0.43}$	1.00	16
GRB 121128A	2.20	3.18	$0.92^{+0.45}_{-0.35}$	$0.49^{+2.29}_{-0.49}$	0.99	83
GRB 121201A	3.385	2.17	0.70 ± 0.11	0	0.99	21
GRB 121211A	1.023	2.62	$1.00^{+0.13}_{-0.12}$	$0.42^{+0.12}_{-0.10}$	0.79	39
GRB 121229A	2.0707	4.60	$1.08^{+0.85}_{-0.76}$	0	0.6	47

4.5   Results

After completing all of the above normalizations and corrections, I built a diagram containing all the GRBs normalized light curves of the sample (254 GRBs), which is displayed in Fig. 4.7.

Gendre et al., 2008a built a flux distribution for their sample at one day. The decision for using the flux at one day was made to avoid early afterglow data.
With the large sample, I used the flux distribution at one day. Surprisingly, the three groups were not apparent, as it can be seen in Fig. 4.8.
 This result was checked at various times during the afterglow, but the broad distribution always remained similar, see Fig. 4.9, which is in the line with the one obtained by the Melandri et al., 2014, surprisingly.
 Why something seen by BeppoSAX, XMM and Chandra, independently (i.e. the clustering was visible for each of these missions alone) would disappear with *Swift*? This question is the purpose of the next section.
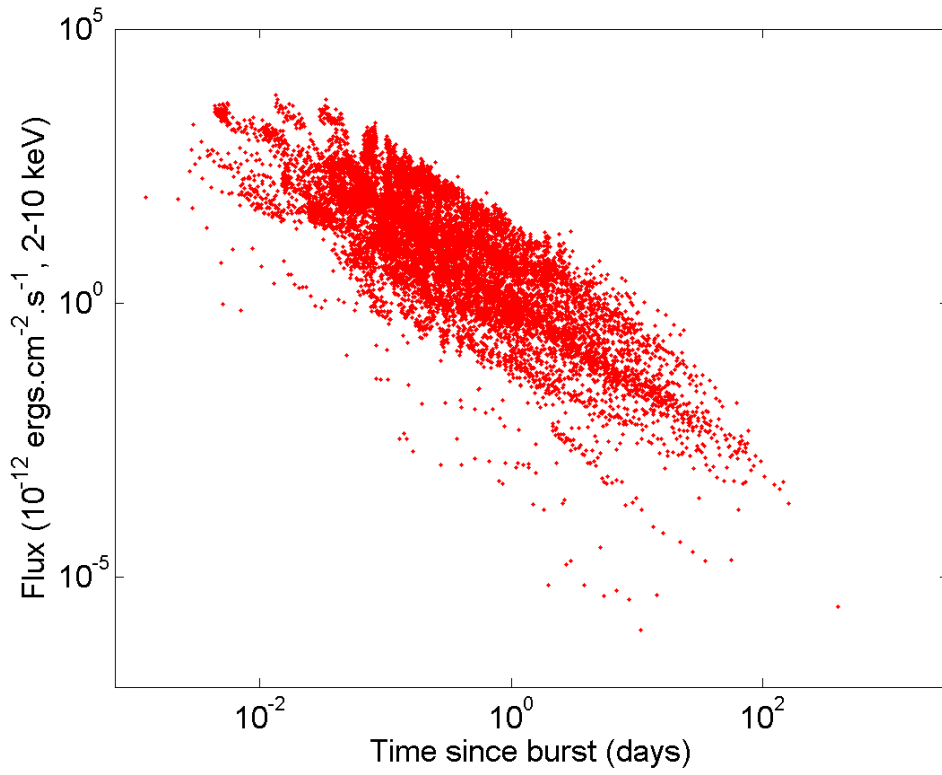
FIGURE 4.7: Light curve for 254 GRBs of our sample

4.6 Discussion

4.6.1 Flux distribution for different groups

We extended the flux distribution at one day. Fig. 4.8 into the Fig. 4.10 display the result of the new sample. This distribution allows us to check for the position of each group. In Fig. 4.10 we have shown the position of the double Gaussian fit as computed from the result described in the Gendre et al., 2008a. The colors of the plot correspond to: red color represents Gr. I, blue color represents Gr. II, green color represents Gr. III and cyan color represents the GRBs located between Gr. I and Gr. II, the same as in Gendre et al., 2008a.

We checked our results by using the pipeline of Raffaella Margutti (private communication) and we obtained consistent results.

The Fig. 4.8 and Fig. 4.10 illustrate the absence of three groups of X-ray afterglow light curves and moreover it demonstrates a scatter of the data. There are basically three explanations:

- Instrumental problems

- Data calibration problems

- Clustering does not exist
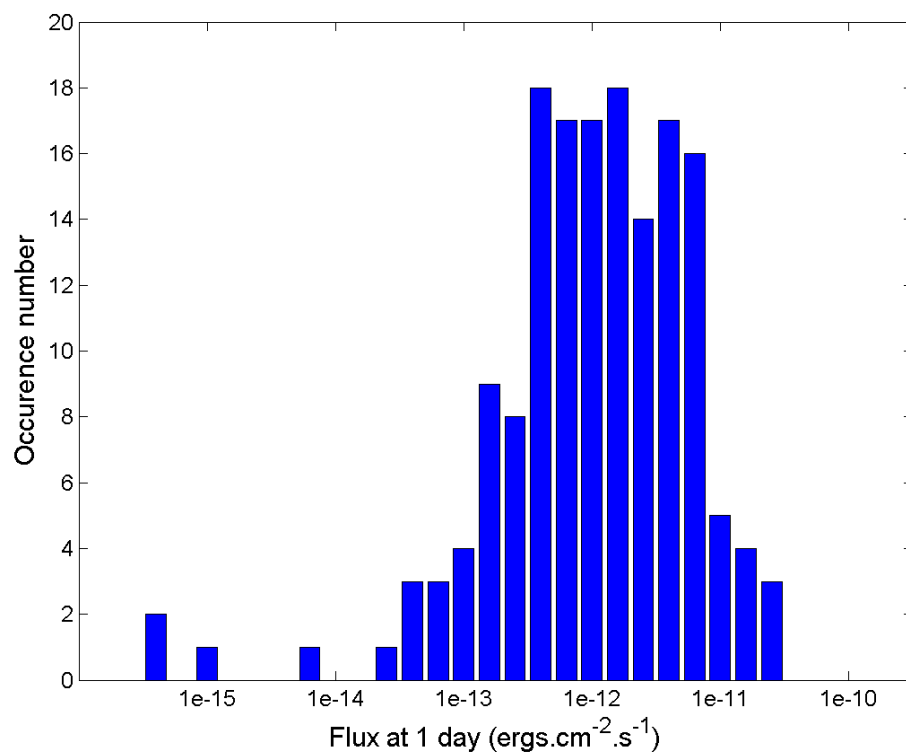
FIGURE 4.8: Flux distribution at one day for 254 GRBs
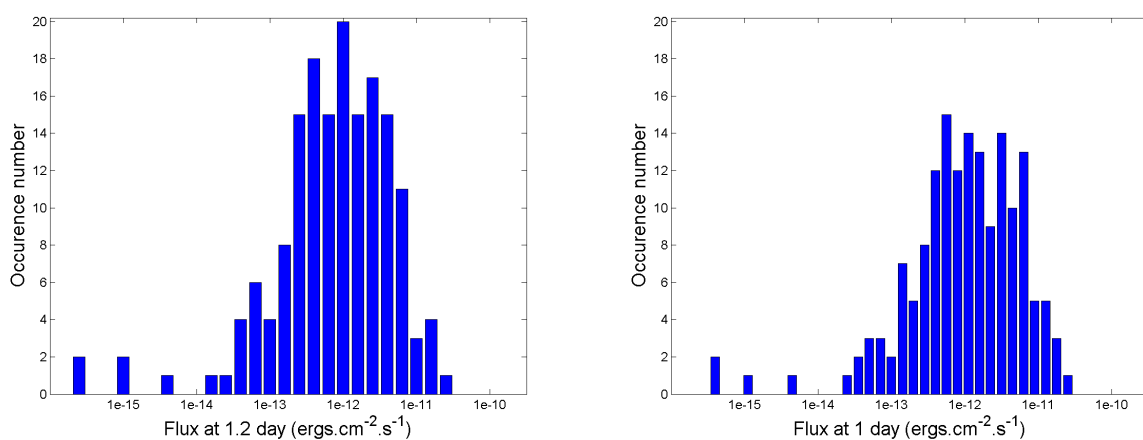
FIGURE 4.9: Flux distribution at 1.2 days for 254 GRBs (figure on the left) and flux distribution at one day for a smaller bin (figure on the right)
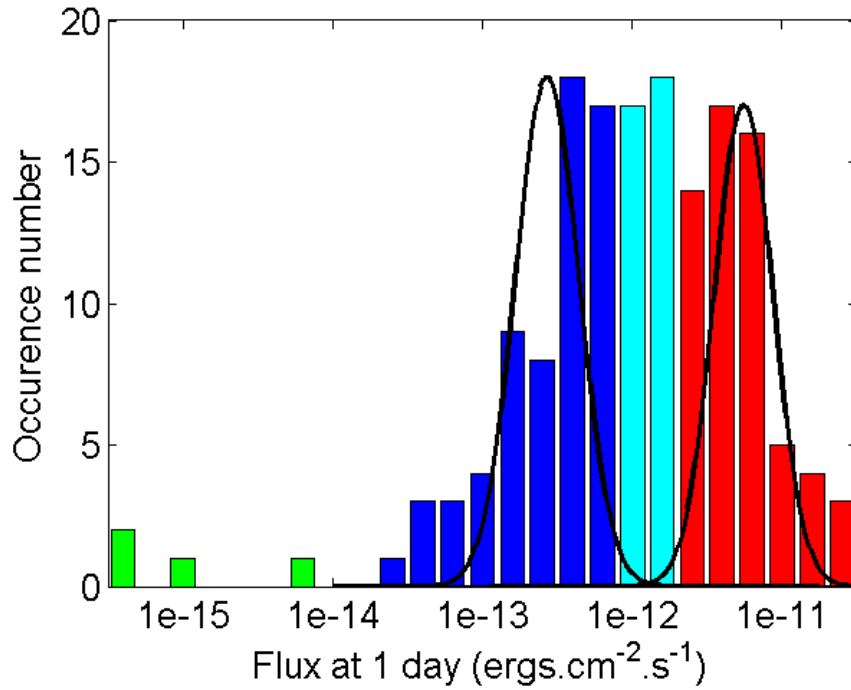
FIGURE 4.10: Flux distribution at 1 day after the burst. Red, blue, and green bars represent groups I, II, and III respectively. The cyan bars represent the GRBs located between Groups I and II. The black line shows the best-fit Gaussian distribution of Gendre et al., 2008a. Credit: Bardho et al., 2015

4.6.2 Instrumental problems

The fact that only the addition of *some* (not all) *Swift* bursts destruct the clustering made us wonder if it does not come from an instrumental problem. In this scenario, we assumed the existence of the clustering. From Fig. 4.10, we conclude that between the two existing groups (Gr. I and Gr. II), we have some GRBs, which probably should not be located there. There are 35 GRBs inside this middle group. This leads to the idea that this group of GRBs should be peculiar, or might have special properties different from the other GRBs of Gr. I and Gr. II.

The date of the observation is the first apparent feature. A quick examination, simply by eye sight, presents a lack of GRBs during several months. A further investigation, considered the monthly distribution of all the problematic GRBs, demonstrates some kind of periodicity (Fig. 4.11, left part), with less problems near the solstices, and a maximum of problematic events near the equinoxes. This is outlined when one compares with the same distribution, but for all bursts (presented in Fig. 4.11, right part), where there is absolutely no periodicity (one should note that we normalized each month by its duration, so February and January can be fairly compared).

The Kolmogorov - Smirnov test indicates a failure to reject the null hypothesis that the two samples are similarly distributed, at 5% significance level with an asymptotic p-value 0.48 and the cumulative distribution is shown in Fig. 4.12.

FIGURE 4.11: Left: Distribution of the month of detection for the 35 GRBs located between groups I and II. Right: Same distribution, but for our whole sample. Credit: Bardho et al., 2015

FIGURE 4.12: Cumulative distribution along the months for the 35 GRBs located between groups I and II (the blue line) and for the whole sample with 254 GRBs (the red line).

This distribution does not start from the zero value in the x-axis, since we do not have a year zero. Thus, the zero is considered the first month and obviously on the year 2005.

As we see from the cumulative distribution, the maximum difference between the two samples occurs during June and September. Therefore, this test is another indicator that during solstices and equinoxes, we might have some problems with the *Swift* observations. Whereas after mid October, we have the months during which the *Swift* observations seem to be linear and not problematic.

The first idea comes as a problem of Earth (or Sun) limb at that time, i.e. an increase of the background induced by the orbit, and maybe not well taken into account during the data reduction.

This is confirmed for the Earth limb angle, Fig. 4.13. In fact this value should be higher than 45 degrees, as explained the *Swift* User Guide (Capalbi et al., 2005). The Fig. 4.13 clearly

illustrates that this value is overcome (see the Fig. 4.13).
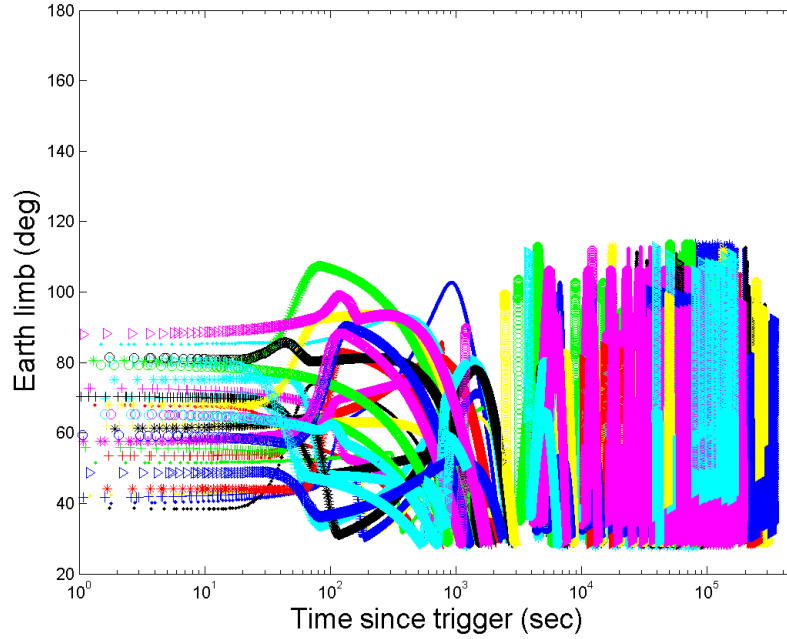
FIGURE 4.13: The plot of the Earth limb angle comparative to the pointing angle of the *Swift*. The plot shows the Earth limb only for 35 problematic GRBs. Each color/marker represents one GRB.

In this context, we conclude that this lack of GRBs during the months July-August and a peak in October, should be neither a real instrumental problem, nor a selection effect, but a data reduction problem. The mean value of the month distribution for the problematic GRBs is ≈ 3 GRBs per month.

Beyond the investigation of the monthly distribution, we inspect the year distribution for 35 GRBs which are problematic and for 232 GRBs, which are only the *Swift* sample, Fig. 4.14.
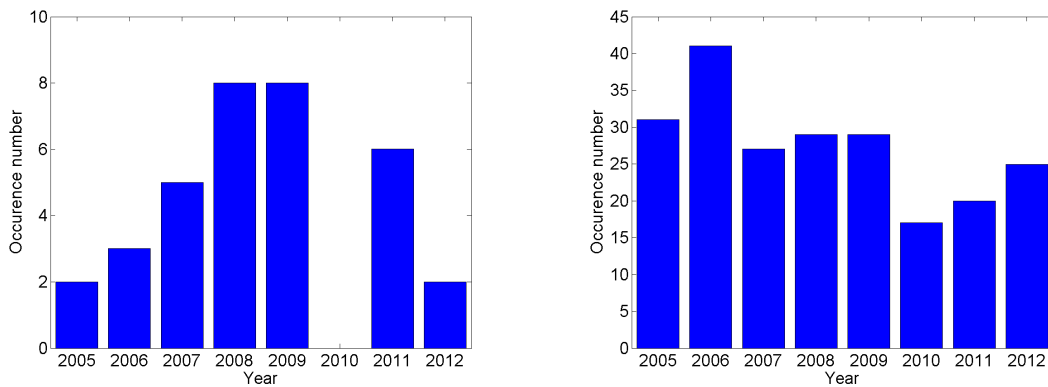
FIGURE 4.14: Distribution during years of detection for the 35 GRBs located between groups I and II (on the left) and for the whole *Swift* sample (on the right).

The Kolmogorov - Smirnov test indicates a failure to reject the null hypothesis at 5 % significance level with an asymptotic p-value 0.38 and the cumulative distribution is shown in Fig. 4.15.
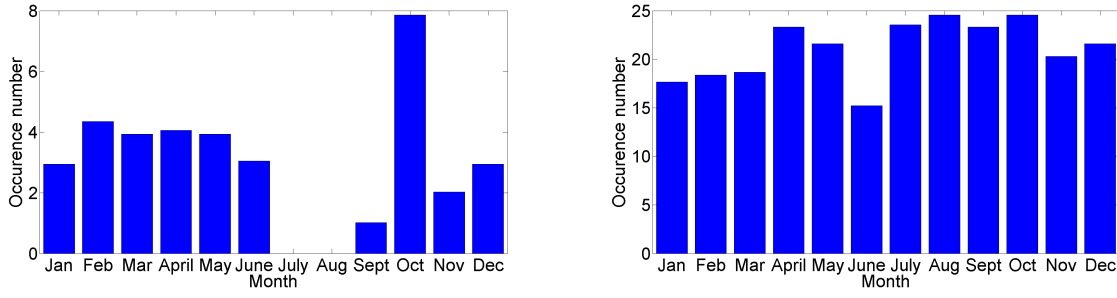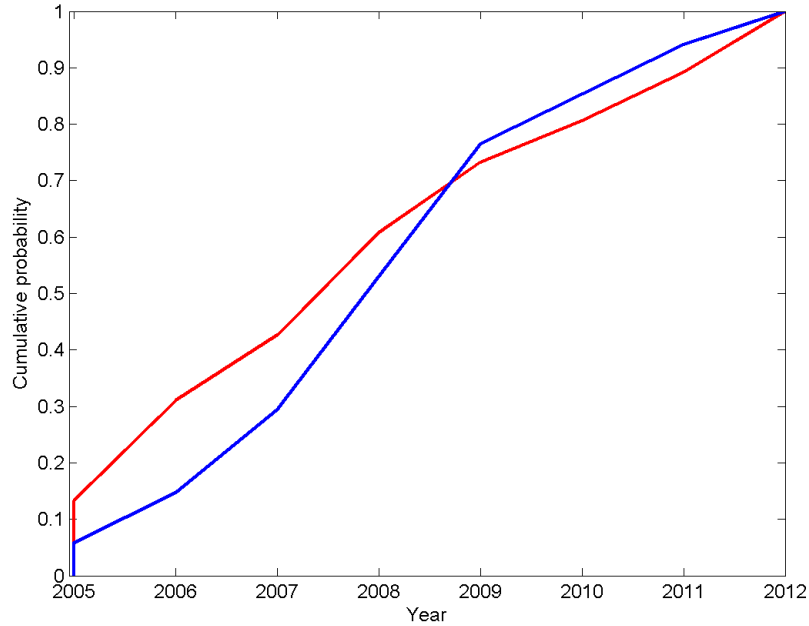

FIGURE 4.15: Cumulative distribution along the years for the 35 GRBs located between groups I and II (the blue line) and for the whole sample with 254 GRBs (the red line).

The same phenomenon happened for the year distribution as explained for the cumulative distribution along the months. We do not start our observation by the year zero, thus the cumulative distribution, cannot start from a zero value in the year axis.
On Fig. 4.15, the maximum difference between the two samples come along the years 2005-2007.

We examined the cumulative distribution along the day for 35 problematic GRBs and 254 GRBs of the whole sample (Fig. 4.16) and the Kolmogorov - Smirnov test indicates a failure to reject the null hypothesis at 5 % significance level with an asymptotic p-value 0.24, by comparing the bursts depending on the day of observation, elapsed from the first day of the year. This time the day starts at zero, as we count that the first day of the year is the day zero. The days along the leap years are normalized, thus we can worthily compare a non leap year to a leap year. This distribution shows again the same problem as the previous ones. Along the June-July period the differences between these plots are in maximum, meaning that the problematic events come during the summer solstice (North hemisphere) and fewer problems during the fall equinox.
All the above plots, linked with the cumulative distributions are done by using a standard normal deviation.

The spectral index distribution is another feature that we checked in order to examine the instrumental problems. We built the spectral index distribution of 35 problematic GRBs located between Gr. I and Gr. II and compared it with the whole sample composed by 254 GRBs. The same comparison is made, furthermore, by using the sample of Gendre et al., 2008a where we can clearly see the clustering. Moreover the comparison was made for their respective cumulative distribution, Fig. 4.17 and Fig. 4.18. In both cases the Kolmogorov - Smirnov test indicates
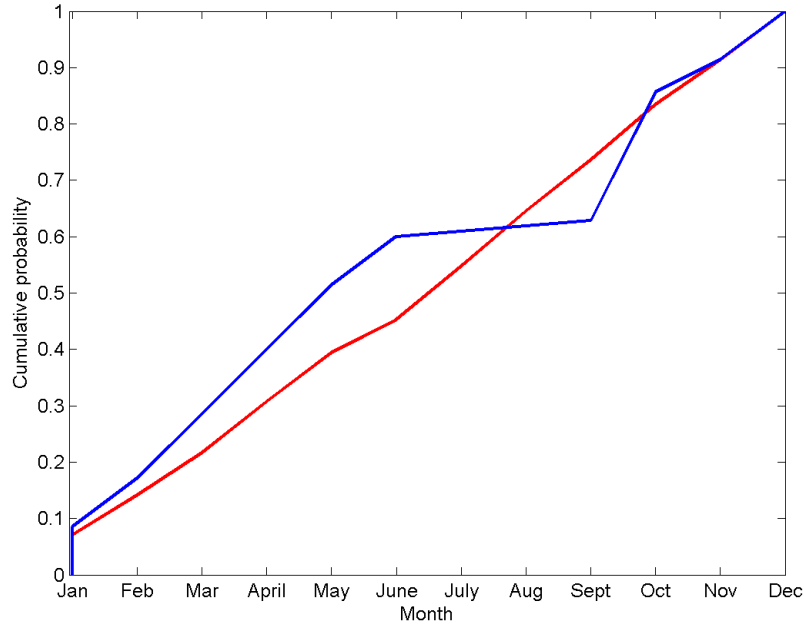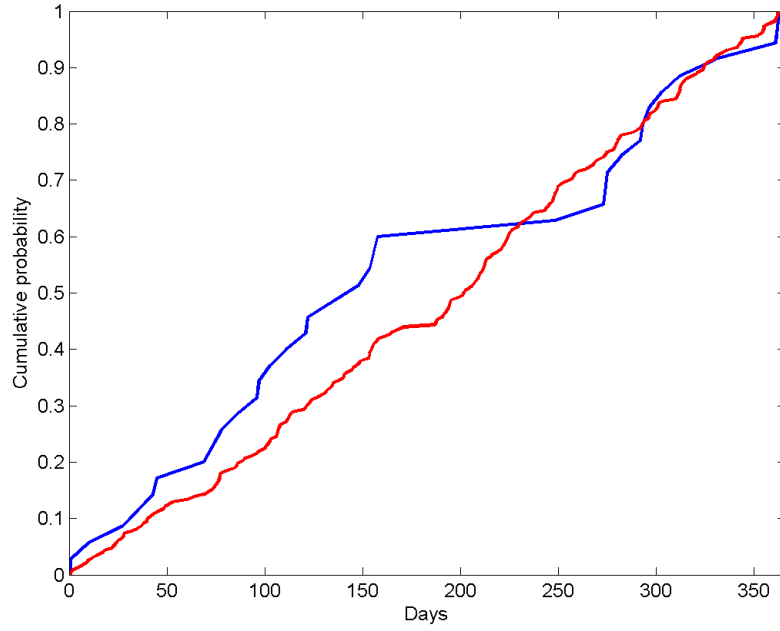
FIGURE 4.16: Cumulative distribution for the 35 GRBs located between groups I and II (the blue line) and for the whole sample with 254 GRBs (the red line).

a failure to reject the null hypothesis at 5 % significance level with an asymptotic p-value 0.77 and 0.55 for Fig. 4.17 and Fig. 4.18 respectively.
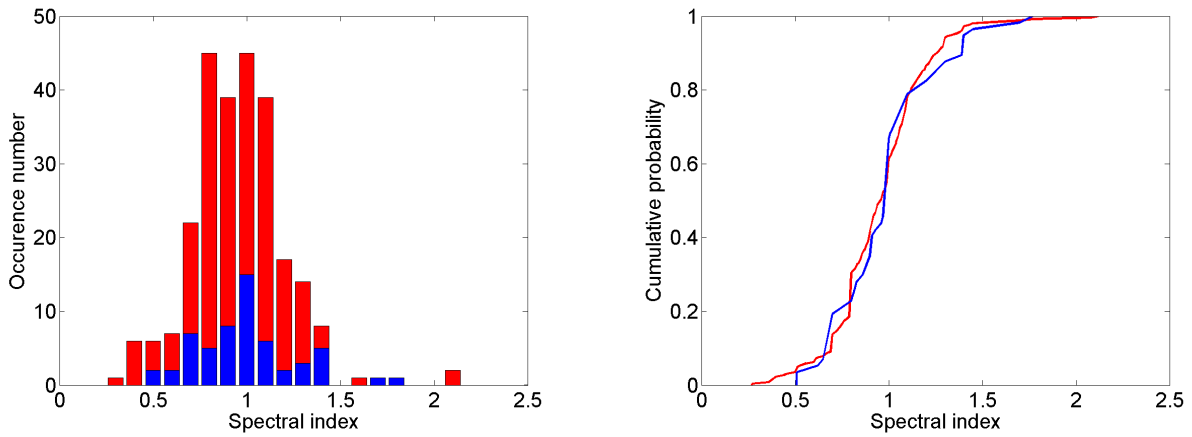
FIGURE 4.17: Spectral index distribution for the 254 GRBs (red bars) and for Gendre et al., 2008a sample (blue bars), (figure on the left). Cumulative distribution for each sample, the colors represent the same sample as in the figure on the left (figure on the right).

As we see from the Fig. 4.18, there is no clear difference between the 35 problematic GRBs and the GRBs where we can see the clustering from Gendre et al., 2008a. Moreover these groups seem identical to the whole sample of 254 GRBs.

The last examination was the flux distribution at one day for GRBs depending on their month, meaning that, I built a flux distribution for every month. This investigation does not lead to
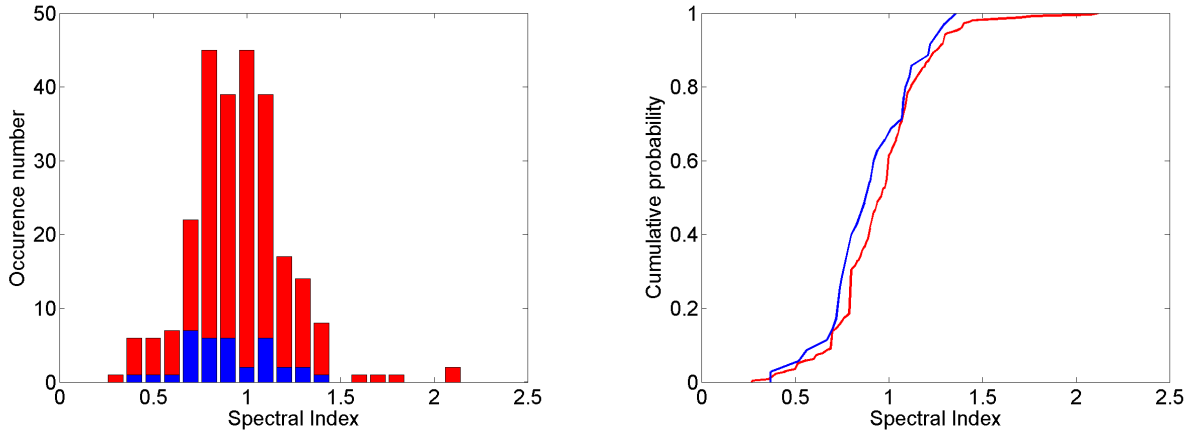
FIGURE 4.18: Spectral Index distribution for the 254 GRBs (red bars) and for 35 problematic GRBs located between groups I and II (blue bars), (figure on the left). Cumulative distribution for each sample, the colors represent the same sample as in the figure on the left (figure on the right).

further results related to the existence or non-existence of the X-ray clustering of afterglow light curves.

I would like to emphasize that the GRBs, which during the manual analysis were considered a theoretical model, do not play any role in the lack of the clustering. 3 out of 35 problematic GRBs are part of this theoretical model during analysis.

4.6.3 Data calibration problems

I faced various problems for several GRBs while performing spectral analysis for the whole sample. This made me think that the automatic analysis is not the best solution for a particular data analysis, which might influence the results of the study.

Spectral index comparison

I compared the spectral index of my manual analysis with the results from the *Swift*-XRT GRB spectrum repository (Evans et al., 2009, 2007). The comparison plot is displayed in Fig. 4.19. Clearly, in most of the cases, we are in close agreement. However, in about 11.2% of the cases, we found some discrepancies. We stress that this comparison is not straightforward, as we are not dealing with the exact same thing. The reasons for this difference come from the following conditions:

- **First**: The temporal range of spectral analysis is not identical in various cases. We are interested in the late afterglow of the GRBs, considering a specific time that depends on every GRB, whereas the *Swift*-XRT GRB spectrum repository proposed by default, a time averaged spectrum between T_1 and T_2 of the object observed, irrespectively of its emission phase. This comparison is performed by using the late time spectrum available in the *Swift*-XRT GRB spectrum repository.

- **Second**: We performed the spectral fitting by using an absorbed power law model (`wabs*zwabs*pow`): one absorption component fixed in our own galaxy and the other one let free to the redshift of the GRB, while the *Swift*-XRT GRB spectrum repository is using a different model with two small differences:

  1. For some GRBs, the spectrum repository webpage reports an unknown value for the redshift, and in that case the spectral fit can give inconsistent results

  2. *Swift*-XRT GRB spectrum repository uses `phabs` as an absorption model while we use `wabs`. The difference between these two absorption models is only related to the cross section model of the photoelectric absorption. `Phabs` is a photoelectric absorption model which is based on the cross-section from Morrison and McCammon, 1983, whereas the `wabs` is a photoelectric absorption which is based on the cross-section from Balucińska-Church and McCammon, 1992. In spite of this difference not much would change, considering that the atomic absorption cross sections were taken from Morrison and McCammon, 1983 in both studies. Thus, we do not expect a difference of more than 1 %.

- **Third**: The correction method of pile-up is very different and can lead to strong differences. We use the method explained at (Vaughan et al., 2006), while the limit for considering a pile-up region is 0.8 counts/sec, but the *Swift*-XRT GRB spectrum repository uses 0.6 counts/sec (Evans et al., 2009, 2007). This means that by considering 0.6 counts/sec as a limit of a pile-up source, we lose significant photons, which clearly affect the results. Furthermore, a low limit of pile-up has other consequences, such as: big error bars, distortion of PSF, and thus a wrong selection of the source region. The distortion of the PSF occurs due to the cut of PSF. Thus, it causes two different problems: 1. Energy distortion and 2. Spectral fitting problem.

- **Fourth**: Continuing with the previous item, a private communication with the team of the *Swift*-XRT GRB spectrum repository, allows us to understand that, in some cases, they are using a very small source region, which goes up to 5 pixels, which is an incorrect decision for choosing a region. Whereas for our analysis the smallest region was around 12-13 pixels.

- **Fifth**: The statistic used in both cases is different. We use the χ^2 statistic, while the *Swift*-XRT GRB spectrum repository uses the Cash statistic. χ^2 statistic operates with binned data and is a highly reliable statistic for an observation which has many photons. In the cases that the observation of a burst has fewer than 100 counts, we applied the Cash statistics which operates with unbinned data. The binning of data with fewer counts would smooth the fit and we may lose some information about the feature of the spectrum.

Thus, we did expect some differences, and found that about 90 % of compatibility is a good result. There are in any case 28 bursts with significant spectral discrepancies, which are not all in the group of 35 problematic events.

The manual and automatic analysis do not have any difference for the GRBs which I did analysis by using a theoretical model.
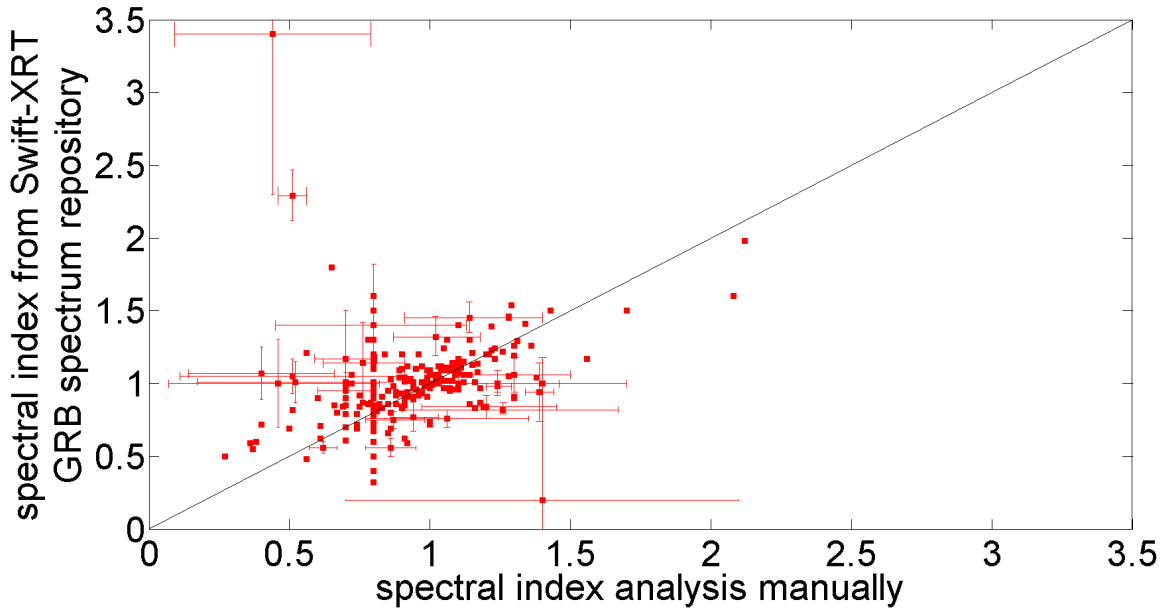
FIGURE 4.19: Comparison of the spectral indices from the manual analysis (x axis) and *Swift*-XRT GRB spectrum repository (y axis). The black line is the line of equality, where both results are equal. For clarity, we removed from the plot the error bars of GRBs which are compatible with equality. Credit: Bardho et al., 2015

ECF comparison

In addition, we examined the comparison of ECF between the manual and automatic analysis, Fig. 4.20.
ECF is a parameter which depends directly on the spectral fitting. The examination of the local minima is considerably higher than the automatic analysis while performing manual data analysis. This implies that automatic analysis does not provide accurate results for the conversion factor. This problem might influence the results of the study, moreover when the results are obtained for an earlier phase of the explosion, where the spectral evolution is highly significant.

The ECFs for the manual analysis are obtained as the ratio between Flux of the model of the burst and count rate, whereas the ECF for the *Swift*-XRT GRB repository is not presented online, thus we calculated it by using the HEASARC WebPIMMS's webpagehttp://heasarc.gsfc.nasa.gov/cgi-bin/Tools/w3pimms/w3pimms.pl.

As one can expect, there are differences in the ECF between manual and *Swift*-XRT GRB repository, meaning that flux to count rate conversion will be different and consequently, the position of GRBs in the flux distribution diagram will be different.

4.6.4 Clustering does not exist

The last question is: Is the clustering real?
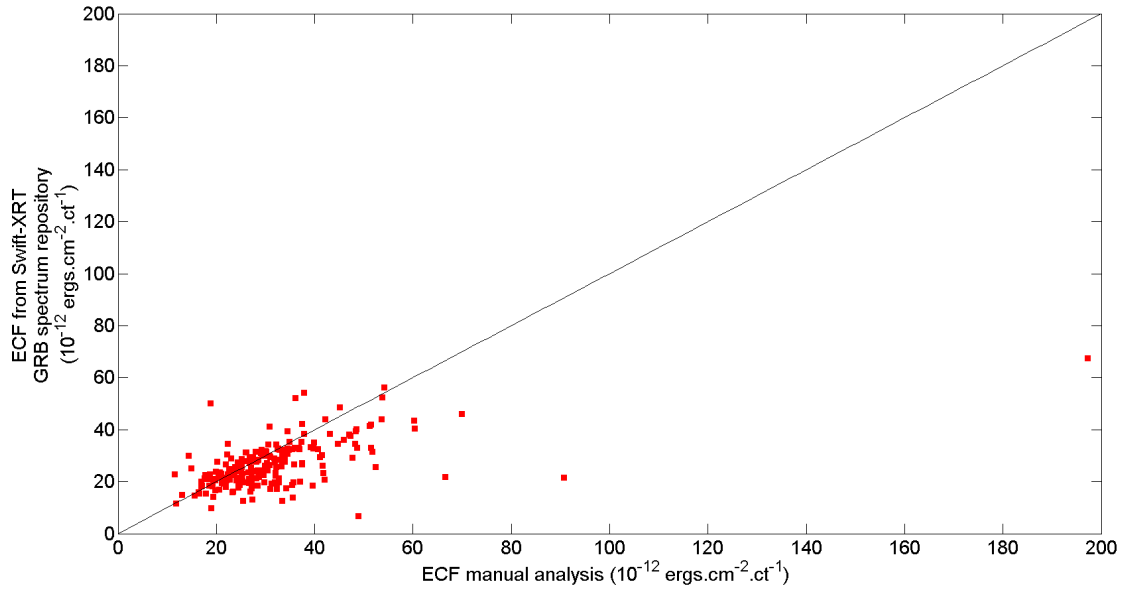
FIGURE 4.20: Comparison of ECF from the manual analysis (x axis) and *Swift*-XRT GRB spectrum repository (y axis). The black line is the line of equality, where both results are equal.

The obvious answer to this question would be a selection effect. In the pre-*Swift* era, the rarity of X-ray light curves implies to build a sample of events observed by BeppoSAX, XMM-Newton and Chandra. It is this mix that produces a (apparent) lack of events, then solved by *Swift*.

This may be the reason that many (see Melandri et al., 2014, one of the latest works) do not see this clustering in their work.
BAT6 sample (Melandri et al., 2014, Salvaterra et al., 2012) does not have the same criteria as our sample. This sample was chosen based in the optical properties, where the most important factor is that the long GRBs should be bright in the gamma ray band. The redshift measurement of the GRBs of this sample is completed only by 95 %.

Melandri et al., 2014 have checked the distribution of GRBs at 12 hours in the rest frame, meaning at one day in the observer frame at z = 1.

In spite of that, the examination of the number of GRBs inside my sample and the BAT6 sample, leads to a big difference. The BAT6 sample consists of 58 GRBs out of 254 GRBs in my sample. Thus, there are only 9 out of 35 problematic GRBs in BAT6 sample. Almost the same amount of GRBs is part of Gr. I and Gr. II. However, they are using the pipeline which could have problems. Their data being suspicious, any conclusion should be taken with caution.
Thus the comparison of both results is out of the scope of this study.

The last possibility of this scattered data should be a selection effect. This means that before the launch of *Swift* satellite, the possibility of observing X-ray afterglow was extremely low. The detection of X-ray afterglows after 2004 opened a New Era on the GRBs research, and made the astrophysics community recheck the previous results.
It is however very difficult to explain why BeppoSAX was seeing a gap between the two groups and not a standard "dim selection effect" removing dim sources. This simple constatation makes more obvious that something is wrong with *Swift* in some cases.

4.6.5 Amati relation

We examined the prompt properties of our sample. Lorenzo Amati provided for us the prompt emission results for GRBs observed by the Fermi satellite. We should mention that this sample does not contain all the GRBs that are in our sample. Both samples have 88 common GRBs, meaning that half of our sample is included. Accordingly, I put in the $E_P - E_{iso}$ plane the GRBs that are in both samples and separated them in each group shown in the Fig. 4.10. The $E_P - E_{iso}$ plane for our sample is illustrated in the Fig. 4.21.
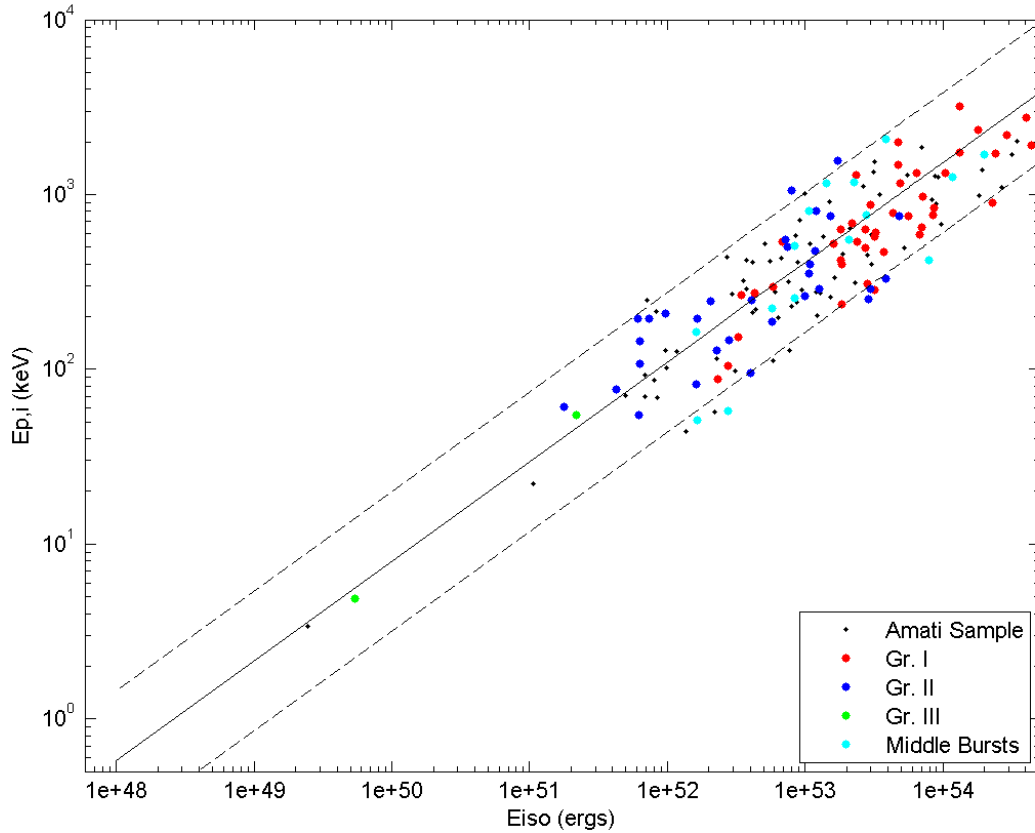
FIGURE 4.21: E_p-E_{iso} relation to our sample (see text for the details).

As we can clearly see our two groups are not clustered, even when checking their prompt properties.

This result demonstrated that clustering is not a feature of the prompt emission. Up to this time, none was capable of observing the clustering for the prompt emission, thus this is an acceptable and expected result.

Chapter 5

Conclusions and Perspectives

My research study relates to different correlations that exist in the GRBs data. Most of these correlations are related to the observational properties of the burst. This study is based on the problems that may come from data analysis. These problems are entirely linked with the process of data analysis which might be different for different studies.

A complete observational analysis and theoretical discussion for the peculiar GRB 141221A were performed in order to illustrate how the data reduction and analysis are done.
In the X-ray band this burst is similar to the ones previously observed. Whereas the optical shows a rising part, a pseudo-plateau, and various temporal breaks. Thus we give several explanations of these temporal breaks. The properties of GRB 141221A are rather unusual and difficult to explain within the standard model of GRBs.

A clustering in the X-ray afterglow light curves was observed before the launch of the *Swift* satellite. This result has been discussed due to the new results from the *Swift* satellite. I have constructed a sample of 254 X-ray afterglows of *Swift* GRBs in order to check the clustering of the afterglow light curves observed during the pre-*Swift* era and *Swift* era. We can clearly see that the clustering is no more apparent in the *Swift* era. However, this result motivates a broad study which leads to three different solutions: 1. Instrumental problems, 2. Data calibration problems, and 3. Clustering does not exist.

The starting point of the examination of the instrumental problems was the monthly distribution of 35 problematic GRBs located between Gr. I and Gr. II. This distribution illustrates some seasonal effects for GRBs during July-August and October. This result comes as a comparison of this distribution with the month distribution of the sample of 254 GRBs. The cumulative distribution for different days elapsed from the first day of the year and for different months illustrate this problem again.

The different statistical tests were applied in order to check for the seasonal effect of these bursts.

The spectral index distributions of the problematic sample with 35 GRBs located between Gr. I and Gr. II, the sample of Gendre et al., 2008a (the last sample where we could see the clustering of X-ray afterglow light curves) and the large sample demonstrate no clear differences between

these samples. This means that all these samples display an identical distribution of the spectral indexes. Thus we cannot pinpoint different groups inside the sample.

In all cases the cumulative distribution illustrates that the problematic months are July-August and October.

We have evidence that some problems might come because of the Earth limb angle on the pointing direction of the burst. Obviously the data should be excluded if this angle is smaller than 45 degree (Capalbi et al., 2005), which has not always been the case.

In order to understand these seasonal problems, one idea would be to investigate deeply on the 35 problematic bursts and to really understand if there are some observational problems during the solstices and equinoxes. This leads to the verification of different problems that might come from the position of the satellite, corresponding to the position of the Sun, Moon and Earth limb. This could indicate a problem of the background induced by the orbit. Furthermore the orbital parameters of the *Swift* satellite during the whole year would be an indication of the existence or non-existence of the problems.

An investigation of these 35 problematic GRBs in the optical bands would be another interesting study. This will highlight the problem (if they exist) for these bursts. Moreover, an investigation of the distribution of their optical light curves, compared to overall distribution would bring some information related to these problematic bursts.

This investigation would be an interesting check of the different properties that might have influences on the instrument during the observation process.

We performed some additional statistical tests during this investigation. Comparing my spectral analysis with the one of the *Swift*-XRT GRB spectrum repository, I found that we are in agreement with the majority of cases. However, I found some discrepancies for 11.2% of bursts. Some discrepancies can be easily explained by a difference of time range (for the extraction of the spectrum) or model, while others are more difficult to explain and understand.

The Energy Correction Factor (ECF) is one piece of evidence which may be problematic in the automatic analysis. ECF is a parameter which directly depends on the flux of the burst model. The examination of the local minima is considerably deeper than the automatic analysis when performing manual data analysis. This implies that the automatic analysis does not provide accurate results with regards to the conversion factor. This is a factor that is directly related to shift of the Boer & Gendre relation in the *Swift* era.

I conclude that a real observational research is based on the reliability of data analysis. The performance of the data analysis should have a dual check related to the information that the burst provides and the goals of the study. As we show in Chapter 4, a small difference on the parameters of the data analysis might significantly influence the results of the study. This means that a manual analysis of a certain study is never time consuming, in the cases that particular analysis required for special research might not be performed from the *Swift*-XRT GRB spectrum repository. The problematic issues include a small change of the time, a region selection, a redshift measurement, an absorption model, a statistical model of the fit, a flux correction and much more beyond this study.

The existing pipelines are one good option for not consuming time of redoing data analysis. The difference comes when the purpose of the study goes beyond the information that an automatic analysis could provide.

The investigation of the clustering of the X-ray afterglow light curves opened a new study. The existence of the clustering before the *Swift* Era may be considered as a hint of this clustering. The following work of this study should be a simulation process, which randomly chooses a certain number of GRBs and builds the flux distribution at one day, to find the probability that this clustering exists or not.
In this case, this simulation process notifies a difference between manual and automatic analysis which means that the automatic process should be redone from the beginning, trying to improve it for different purposes.

The last message that I would like to stress is that these problems which come due to the automatic pipeline might affect every publication so far. Even if 90 % of the results are compatible, still the 10 % should be doubtful. This is one of the main reasons why we see differences on the results between the pre and the post *Swift* era.

Bibliography

L. Amati. Intrinsic spectra and energetics of cosmological Gamma-Ray Bursts. *Chinese Journal of Astronomy and Astropphysics Supplement*, 3:455–460, 2003.

L. Amati. The $E_{p,i}$-E_{iso} correlation in gamma-ray bursts: updated observational status, reanalysis and main implications. *MNRS*, 372:233–245, 2006.

L. Amati, F. Frontera, M. Tavani, et al. Instrinsic spectra and energetics of BeppoSAX Gamma-Ray Bursts with known redshifts. *Astronomy and Astrophysics*, 390:81–89, May 2002.

K. Arnaud, B. Dorman, and C. Gordon. *An X-ray Spectral Fitting Package*, version 12.9.0 edition, 2015.

K. A. Arnaud. XSPEC: The First Ten Years. *Astronomical Data Analysis Software and Systems V, A.S.P. Conference Series, G. H. Jacoby and J. Barnes, eds*, 101:17–20, 1996.

J.-L. Atteia. A simple empirical redshift indicator for gamma-ray bursts. *Astronomy and Astrophysics*, 407:L1–L4, 2003.

J. L. Atteia, C. Barat, K. Hurley, et al. A second catalog of gamma-ray bursts: 1978-1980 localizations from the interplanetary network. *The Astrophysical Journal Supplement Series*, 64:305–382, May 1987.

J. Ballet. Pile-up on the X-ray CCD instruments. *Astronomy and Astrophysics Supplement Series*, 135:371–381, March 1999.

M. Balucińska-Church and D. McCammon. Photoelectric absorption cross sections with variable abudances. *The Astrophysical Journal*, 400:699–700, December 1992.

D. Band, J. Matteson, L. Ford, et al. BATSE observations pf gamma-ray burst spectra. I. spectral diversity. *The Astrophysical Journal*, 413:281–292, August 1993.

O. Bardho, M. Boër, and B. Gendre. 10 Years of XRT light curves: a general view of the X-ray afterglow. *Proceedings of Science*, 062, 2015.

O. Bardho, B. Gendre, A. Rossi, et al. GRB 141221A: gone as the wind. *Monthly Notices of the Royal Astronomical Society*, 459:508–516, March 2016.

D. S. Barthelmy, M. L. Barbier, R. J. Cummings, et al. The Burst Alert Telescope (BAT) on the *Swift* MIDEX mission. *Space Science Reviews*, 120:143–164, October 2005.

A. P. Beardmore, P. A. Evans, M. R Goad, et al. *GCN Circular*, #17211, 2014.

E. Berger. Short-Duration Gamma-Ray Bursts. *arXiv:astro-ph/1311.2603v1*, November 2013.

E. Bissaldi, A. von Kienlin, G. Lichti, et al. Ground-based calibration and characterization of the Fermi gamma-ray burst monitor detectors. *Experimental Astronomy*, 24:47–88, 2009.

R. D. Blandford and C. F. McKee. Fluid dynamics of relativistic blast waves. *Physics of Fluids*, 19:1130–1138, 1976.

J. S. Bloom, S. G. Djorgovski, S. R. Kulkarni, et al. The host galaxy of GRB 970508. *The Astrophysical Journal*, 507:L25–L28, November 1998.

J. S. Bloom, D. A. Frail, and R. Sari. The prompt energy release of gamma-ray bursts using a cosmological *k*-correction. *The astrophysical Journal*, 121:2879–2888, June 2001.

G. Boella, R. C. Butler, G. C. Perola, et al. BeppoSAX, the wide band mission for X-ray astronomy. *Astronomy and Astrophysics Supplement Series*, 122:299–307, 1997.

M. Boër and B. Gendre. Evidences for two Gamma-Ray Burst afterglow emission regimes. *Astronomy and Astrophysics*, 361:L21–L24, August 2000.

M. Boër, A. Klotz, J.-L. Atteia, et al. The Gamma-Ray Burst Hunt at La Silla the TAROT-S Very Fast Moving Telescope. *The Messenger*, 113:45–48, September 2003.

M. S. Briggs, W. S. Paciesas, G. N. Pendleton, et al. BATSE observations of the large-scale isotropy of gamma-ray bursts. *The Astrophysical Journal*, 459:40–63, March 1996.

M. S. Briggs, D. L. Band, R. M. Kippen, et al. Observations of GRB 990123 by the COMPTON Gamma Ray Observatory. *The Astrophysical Journal*, 524:82–91, October 1999.

T. Brown, W. E. Rosing, N. Baliber, et al. Surveys, Temporal Variability and the Las cumbres Oservatory Global Telescope. *American Astronomical Society Meeting*, 39:173, May 2007.

N. D. Burrows, E. J. Hill, A. J. Nousek, et al. The *Swift* X-Ray Telescope. *arXiv:astro-ph/0508071v1*, August 2005.

N. R. Butler. On the early-time X-ray spectra of *Swift* afterglows. I. Evidence for anomalous soft X-ray emission. *The Astrophysical Journal*, 656:1001–1018, February 2007.

M. Capalbi, M. Perri, B. Saija, et al. *The SWIFT XRT Data Reduction Guide*, April 2005.

W. Cash. Parameter estimation in astronomy through application of the likelihood ratio. *The Astronomical Journal*, 228:939–947, March 1979.

G. Cavallo and M. J. Rees. A qualitative study of cosmic fireballs and γ-ray bursts. *MNRS*, 183:359–365, 1978.

R. A. Chevalier and Zh. Y. Li. Gamma-ray burst environments and progenitors. *The Astrophysical Journal*, 520:L29–L32, July 1999.

R. A. Chevalier and Zh-Y. Li. Wind interaction models for gamma-ray burst afterglows: the case for two types of progenitors. *The Astrophysical Journal*, 536:195–212, June 2000.

R. A. Chevalier, Zh. Y. Li, and C. Fransson. The diversity of gamma-ray burst afterglows and the surroundings of massive stars. *The Astrophysical Journal*, 606:369–380, May 2004.

G. Chincarini, F. Zerbi, A. Antonelli, et al. The last born at La Silla: REM, The Rapid Eye Mount. *The Messenger*, 113:40–44, September 2003.

E. Costa, M. Feroci, L. Piro, et al. GRB 970228. *International Astronomical Union*, 6576:1, March 1997a.

E. Costa, F. Frontera, J. Heise, et al. Discovery of an X-ray afterglow associated with the γ-ray burst on 28 February 1997. *Nature*, 387:783–785, June 1997b.

E. Costa, F. Frontera, D. D. Fiume, et al. The gamma-ray bursts monitor ondoard SAX. *Advances in Space Research*, 22:1129–1132, 1998.

S. Covino. *GCN Circular*, #17208, 2014.

S. Covino, A. Melandri, R. Salvaterra, et al. Dust extinctions for an unbiased sample of gamma-ray burst afterglows. *Monthly Notices of the Royal Astronomical Society*, 432:1231–1244, June 2013.

M. G. Dainotti, V. F. Cardone, and S. Capozziello. A time–luminosity correlation for γ-ray bursts in the X-rays. *MNRS*, 391:L79–L83, 2009.

M. G. Dainotti, R. Willingale, S. Capozziello, et al. Discovery of a tight correlation for gamma-ray burst afterglows with 'canonical' light curves. *The Astrophysical Journal Letters*, 722: L215–L219, October 2010.

M. G. Dainotti, V. Petrosian ans J. Singal, et al. Determination of the intrinsic luminosity time correlation in the X-ray afterglows of gamma-ray bursts. *The Astrophysical Journal*, 774: 157–166, September 2013.

H. Dereli. *Study of a Population of Gamma-ray Bursts with Low-Luminosity Afterglows*. PhD thesis, European Community Erasmus Mundus Joint Doctorate; International Relativistic Astrophysics Ph.D. Program, 2015.

H. Dereli, M. Boër, B. Gendre, et al. Properties of low luminosity Gamma-ray Bursts. *arXiv:astro-ph*, 1506.05521, June 2015.

J.-P. Dezalay, C. Barat, R. Talon, et al. Short cosmic events - a subset of classical grbs? *American Institute of Physics Conference Series*, 265:304–309, 1992.

P. A. Evans, A. P. Beardmore, K. L. Page, et al. Methods and results of an automatic analysis of a complete sample of *Swift*-XRT observations of GRBs. *MNRS*, 397:1177–1201, 2009.

P.A. Evans, A.P. Beardmore, K.L. Page, et al. An online repository of *Swift*/XRT light curves of GRBs. *Astronomy and Astrophysics*, 469:379–385, May 2007.

D. A. Frail, S. R. Kulkarni, L. Nicastro, et al. The radio afterglow from the γ-ray burst of 8 May 1997. *Nature*, 389:261–263, September 1997.

F. Frontera, E. Costa, D. D. Fiume, et al. The high energy instrument PDS on-board the BeppoSAX X-ray astronomy satellite. *Astronomy and Astrophysics Supplement Series*, 122: 357–369, 1997.

Ch. L. Fryer, S. E. Woosley, and D. H. Hartmann. Formation rates of black hole accration disk gamma-ray bursts. *The Astrophysical Journal*, 526:152–177, November 1999.

Ch. L. Fryer, A. L. Hungerford, and P. A. Young. Light-curve calculations of supernovae from fallback gamma-ray bursts. *The Astrophysical Journaal*, 662:L55–L58, June 2007.

M. Fukugita, K. Shimasaku, and T. Ichikawa. Galaxy Colors in Various Photometric Band Systems. *Publications of the Astronomical Society of the pacific*, 107:945–958, October 1995.

N. Gehrels, G. Chincarini, P. Giommi, et al. The *Swift* Gamma-Ray Burst mission. *The Astrophysical Journal*, 611:1005–1020, August 2004.

N. Gehrels, J. P. Norris, S. D. Barthelmy, et al. A new γ-ray burst classification scheme from GRB 060614. *Nature*, 444:1044–1046, December 2006.

B. Gendre and M. Boër. Decay properties of the X-ray afterglows of gamma-ray bursts. *Astronomy and Astrophysics*, 430:465–470, 2005.

B. Gendre, L. Piro, and M. De Pasquale. The XMM-Newton observation of GRB 040106: Evidence for an afterglow in a wind environment. *Astronomy and Astrophysics*, 424:L27–L30, 2004.

B. Gendre, A. Corsi, and L. Piro. X-ray continuum properties of grb afterglows observed by XMM-Newton and Chandra. *Astronomy and Astrophysics*, 455:803–812, 2006 2006.

B. Gendre, A. Galli, and M. Boër. X-ray afterglow light curves: toward a standard candle? *The Astrophysical Journal*, 683:620–629, August 2008a.

B. Gendre, S. Pelisson, M. Boër, et al. Gamma-ray burst afterglows: luminosity clustering at infrared wavelengths? *Astronomy and Astrophysics*, 492:L1–L4, 2008b.

B. Gendre, J. L. Atteia, and M. Boër. GRB 110205A: Anatomy of a long gamma ray burst. *The Astrophysical Journal*, 748:59–70, March 2012.

G. Ghirlanda, G. Ghisellini, C. Firmani, et al. The peak luminosity-peak energy correlation in gamma-ray bursts. *MNRS*, 360:L45–L49, 2005.

A. Gomboc. Unveiling the Sectrets of Gamma Ray Bursts. *arXiv:astro-ph/1206.3127*, 2012.

J. Goodman. Are gamma-ray bursts optically thick? *The Astrophysical Journal*, 308:L47–L50, September 1986.

J. Granot and R. Sari. The shape of spectral breaks in gamma-ray burst afterglows. *The Astrophysical Journal*, 568:820–829, April 2002.

J. Greiner, W. Bornemann, C. Clemens, et al. GROND-a 7-Channel Imager. *The Publications of the Astronomical Society of the Pacific*, 120:405–424, April 2008.

J. Greiner, T. Krühler, S. Klose, et al. The nature of "dark" gamma-ray bursts. *Astronomy and Astrophysics*, 526:A30–A39, 2011.

P. J. Groot, T. J. Galma, J. van Paradijs, et al. GRB 970228. *International Astronomical Union*, 6584:1, March 1997.

P. J. Groot, T. J. Galama, J. van Paradijs, et al. A search for optical afterglow from GRB 970828. *The strophysical Journal*, 493:L27–L30, January 1998.

C. Guidorzi, S. Dichiara, D. Kopac, et al. *GCN Circular*, #17209, 2014.

J. E. Hill, D. N. Burrows, J. A. Nousek, et al. Readout Mode and Automated Operation of the *Swift* X-Ray Telescope. *Proc. of SPIE*, 5165:217–231, 2004.

Ph. J. Humphrey, W. Liu, and D. A. Buote. chi^2 and poissonian data: biases even in the high-count regime and how to avoid them. *The Astrophysical Journal*, 693:822–829, March 2009.

R. Jager, W. A. Mels, A. C. Brinkman, et al. The Wide Field Cameras onboard the BeppoSAX X-ray Astronomy Satellite. *Astronomy and Astrophysics Supplement Series*, 125:557–572, 1997.

P. Jakobsson, J. Hjorth, J. P. U. Fynbo, et al. *Swift* identification of dark gamma-ray bursts. *The Astrophysical Journal*, 617:L21–L24, December 2004.

P. M. W. Kalberla, W. B. Burton, D. Hartmann, et al. The Leiden/Argentine/Bonn (LAB) Survey of Galactic HI. Final data release of the combined (LDS) and (IAR) surveys with improved stray-radiation corrections. *Astronomy and Astrophysics*, 440:775–782, 2005.

D. A. Kann, S. Klose, and A. Zrh. Signatures of extragalactic dust in pre-*Swift* GRB afterglows. *The Astrophysical Journal*, 641:993–1009, April 2006.

D. A. Kann, S. Klose, B. Zhang, et al. The afterglows of *Swift*-era gamma-ray bursts. I. Comparing pre-*Swift* and *Swift*-era long/soft (type II) GRB optical afterglows. *The Astrophysical Journal*, 720:1513–1558, September 2010.

R. W. Klebesadel, I. B. Strong, and R. A. Olson. Observations of gamma-ray bursts of cosmic origin. *The Astrophysical Journal*, 182:L85–L88, June 1973.

A. Klotz, F. Vachier, and M. Boër. TAROT: Robotic observatories for gamma-ray bursts and other sources. *Astronomische Nachrichten*, 329:275–277, March 2008.

A. Klotz, D. Turpin, M. Boer, et al. *GCN Circular*, #17227, 2014.

S. Kobayashi, B. Zhang, P. Mészáros, et al. Inverse Compton X-ray Flare from GRB Reverse Shock. *arXiv:astro-ph*, 0506157, October 2006.

C. Kouveliotou, S. E. Woosley, S. K. Patel, et al. *Chandra* observations of the X-ray environs of SN 1998bw/GRB 980425. *The Astrophysical Journal*, 608:872–882, June 2004.

Ch. Kouveliotou, Ch. A. Meegan, G. J. Fishman, et al. Identification of two classes of gamma-ray bursts. *The Astrophysical Journal*, 413:L101–L104, August 1993.

H. A. Krimm, S. T. Holland, R. H. D. Corbet, et al. The *Swift*/BAT hard X-ray transient monitor. *The Astrophysical Journal Supplement Series*, 209:14–47, November 2013.

T. Krühler, A. Küpcü Yoldaş, J. Greiner, et al. The 2175 Å dust feature in gamma-ray burst afterglow at redshift 2.45. *The Astrophysical Journal*, 685:376–383, September 2008.

T. Krühler, J. Greiner, P. Schady, et al. The SEDs and host galaxies of the dustiest GRB afterglows. *Astronomy and Astrophysics*, 534:A108–A124, 2011.

P. Kumar and T. Piran. Energetics and luminosity function of gamma-ray bursts. *The Astrophysical Journal*, 535:152–157, May 2000.

D. Q. Lamb and D. E. Reichart. Gamma-ray bursts as a probe of the very high redshift universe. *The Astrophysical Journal*, 536:1–18, June 2000.

D. Q. Lamb, T. Q. Donaghy, and C. Graziani. A unified jet model of X-ray flashes and X-ray bursts. *New Astronomy Reviews*, 48:459–466, 2004.

D. Q. Lamb, T. Q. Donaghy, and C. Graziani. A unified jet model of X-ray flashes, X-Ray-Rich gamma-ray bursts and gamma-ray bursts. I power-law-shaped universal and top-hat-shaped variable opening angle jet models. *The Astrophysical Journal*, 620:355–378, February 2005.

M. Lampton, B. Morgan, and S. Bowyer. Parameter estimation in x-ray astronomy. *The Astrophysical Journal*, 208:177–190, August 1976.

E. Liang and B. Zhang. Identification of two categories of optically bright gamma-ray bursts. *The Astrophysical Journal*, 638:L67–L70, February 2006.

A. I. MacFadyen, S. E. Woosley, and A. Heger. Supernovae, jets, and collapsars. *The Astrophysical Journal*, 550:410–425, March 2001.

R. Margutti. *Toward new insights on the gamma ray burst physics: from X-ray spectroscopy to the identification of the characteristic time scales.* PhD thesis, Universita' Degli Studi Milano - Bicocca, Scuola di dottorato in scienze, 2008–2009.

F. E. Marshall and E. Sonbas. *GCN Circular*, #17219, 2014.

A. Maselli, A. Melandri, B. Sbarufatti, et al. *GCN Circular*, #17214, 2014.

C. A. Meegan, G. J. Fishman, R. B. Wilson, et al. Spatial distribution of γ-ray bursts observed by BATSE. *Nature*, 355:143–145, January 1992.

Ch. Meegan, G. Lichti, P. N. Bhat, et al. The *Fermi* Gamma-ray Burst Monitor. *The Astrophysical Journal*, 702:791–804, September 2009.

A. Melandri, S. Covino, and D. Rogantini. Optical and X-ray rest-frame light curves of the bat6 sample. *Astronomy and Astrophysics*, 565:A72–A82, 2014.

P. Mészáros. Gamma-ray bursts. *Reports on Progress in physics*, 69:2259–2321, 2006.

P. Mészáros and M. J. Rees. Optical and long-wavelength afterglow from gamma-ray bursts. *The Astrophysical Journal*, 476:232–237, February 1997.

P. Mészáros and M. J. Rees. Collapsar jets, bubbles and Fe lines. *The Astrophysical Journal*, 556:L37–L40, July 2001.

R. Morrison and D. McCammon. Interstellar photoelectric absorption across sections, 0.03–10 kev. *The Astrophysical Journal*, 270:119–122, July 1983.

M. Nardini, G. Ghisellini, G. Ghirlanda, et al. Clustering of the optical-afterglow luminosities of long gamma-ray bursts. *Astronomy and Astrophysics*, 451:821–833, 2006.

J. A. Nousek, C. Kouveliotou, D. Grupe, et al. Evidence for a canonical gamma-ray bursts afterglow light curve in the *Swift* XRT data. *The Astrophysical Journal*, 642:389–400, May 2006.

Y. Ono, T. Yoshii, Y. Saito, et al. *GCN Circular*, #17222, 2014.

B. Paczyński. Gamma-ray bursts at cosmological distances. *The Astrophysical Journal*, 308: L43–L46, September 1986.

A. Panaitescu and P. Kumar. Analytic light curves of gamma-ray burst afterglows: Homogeneous versus wind external media. *The Astrophysical Journal*, 543:66–76, November 2000a.

A. Panaitescu and P. Kumar. Analytic light curves of gamma-ray burst afterglows: homogeneous versus wind external media. *The Astrophysical Journal*, 543:66–76, November 2000b.

U. P. Pen. Analytical fit to the luminosity distance for flat cosmologies with a cosmological constant. *The Astrophysical Journal Supplement Series*, 120:49–50, January 1999.

D. A. Perley, Y. Cao, and S. B. Cenko. *GCN Circular*, #17228, 2014.

L. Piro, E. Troja, B. Gendre, et al. A hot cocoon in the ultralong GRB 130925A: Hints of a popIII-like progenitor in a low-density wind environment. *The Astrophysical Journal Letters*, 790:L15–L19, August 2014.

E. Ramirez-Ruiz. Identifying young gamma-ray burst fossils. *Monthly Notices of the Royal Astronomical Society*, 349:L38–L42, 2004.

E. Ramirez-Ruiz, A. Merloni, and M. J. Rees. Quiescent times in gamma-ray bursts - II. Dormant periods in the central engine? *Monthly Notices of the Royal Astronomical Society*, 324:1147–1158, 2001.

E. Ramirez-Ruiz, A. Celotti, and M. J. Rees. Events in the life of a cocoon surrounding a light, collapsar jet. *MNRS*, 337:1349–1356, 2002.

M. J. Rees and P. Mészáros. Relativistic fireballs: energy conversion and time-scales. *MNRS*, 258:41–43, 1992.

M. J. Rees and P. Mészáros. Unsteady outflow models for cosmological gamma-ray bursts. *The Astrophysical Journal*, 430:L93–L96, August 1994.

M. J. Rees and P. Mészáros. Refreshed shocks and afterglow longevity in gamma-ray bursts. *The Astrophysical Journal*, 496:L1–L4, March 1998.

M. J. Rees and P. Mészáros. Fe Kα emission from a decaying magnetar model of gamma-ray bursts. *The Astrophysical Journal*, 545:L73–L75, December 2000.

D. Reichart, M. Nysewander, J. Moran, et al. PROMPT: Panchromatic Robotic Optical Monitoring and Polarimetry Telescopes. *Il Nuovo Cimento C*, 28:767–771, July 2005.

J. E. Rhoads. How to tell a jet from a balloon: A proposed test for a beaming in gamma-ray bursts. *The Astrophysical Journal*, 487:L1–L4, September 1997.

J. E. Rhoads. The dynamics and light curves of beamed gamma-ray burst afterglows. *The Astrophysical Journal*, 525:737–749, November 1999.

P. Romano, S. Campana, G. Chincarini, et al. Panchromatic study of GRB 060124: from precursor of afterglow. *Astronomy and Astrophysics*, 456:917–927, September 2006.

A. W. P. Roming, E. Th. Kennedy, O. K. Mason, et al. The *Swift* Ultra-Violet/Optical Telescope. *arXiv:astro-ph/0507413*, July 2005.

A. Rossi, S. Klose, P. Ferrero, et al. A deep search of the host galaxies of gamma-ray bursts with no detected optical afterglow. *Astronomy and Astrophysics*, 545:A77–A104, 2012.

G. B. Rybicki and A. P. Lightman. *Radiative Procceses in Astrophysics*. Wiley-Interscience, 1979.

T. Sakamoto, D. Q. Lamb, C. Graziani, et al. High energy transient explorer 2 observations of the extremely soft X-Ray Flash XRF 020903. *The Astrophysical Journal*, 602:875–885, February 2004.

T. Sakamoto, L. Barbier, S. D. Barthelmy, et al. Confirmation of the E_{peak}^{src}-E_{iso} (Amati) relation from the X-Ray Flash XRF 050416A observed by the *Swift* Burst Alert Telescope. *The Astrophysical Journal*, 636:L73–L76, January 2006.

R. Salvaterra, S. Campana, S. D. Vergani, et al. A complete sample of bright *Swift* long gamma-ray bursts. I. sample presentation, luminosity function and evolution. *The Astrophysical Journal*, 749:68–74, April 2012.

R. Sari and P. Mészáros. Impulsive and varying injection in gamma-ray burst afterglows. *The Astrophysical Journal*, 535:L33–L37, May 2000.

R. Sari and T. Piran. Predictions for the very early afterglow and the optical flash. *The Astrophysical Journal*, 520:641–649, August 1999.

R. Sari, T. Piran, and R. Narayan. Spectra and light curves of gamma-ray burst afterglows. *The Astrophysical Journal*, 497:L17–L20, April 1998.

E. F. Schlafly and D. P. Finkbeiner. Measuring reddening with sloan digital sky survey stellar spectra and recalibrating SFD. *The Astrophysical Journal*, 737:103–115, August 2011.

T. Schweyer, P. Wiseman, P. Schady, et al. *GCN Circular*, #17212, 2014.

K. Siellez, M. Boër, and B. Gendre. Simultaneous event detection rates by electromagnetic and gravitational wave detectors in the advanced era of LIGO and Virgo. *Monthly Notices of the Royal Astronomical Society*, 437:649–655, January 2014.

E. Sonbas, J. R. Cummings, V. D'Elia, et al. *GCN*, #17206, 2014.

M. Sparre and R. L. C. Starling. A serach for thermal X-ray signatures in gamma-ray bursts - ii. The *Swift* sample. *Monthly Notices of the Royal Astronomical Society*, 427:2965–2974, December 2012.

R. L. C. Starling, K. L. Page, A. Pe'er, et al. A search for thermal X-ray signatures in gamma-ray bursts - I. *Swift* bursts with optical suprenovae. *Monthly Notices of the Royal Astronomical Society*, 427:2950–2964, December 2012.

G. Stratta, F. Fiore, L. A. Antonelli, et al. Absorption in gamma-ray burst afterglows. *The Astrophysical Journal*, 608:846–864, June 2004.

G. Tagliaferri, M. Goad, G. Chincarini, et al. An unexpectedly rapid decline in the X-ray afterglow emission of long γ-ray bursts. *Nature*, 436:985–988, August 2005.

A. Trotter, J. Haislip, D. Reichart, et al. *GCN Circular*, #17210, 2014a.

A. Trotter, J. Haislip, D. Reichart, et al. *GCN Circular*, #17221, 2014b.

T. N. Ukwatta, S. D. Barthelmy, W. H. Baumgartner, et al. *GCN Circular*, #17213, 2014.

J. van Paradijs, P. J. Groot, T. Galama, et al. Transient optical emission from the error box of the γ-ray burst of 28 February 1997. *Nature*, 386:686–689, April 1997.

S. Vaughan, M. R. Goad, A. P. Beardmore, et al. *Swift* observations of the X-ray-bright GRB 050315. *The Astrophysical Journal*, 638:920–929, February 2006.

D. Watson, T. Zafar, A. C. Andersen, et al. Helium in antal HII regions: The origin of the X-ray absorption in gamma-ray burst afterglows. *The Astrophysical Journal*, 768:23–32, May 2013.

R. Willingale, P. T. O'Brien, J. P. Osborne, et al. Testing the standard fireball model of gamma-ray bursts using late X-ray afterglows measured by *Swift*. *The Astrophysical Journal*, 662: 1093–1110, June 2007.

S. E. Woosley. Gamma-ray bursts from stellar mass accretion disks around black holes. *The Astrophysical Journal*, 405:273–277, March 1993.

Y. Yatsu, N. Kawai, T. Shimokawabe, et al. Development of MITSuME-Multicolor imaging telescopes for survey and monstrous explosions. *Elsevier proceeding*, 40:434–437, December 2007.

D. Yonetoku, T. Murakami, T. Nakamura, et al. Gamma-ray burst formation rate inferred from the spectral peak energy-peak luminosity relation. *The Astrophysical Journal*, 609:935–951, 2004.

H. F. Yu. *GCN Circular*, #17216, 2014.

T. Zafar, D. Watson, J. P. U. Fynbo, et al. The extinction curves of star-forming regions from z=0.1 to 6.7 using GRB afterglow spectroscopy. *Astronomy and Astrophysics*, 532:A143–A173, 2011.

B. Zhang. Open questions in grbs physics. *Comptes Rendeus Physique*, 12:206–225, April 2011.

B. Zhang, Y. Z. Fan, J. Dyks, et al. Physical processes shaping gamma-ray burst X-ray afterglow light curves: theoretical implications from the *swift* X-ray telescope observations. *The Astrophysical Journal*, 642:354–370, May 2006.

B. Zhang, B. B. Zhang, F. J. Virgili, et al. Discerning the physical origins of cosmological gamma-ray bursts based on multiple observational criteria: the cases of z=6.7 GRB 080913, z=8.2 GRB 090423, and some short/hard GRBs. *The Astrophysical Journal*, 703:1696–1724, 2009.

Appendix A

GRB 141221A: gone is the wind

O. Bardho,[1,2]★ B. Gendre,[1,3,4]★ A. Rossi,[2] L. Amati,[2] J. Haislip,[5] A. Klotz,[6]
E. Palazzi,[2] D. Reichart,[5] A. S. Trotter[5,7] and M. Boër[1]★

[1]*ARTEMIS, CNRS UMR 5270, Université Côte d'Azur, Observatoire de la Côte d'Azur, boulevard de l'Observatoire, CS 34229,*
F-06304 Nice Cedex 04, France
[2]*IASF Bologna-INAF, via P. Gobetti 101, I-40129 Bologna, Italy*
[3]*Etelman Observatory, St Thomas, VI 00802, USA*
[4]*University of the Virgin Islands, 2 John Brewer's Bay Road, St Thomas, VI 00802, USA*
[5]*Department of Physics and Astronomy, University of North Carolina at Chapel Hill, Campus Box 3255, Chapel Hill, NC 27599, USA*
[6]*IRAP, CNRS, Université de Toulouse, 9 avenue du colonel Roche, F-31028 Toulouse Cedex 4, France*
[7]*Department of Physics, NC A&T State University, 1601 E. Market St, Greensboro, NC 27411, USA*

ABSTRACT

GRB 141221A was observed from infrared to soft gamma-ray bands. Here, we investigate its properties, in light of the standard model. We find that the optical light curve of the afterglow of this burst presents an unusual steep/quick rise. The broad-band spectral energy distribution taken near the maximum of the optical emission presents either a thermal component or a spectral break. In the former case, the properties of the afterglow are then very unusual, but could explain the lack of apparent jet breaks in the *Swift* light curves. In the latter case, the afterglow properties of this burst are more usual, and we can see in the light curves the passing through of the injection and cooling frequencies within the optical bands, not masked by a reverse shock. This model also excludes the presence of a stellar wind, challenging either the stellar progenitor properties, or the very stellar nature of the progenitor itself. In all cases, this burst may be a part of a Rosetta stone that could help to explain some of the most striking features discovered by *Swift* during the last 10 years.

Key words: gamma-ray burst: individual: GRB 141221A.

1 INTRODUCTION

Since the launch of the *Swift* satellite in 2004 (Gehrels et al. 2004), hundreds of gamma-ray bursts (GRBs; see Kumar & Zhang 2015, for a review) have been detected, localized and followed both on-board and by telescopes on the ground. This led to a very large sample of events presenting virtually all possible aspects of the standard model (see Rees & Mészáros 1992; Mészáros & Rees 1997; Panaitescu, Mészáros & Rees 1998, for a complete description of the model). Several events have been followed in optical with rapid robotic telescopes while the prompt emission was still active or recently concluded, and in a fair number of cases a rising behaviour has been observed in this band (see for instance Gendre et al. 2012).

This rise of the optical wavelength emission can be understood in two different ways: either it is the initial part of the forward shock, which can be observed until the injection frequency ν_m crosses the observational band, or we see the signature of the reverse shock (e.g. Sari & Piran 1999). Both phenomena can be interleaved, complicating the analysis.

GRB 141221A is one of these 'optically rising' bursts. It was detected by *Swift* at 08:07:10 UT (hereafter T_0) on 2014 December 21

(Sonbas et al. 2014). The duration of the burst, while not exceptional ($T_{90} = 36.9 \pm 4.0$ s, Ukwatta et al. 2014), allowed the TAROT and Skynet robotic observatories to start the observation while the prompt emission was still active. While in other cases the rise was smooth and not extreme, in this case the optical emission increased very quickly and presented other features usually not seen; the purpose of this work is to investigate those features.

In Section 2 we present the data for this event. We explain the data reduction in Section 3, and present the spectral and temporal analyses in Section 4. We then discuss our results in Section 5, before concluding.

In the remainder of this paper, all errors are quoted at the 90 per cent confidence level (except when otherwise stated), and we use a flat Λ-cold-dark-matter model for the Universe, with $H_0 = 70 \, \mathrm{km \, s^{-1} \, Mpc^{-1}}$, $\Omega_m = 0.3$ and $\Omega_\Lambda = 0.73$. We will use the standard notation $F_\nu \propto t^{-\alpha} \nu^{-\beta}$.

2 OBSERVATIONS

2.1 High-energy data

Swift-BAT (Burst Alert Telescope) *and Fermi-GBM* (Gamma-ray Burst Monitor): GRB 141221A triggered both instruments (Ukwatta et al. 2014; Yu 2014), at nearly the same time (08:07:10 UT for *Swift*,

★ E-mail: Onelda.Bardho@oca.eu (OD); Bruce.Gendre@uvi.edu (BG); Michel.Boer@unice.fr (MB)

08:07:11.22 UT for *Fermi*). The recorded duration is, however, longer in the BAT compared to GBM (23.8 s), as one can expect from the larger effective area (and hence better sensitivity) of BAT/*Swift*.

Swift-XRT: the X-Ray Telescope (XRT) observed the burst position between $T_0 + 64$ s and $T_0 + 34.9$ ks (Beardmore et al. 2014; Maselli et al. 2014), mostly in Photon Counting (PC) mode. The afterglow was clearly detected in X-rays.

2.2 Optical and infrared data

Table 1 presents a log of the observations and the data from the instruments that are used in this work.

Swift-UVOT: the observations started at $T_0 + 84$ s (Marshall & Sonbas 2014). The afterglow is clearly detected.

TAROT La Silla: the observations at TAROT La Silla (Boër et al. 2003) started at $T_0 + 31.2$ s and lasted for about 41 min, until the

Table 1. Optical data converted into the AB System and corrected for Galactic extinction.

Mid time (s)	Filter	Magnitude AB System	Telescope	Reference[a]	Mid time (s)	Filter	Magnitude AB System	Telescope	Reference[a]
65.46	R	<16.76	TAROT	(1)	57.00	V	<16.72	Skynet	(1)
71.46	R	16.18 ± 0.2	TAROT	(1)	69.00	V	$17.00^{+0.95}_{-0.54}$	Skynet	(1)
77.46	R	15.84 ± 0.2	TAROT	(1)	84.00	V	$16.66^{+0.24}_{-0.19}$	Skynet	(1)
83.46	R	15.66 ± 0.2	TAROT	(1)	101.00	V	$15.93^{+0.12}_{-0.10}$	Skynet	(1)[b]
89.46	R	15.76 ± 0.30	TAROT	(1)	123.00	V	$16.21^{+0.08}_{-0.08}$	Skynet	(1)
119.60	R	15.63 ± 0.03	TAROT	(1)	150.00	V	$16.25^{+0.08}_{-0.08}$	Skynet	(1)
160.10	R	15.52 ± 0.03	TAROT	(1)	177.00	V	$16.23^{+0.08}_{-0.07}$	Skynet	(1)
200.70	R	15.56 ± 0.03	TAROT	(1)	205.00	V	$16.19^{+0.08}_{-0.07}$	Skynet	(1)
241.00	R	15.58 ± 0.03	TAROT	(1)	242.00	V	$16.28^{+0.05}_{-0.05}$	Skynet	(1)
281.30	R	15.55 ± 0.03	TAROT	(1)	290.00	V	$16.49^{+0.07}_{-0.06}$	Skynet	(1)
351.70	R	15.76 ± 0.09	TAROT	(1)	337.00	V	$16.44^{+0.06}_{-0.05}$	Skynet	(1)
446.30	R	16.33 ± 0.02	TAROT	(1)	384.00	V	$16.61^{+0.07}_{-0.06}$	Skynet	(1)
611.00	r'	16.54 ± 0.1	GROND	(2)	451.00	V	$16.77^{+0.04}_{-0.04}$	Skynet	(1)
760.60	R	16.79 ± 0.02	TAROT	(1)	539.00	V	$16.96^{+0.05}_{-0.05}$	Skynet	(1)
861.20	R	16.84 ± 0.08	TAROT	(1)	627.00	V	$16.96^{+0.05}_{-0.05}$	Skynet	(1)
1074.40	R	17.11 ± 0.08	TAROT	(1)	636.00	V	$17.35^{+0.26}_{-0.26}$	UVOT	(3)
1327.50	R	17.38 ± 0.08	TAROT	(1)	716.00	V	$17.19^{+0.06}_{-0.06}$	Skynet	(1)
2011.00	R	17.98 ± 0.08	TAROT	(1)	804.00	V	$17.40^{+0.07}_{-0.07}$	Skynet	(1)
48.00	I	$17.05^{+0.65}_{-0.42}$	Skynet	(1)	931.00	V	$17.49^{+0.06}_{-0.05}$	Skynet	(1)
68.00	I	$15.97^{+0.12}_{-0.11}$	Skynet	(1)	1098.00	V	$17.77^{+0.07}_{-0.07}$	Skynet	(1)
85.00	I	$15.46^{+0.07}_{-0.06}$	Skynet	(1)	1266.00	V	$17.98^{+0.10}_{-0.09}$	Skynet	(1)
102.00	I	$15.25^{+0.06}_{-0.06}$	Skynet	(1)	1433.00	V	$18.19^{+0.13}_{-0.12}$	Skynet	(1)
123.00	I	$15.19^{+0.04}_{-0.03}$	Skynet	(1)	1600.00	V	$18.43^{+0.17}_{-0.15}$	Skynet	(1)
150.00	I	$15.23^{+0.03}_{-0.03}$	Skynet	(1)	85 523.00	V	$22.23^{+3.83}_{-1.10}$	Skynet	(1)
177.00	I	$15.26^{+0.03}_{-0.03}$	Skynet	(1)	611.00	g'	17.01 ± 0.1	GROND	(2)
205.00	I	$15.45^{+0.04}_{-0.04}$	Skynet	(1)	611.00	z'	16.07 ± 0.1	GROND	(2)
242.00	I	$15.52^{+0.03}_{-0.03}$	Skynet	(1)	611.00	J	15.68 ± 0.1	GROND	(2)
290.00	I	$15.60^{+0.03}_{-0.03}$	Skynet	(1)	611.00	H	15.39 ± 0.1	GROND	(2)
337.00	I	$15.62^{+0.03}_{-0.03}$	Skynet	(1)	611.00	K	15.29 ± 0.1	GROND	(2)
384.00	I	$15.77^{+0.04}_{-0.04}$	Skynet	(1)	561.50	b	17.73 ± 0.21	UVOT	(3)
451.00	I	$15.85^{+0.02}_{-0.02}$	Skynet	(1)	421.00	u	18.47 ± 0.07	UVOT	(3)
539.00	I	$16.11^{+0.03}_{-0.03}$	Skynet	(1)					
611.00	i'	16.35 ± 0.1	GROND	(2)					
627.00	I	$16.26^{+0.04}_{-0.03}$	Skynet	(1)					
716.00	I	$16.45^{+0.04}_{-0.04}$	Skynet	(1)					
804.00	I	$16.54^{+0.04}_{-0.04}$	Skynet	(1)					
931.00	I	$16.71^{+0.03}_{-0.03}$	Skynet	(1)					
1098.00	I	$16.99^{+0.04}_{-0.04}$	Skynet	(1)					
1265.00	I	$17.27^{+0.06}_{-0.06}$	Skynet	(1)					
1433.00	I	$17.36^{+0.07}_{-0.06}$	Skynet	(1)					
1600.00	I	$17.75^{+0.10}_{-0.09}$	Skynet	(1)					
85 609.00	I	$21.45^{+0.67}_{-0.43}$	Skynet	(1)					

[a]References for the data: (1) this work; (2) Schweyer et al. (2014); (3) Marshall & Sonbas (2014).
[b]This point exhibits an instrumental bias and has not been included in the analysis.

beginning of sunrise (Klotz et al. 2014). The burst is not detected between 31 and 68 s, with a limiting magnitude $R_{lim} = 16.6$. After that time, the burst is clearly detected for the remainder of the observation.

Skynet PROMPT-CTIO: the observations with Skynet PROMPT-CTIO (two 14 inch telescopes), at Cerro Tololo, Chile (Reichart et al. 2005), started at $T_0 + 45$ s and lasted for 27.25 min (Trotter et al. 2014a,b). 44 exposures were taken in the *V* and *I* bands, ranging from 5 to 160 s. The optical afterglow was clearly detected with a rising light curve at $t = 2$ min and peaks at $I = 14.8$. Skynet observed the afterglow again at $T_0 + 23.0$ h for 1.5 h, taking 64 exposures of 160 s each in *V* and *I* bands.

GROND: GROND (Greiner et al. 2008) observations started at $T_0 + 142$ s (Schweyer et al. 2014), and continued for 18 min. The afterglow was clearly detected.

Keck II telescope: spectroscopic observations with the Keck II telescope were performed from $T_0 + 1.78$ h to $T_0 + 2.15$ h. Several lines were detected (Mg II doublet and Fe II), putting this burst at a redshift of $z = 1.452$ (Perley, Cao & Cenko 2014).

3 DATA REDUCTION

3.1 Optical/IR data

The TAROT data were reduced using the standard procedure already discussed in Klotz, Vachier & Boër (2008). We converted the observed signal from the clear filter to the *R* filter by calibrating the magnitude of the afterglow against nearby stars of similar colour.

Subsets of the Skynet images were stacked to maximize the signal-to-noise ratio (SNR). Calibration of these images was performed using three stars in the field from the AAVSO APASS

DR7 catalogue. The *BVg'r'i'* magnitudes from APASS were converted to *BVRI* Vega magnitudes using transformations provided by AAVSO (Hendon, private communication). Standard bias, dark and flat corrections were applied to all images. Consecutive images were grouped and stacked in a way which maximizes the SNR of the afterglow while minimizing the loss of temporal resolution. The afterglow and a single primary calibration star were photometered in each stacked image and the resulting calibration offset was recorded. A master calibration stack was then generated for each filter by combining all available images. For each master calibration stack, the primary calibration star was photometered as well as the two secondary calibration stars. By comparing the offset obtained from the secondary calibration stars to that obtained from the primary calibration star, a calibration correction is calculated and applied to all afterglow photometry. The remaining data have been gathered from the literature and are compiled in Table 1. Fig. 1 displays the resulting light curves.

All magnitudes were then converted into the AB system, if required. The correction for the Galactic extinction was applied at the same time, using a value of $E(B - V) = 0.024$ (Schlafly & Finkbeiner 2011). The reddening due to the host galaxy is left as free parameter in fits to be discussed below. This leads to the corrections listed in Table 2. We then computed from the corrected magnitudes the flux density, using a zero-point value of 23.926. The final flux density light curves are presented in Fig. 1.

3.2 *Fermi* data

GBM data for GRB 141221A were downloaded from the NASA/Goddard Space Flight Center (GSFC) *Fermi* GBM Archive. The extraction of GBM data was done by using only the Na I
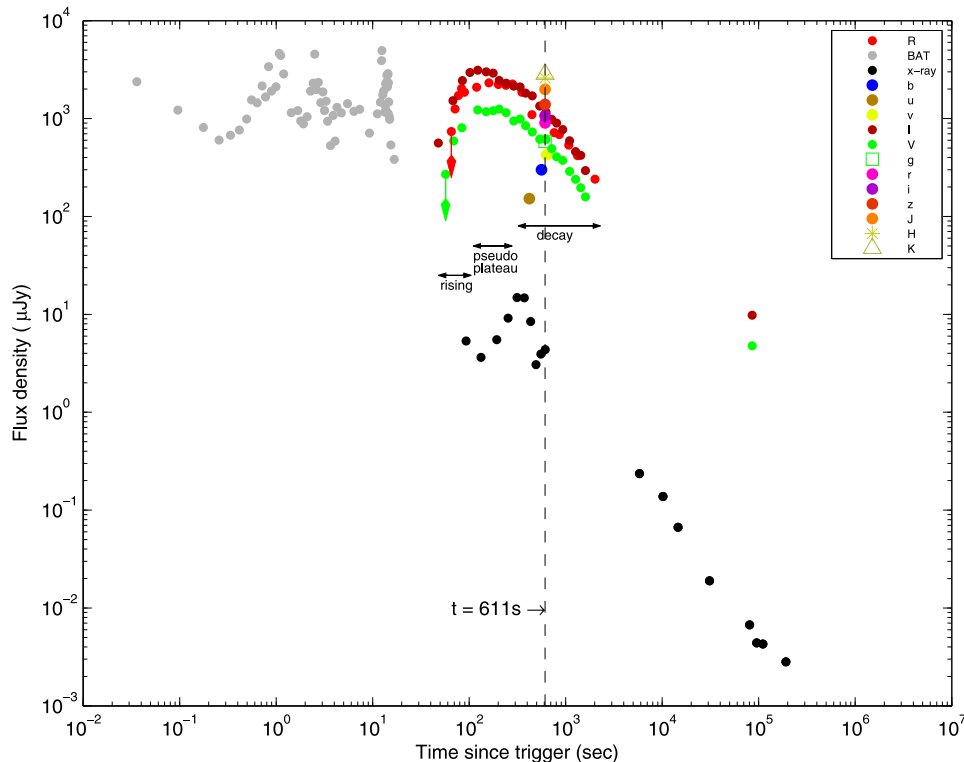

Figure 1. Flux density light curve of GRB 141221A. The vertical dashed line represents the epoch when the spectral energy distribution (SED) was extracted (see text for details).

Table 2. Corrections to magnitudes due to Galactic extinction.

Filter	Correction
u	0.117
b	0.092
V	0.075
v'	0.104
g'	0.091
R	0.074
r'	0.063
I	0.041
i'	0.047
z'	0.035
J	0.019
H	0.012
K	0.080

Figure 2. Our GRB compared to the whole sample of GRBs until 2013 June. The solid line is $E_{p,i} = 110 * E_{iso}^{0.57}$, while the dashed line is the 2σ standard deviation (Amati et al. 2009).

detectors with the brightest signal in the 8 keV–1 MeV band. In the case of GRB 141221A, these detectors were Na I 01 and Na I 02. We used the task RMFIT(v432) for data reduction, using the time tagged event files (TTE) of each good detector.

As the high-energy light curve of this event consists of two pulses, we performed all analysis both on each pulse separately and on the full time interval to check for spectral variations. For that purpose, we used the 8.0–900.0-keV energy band.

3.3 X-ray data

The data for GRB 141221A were downloaded from the NASA/GSFC *Swift* Data Center and were processed using HEA-SOFT(v6.16) and the XRTDAS software version 0.13.1, with the latest calibration files available in 2015 June. We used the task XRTPIPELINE to create the clean event file and to apply the latest calibration. We then performed a screening for bad pixels and piled-up data, using the methods and corrections indicated in Romano et al. (2006) and Vaughan et al. (2005). We found that the flare observed in PC mode is piled up during the interval $T_0 + 138.2$ s $– T_0 + 619.7$ s. Lastly, we restricted the analysis to events with energy between 0.3 and 10.0 keV. This led to a net exposure of 50.53 s in the Window Timing mode (hereafter WT) and 26 251.72 s in the PC mode.

4 DATA ANALYSIS

4.1 Prompt data

As already indicated, the prompt light curve has a duration (T_{90}) of about 23.8 s in *Fermi*-GBM and about 37 s in *Swift*-BAT, and

consists of two pulses. For the spectral analysis of prompt emission we used the *Fermi*/GBM instead of *Swift*/BAT data because of the much larger energy band of the former instrument. We used XSPEC version 12 (Arnaud 1996) to fit the spectrum with a Band model (Band et al. 1993). We first fit each pulse separately (named Intervals 1 and 2, respectively), and then fit the complete spectrum. We also took an average of the two pulse results. All the results are displayed in Table 3, together with a reminder of the GCN result (Yu 2014). The low signal prevented us from fitting all the Band parameters separately, and in all cases we had to fix the β parameter to a value of -2.3. Knowing E_{peak} and the distance of this burst, we have calculated $E_{p,i} = 374 \pm 70$ keV and $E_{iso} = 2.4 \times 10^{52}$ erg. We note that these values follow the $E_{p,i} - E_{iso}$ relation (Amati, Frontera & Tavani 2002; Amati, Frontera & Guidorzi 2009), as can be seen in Fig. 2.

4.2 Temporal decay

4.2.1 X-ray

The X-ray temporal analysis was already done for the extraction of the spectral energy distribution (SED). The light curve presents a prominent flare, peaking at about 340 s. The remainder of the afterglow light curve is well fit by a simple power law, as can be seen in Table 4 and Fig. 1.

Table 3. Results of the prompt spectral fitting. Non-constrained parameters are fixed to the values indicated in square brackets

Interval	Time (s)	Exposure time (s)	α	β	C-Stat	d.o.f	$E_{p,i}$ (keV)	E_{iso} (10^{52} erg)
1	-1.024–8.704	9.728	[-1.00]	[-2.30]	431.57	241	353 ± 42	1.88 ± 0.11
2	8.704–17.408	8.704	-0.82 ± 0.38	[-2.30]	523.84	253	247 ± 77	0.83 ± 0.09
2	8.704–17.408	8.704	[-1.00]	[-2.30]	523.98	254	297 ± 61	0.88 ± 0.10
Total	-1.024–17.408	18.432	-1.24 ± 0.11	[-2.30]	558.20	240	531 ± 164	3.13 ± 0.25
Total	-1.024–17.408	18.432	[-1.00]	[-2.30]	558.97	241	328 ± 35	2.71 ± 0.14
Averaged	-1.024–17.408	18.432	[-1.00]	[-2.30]	477.77	247.5	325 ± 52	2.74 ± 0.21
GCN	-1.024–17.408	18.432	-1.07 ± 0.13	–	–	–	374 ± 70	2.43 ± 0.29

Table 4. Best-fitting temporal decay indices for the *I*, *R*, *V* and X-ray bands. Numbers in parentheses are not constrained by the fit. See text for details.

Time (s)	Filter	Model	α_1	α_2	α_3	t_{break} (s)	$t_{break,2}$ (s)	χ^2_ν	d.o.f
48–337	*I*	Broken power law	-1.6 ± 0.9	0.5 ± 0.2	–	110 ± 13	–	1.67	6
337–85 609	*I*	Broken power law	1.0 ± 0.2	1.6 ± 0.4	–	918 ± 160	–	1.53	9
281–2011	*R*	2 broken power law	1.6 ± 0.4	0.4 ± 3.2	1.3 ± 0.9	540 ± 514	906 ± 696	1.36	1
69–205	*V*	Broken power law	(-1.6)	0.1 ± 1.2	–	(109)	–	0.10	1
205–85 523	*V*	Broken power law	0.7 ± 0.1	1.3 ± 0.3	–	641 ± 125	–	0.70	12
5800–191 504	X-ray	Power law	1.4 ± 0.2	–	–	–	–	1.31	6

Table 5. Simple-power-law decay fit of the *I*, *R*, *V* bands. See text for details.

Filter	α	χ^2_ν	d.o.f
I	1.12 ± 0.10	3.83	11
V	0.91 ± 0.10	2.57	14
R	1.04 ± 0.22	10.6	6

4.2.2 Optical

The optical light curves are more complex than the X-ray one. They present a rise, a pseudo-plateau and a decay. We split the study in two parts, namely the rising and the decaying parts.

For the rise, we used a broken-power-law model. This gives us the end time of the fast rise and the start of the pseudo-plateau phase. In a few cases, the lack of data prevented an accurate measure, and we indicate these as numbers in parentheses in Table 4. This is the case for the *R* band, which we attribute to an instrumental bias (see below).

For the decay, we first tried a simple-power-law model. As one can see in Table 5, this model is strongly rejected in all bands. We then inserted a break in the power laws, obtaining good fits in the *V* and *I* bands (see Table 4). However, this model, surprisingly, still does not fit the *R* band. In that band, we need a double-broken power-law in order to obtain a correct fit. At that point, the degrees of freedom are too low to ensure a correct measurement of the errors.

This double-broken-power-law model mimics the standard *Swift* X-ray light curve (i.e. a steep–flat–steep shape), but is not seen in the other bands. We explain this feature by the fact that these

R-band measurements come from the TAROT telescope, which was unfiltered to maximize its sensitivity. We have normalized the magnitudes to the Cousin *R* band assuming a template afterglow spectrum that does not contain any break. The TAROT CCD camera is sensitive from the *I* to the *V* bands (the *B* sensitivity is very low). A spectral break that appears partly in the observation window will not be accounted for. This can introduce an error in the reduced *R* magnitude that will depend on the position of the break. If the break is in the blue part of the spectrum, then the *R* magnitude will be underestimated, and vice-versa for the opposite case. The crossing of a spectral break would then translate into a steep–flat–steep shape in the light curve during the whole time of the crossing. This is not observed for the other bands (*I* and *V*) as standard filters have been used. The fits in the *V* and *I* bands (decay) are presented in Fig. 3.

4.3 Afterglow spectrum

We started by analysing the XRT spectrum alone, independently of the optical data. This is because at high energy (above 2 keV), the spectrum is not influenced by the surrounding medium and the column density, and thus the X-ray spectrum allows us to derive the intrinsic power-law index. We extracted three spectra, one in WT mode and two in PC mode (during the flare, and after the flare), and fit these with a power-law model absorbed twice (one let free to vary at the distance of the burst, the second fixed to the galactic value in the direction of the burst, $N_H^{gal} = 2.27 \times 10^{20}$ cm^{-2}). The data are consistent with no spectral variation, though we note that the error bars are large due to the low flux of the afterglow. The results of these fits are presented in Table 6. The lack of spectral

Figure 3. The best fit in the *I* (left) and *V* (right) bands with a power-law decay, starting from the end of the pseudo-plateau. The lower parts of each figure show the residuals of the fits.

Table 6. X-ray spectral analysis, independent of the optical measurements. See text for details.

Interval (s)	Mode	$N_{\mathrm{H}}^{\mathrm{host}}$ $(10^{22}\ \mathrm{cm}^{-2})$	β_X	χ^2_ν	d.o.f.
60–90	WT	$0.27^{+2.3}_{-0.27}$	$0.7^{+0.7}_{-0.5}$	1.02	6
100–1000	PC	$0.9^{+0.5}_{-0.4}$	$1.0^{+0.4}_{-0.4}$	0.96	15
3000–11 000	PC	$0.5^{+0.6}_{-0.4}$	$1.0^{+0.4}_{-0.4}$	0.89	7

Figure 4. Hardness ratio of the X-ray observation. We used the hard and soft bands of 2.0–10.0 keV and 0.5–2.0 keV, respectively, only in PC mode.

variation is clearly confirmed by an analysis of the hardness ratio (using the hard and soft bands of 2.0–10.0 keV and 0.5–2.0 keV, respectively) presented in Fig. 4. While we see at 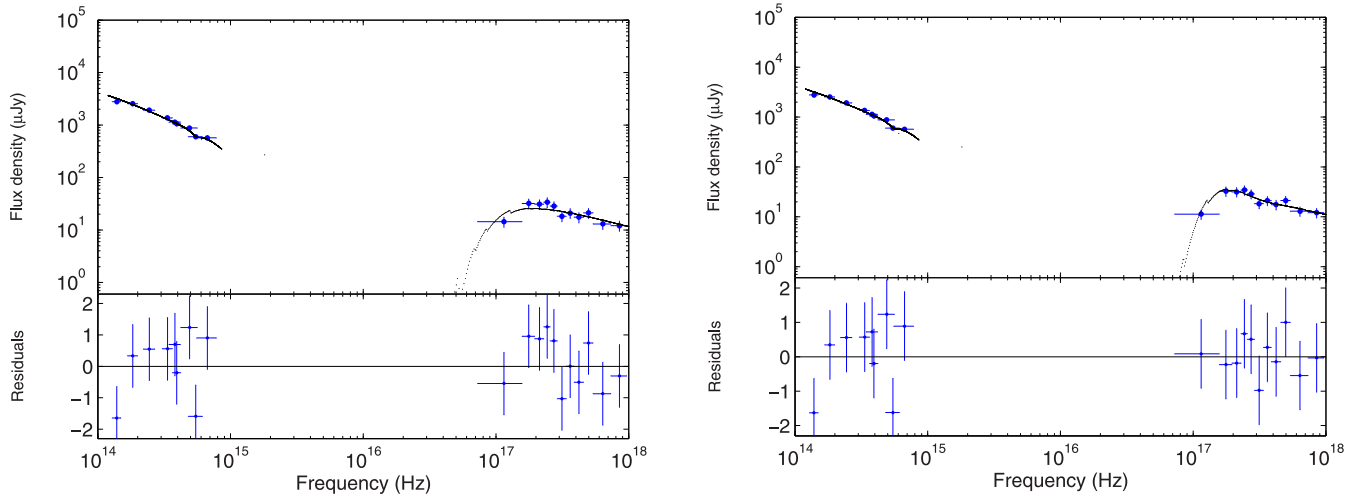the end of the flare a possible hardening of the spectrum, the error bars are still consistent with no spectral variation at the 3σ level.

Once we had the information on the power-law spectral index at high energy, we built the SED, this time using all data available. We extracted the SED where the data were the most numerous, at about 611 s post-burst (see Fig. 1). This corresponds to the end of the flare in X-ray and the decay phase of the optical band. In X-ray, we used the data taken between 350 and 619.7 s, and normalized them to the underlying afterglow flux. This last point is important:

as there is no hint of flare in the optical light curve, it should not be linked to the X-ray flare. The non-variability of the hardness ratio makes us confident that this renormalization is enough to correct for the presence of the flare. All data (including the optical data) were then imported into XSPEC for the spectral fitting.

To model the SED, we consider single power law, double power law and thermal components (see Table 7). In all cases, we added foreground absorption by our own Galaxy (this absorption was fixed to the measured values of Kalberla et al. (2005), the optical extinction being corrected before the insertion into XSPEC), and by the distant host galaxy. We consider the three standard extinction laws, i.e. the Milky Way (MW), the Large Magellanic Cloud (LMC) and the Small Magellanic Cloud (SMC) ones. In all cases, the high-energy power-law index was allowed to vary freely only within the measured X-ray confidence interval. We first considered a simple-power-law extincted model. Even if the fit quality seems good (see Table 7), an analysis of the residuals shows that this model does not fit the data correctly: it exhibits a lack of emission in the soft X-ray part of the SED (see Fig. 5). We then inserted a thermal component into the model, and redid the analysis. This time, both the quality indicator of the fit and the residuals are in agreement with a good solution. We also tested the hypothesis of a cooling break, i.e. a broken power law with the two spectral indices linked together by a difference of $\beta_X = \beta_o + 0.5$, which also provides an acceptable fit.

As can be seen, the addition of the optical data strongly constrains the spectral index of the power law to a very low value. On the other hand, from this fit we cannot discriminate between a Galactic and an LMC law of extinction. We present the best-fitting SED (assuming a power-law model with an additional thermal component) in Fig. 5, using the LMC law, which is more common for GRBs compared to the MW law (Stratta et al. 2004).

5 DISCUSSION

5.1 The thermal component

We first consider the possibility that the thermal component seen in the SED is real. This would not be the first time such a component has been observed in the *Swift* era (Sparre & Starling 2013; Starling et al. 2013). It has been explained either as the shock breakout of the supernova on to the surface of the progenitor or the emission of a hot cocoon protecting the jet during its travel into the progenitor

Table 7. Results of the spectral analysis of the SED. β_o is the power-law index in case of a single power law. In case of a broken power law, this is the spectral index of the low-energy segment, the high-energy segment being linked to it by the relation $\beta_X = \beta_o + 0.5$. See text for details.

Model	Extinction law	$N_{\mathrm{H,host}}$ $(\times\,10^{22}\ \mathrm{cm}^{-2})$	R_V (mag)	$E(B-V)$ (mag)	β_o	Temperature or break energy (keV)	χ^2_ν	d.o.f
pow	MW	0.4 ± 0.3	3.08	0.12 ± 0.02	$0.63^{+0.03}_{-0.02}$	–	0.7674	16
	LMC	0.4 ± 0.3	3.16	0.12 ± 0.02	0.63 ± 0.02	–	0.9855	16
	SMC	0.4 ± 0.3	2.93	0.12 ± 0.02	$0.63^{+0.03}_{-0.02}$	–	1.3111	16
pow+bbody	MW	$1.3^{+1.9}_{-1.0}$	3.08	0.11 ± 0.02	0.63 ± 0.03	$0.14^{+0.17}_{-0.04}$	0.607	14
	LMC	$1.3^{+1.9}_{-1.0}$	3.16	0.12 ± 0.02	0.64 ± 0.03	$0.13^{+0.16}_{-0.05}$	0.862	14
	SMC	1.3 ± 0.9	2.93	0.12 ± 0.02	0.63 ± 0.03	$0.14^{+0.17}_{-0.05}$	1.229	14
cooling	MW	$0.8^{+0.5}_{-0.4}$	3.08	$0.14^{+0.05}_{-0.04}$	0.5 ± 0.2	<0.17	0.645	15
break	LMC	$0.6^{+0.5}_{-0.3}$	3.16	$0.18^{+0.02}_{-0.06}$	$0.3^{+0.3}_{-0.1}$	$0.012^{+0.8}_{-0.01}$	0.7	15
	SMC	0.7 ± 0.3	2.93	$0.17^{+0.03}_{-0.05}$	$0.37^{+0.03}_{-0.09}$	$0.03^{+1.6}_{-0.028}$	1.15	15

Figure 5. The SED of GRB 141221A, fit with various models. On the left, a simple-power-law model. On the right, a simple power law plus a thermal component. In both cases, we use the LMC extinction law to fit the optical data. The bottom panels show the residuals for each model.

(Butler 2007). We note incidentally that this last explanation was also proposed to describe the early emission of ultralong GRBs (Gendre et al. 2013; Piro et al. 2014), even if, as in this case, the burst does not belong to that class of events. As no supernova has been reported for GRB 141221A, we do favour the hypothesis of the hot cocoon.

If this component is really present, then the SED indicates that the optical and X-ray emissions are linked together, and are thus due to the same emission mechanism. Indeed, at late times, all the temporal decay indices are compatible, within errors. However, the SED is extracted before the final break of the *I* band, and thus this should also apply to earlier measurements. We do not see any evidence of a break in the X-ray light curve: this can be explained by the presence of the flare, which masks out the actual evolution of the afterglow. Moreover, the break times of the *I* and *V* magnitudes are compatible, within errors.

This light-curve break is then achromatic, which is consistent with a jet break (Rhoads 1997, 1999). We obtain a value of $p = 1.28 \pm 0.06$ which is extremely low. In addition, the jet break time is also extreme (about 750 s, while a common pre-*Swift* value is of the order of days; Gendre, Corsi & Piro 2006). This would lead to a jet opening angle of 1.3 deg (assuming the standard law of Sari & Piran 1999), and could explain why in most cases no jet break is observed for *Swift* bursts: the break is looked for around a few hours (or days) after the trigger, and not at that earlier time.

In addition to this surprising value of the jet opening angle (that would put strong constraints on the Star Formation Rate of massive stars in the Universe), the only argument against this hypothesis is the *R* band behaviour, that does not follow the *V* and *I* bands. In the previous section, we have explained this behaviour by the fact that the break time was not identical in all bands. If we suppose a constant break time, we cannot explain the *R* band behaviour.

5.2 The rising and early decay of the afterglow

Let us now assume that the thermal component is not real, and instead use a broken power model for the SED. At a late time, all the temporal decay indices are compatible, within errors. Now, the SED tells us that the X-ray and optical emissions are not linked to the same emission mechanism at the time of the SED (611 s). We can then assume that the various breaks we see are due to the passing

through of a specific frequency into the observation bands, and that at a late time (> about 1000 s), the crossing of this frequency has ended and all the emission is due to the same emission mechanism.

The temporal break times in the *I* and *V* bands indicate that this specific frequency is decreasing with time, and, as already explained, the *R*-band behaviour is also compatible with that hypothesis. This leads us to exclude the passing through of the cooling frequency in a wind medium, as this frequency increases with time in such a case (Chevalier & Li 1999; Panaitescu & Kumar 2000). If we still assume the wind medium, the only remaining option is the injection frequency, ν_m. However, the spectral index before the crossing ($0.3^{+0.3}_{-0.1}$) would lead to a value of p lower than 1, which is not physical. We thus can conclude that these breaks cannot be explained in the case of the wind medium.

The situation is different in case of the interstellar medium (ISM). There, we can logically assume that the last two breaks are linked to the injection and cooling breaks, respectively. The injection and cooling frequencies vary as $t^{-1.5}$ and $t^{-0.5}$, respectively. Taking into account the errors on the break times, all break measurements are compatible with this explanation. After the cooling break, the spectral and the temporal decay indices are all compatible with a value of $p \sim 2.5 \pm 0.3$. The early spectral index (before the cooling break, as measured in the optical) should be $\beta = 0.7 \pm 0.2$, compatible with the measurement ($0.3^{+0.3}_{-0.04}$).

In this scenario, the end of the 'pseudo-plateau' phase is the injection break, i.e. the peak of the afterglow. Again, the variation of the break time between the *V* and *I* bands is consistent with this hypothesis. Then, however, the temporal decay indices of the 'pseudo-plateau' should become negative. This does not agree with the model. We explain it by the contribution of a small reverse shock that masks the peak of the emission. We can then, assuming the surrounding medium density to be equal to 1, and the efficiency of the fireball in radiating its energy to be 30 per cent, compute the microphysical parameters of the fireball, using the work of Panaitescu & Kumar (2000). Doing so, we obtain the fireball total energy ($E = 8 \times 10^{52}$ erg), the magnetic parameter ($\epsilon_B = 5 \times 10^{-2}$) and the electron parameter ($\epsilon_e = 3 \times 10^{-3}$). These numbers are relatively normal (see e.g. Gendre, Galli & Boër 2008), albeit ϵ_B is slightly higher than usually seen. We thus have a complete description of the afterglow of this burst. We note, however, the total absence of a stellar wind in that model.

Chevalier, Li & Fransson (2004) have pointed out the complex surrounding medium of a GRB. However, assuming that the progenitor for all long GRBs is a stellar object (Woosley 1993), we still should observe a small portion of the light curve where a wind environment should be present. Here, from about 200 s after the trigger to the end of the observations, the medium is compatible with an ISM only. It is a well-known fact that most of *Swift* bursts are compatible with an ISM, but a degeneracy prevents excluding the wind medium hypothesis (Chevalier et al. 2004). Here, we have the proof that the wind medium is rejected from nearly the start of the afterglow, leaving only extreme constraints on the stellar physics in order to suppress the stellar wind from the progenitor. It is beyond the scope of this paper to introduce such a stellar model; however, GRBs are known to have weak stellar winds (e.g. Gendre, Piro & De Pasquale 2004; Gendre et al. 2013), and thus such a model would be very useful. We conclude this section by noting that the intrinsic values of E_{B-V} and N_H are low, and thus again are compatible with a low density around this GRB.

5.3 Absorption and extinction

From our analysis, it turns out that we obtain a better solution using an LMC extinction law, because the observed GROND *g* band is best fit by 2175-Å absorption feature present in LMC (and MW). We note that best-fitting solutions with LMC or MW dust have already been observed (e.g. Kann, Klose & Zeh 2006; Krühler et al. 2008; Kann et al. 2010), even if other models may be more appropriate (Stratta et al. 2004). However, given that these data were obtained from the preliminary photometry quoted in Schweyer et al. (2014), and that they do not have appreciable influence on the fitted parameter values, we prefer to leave this argument for a future work when better data will be available.

All the spectral models we tried favour a slightly dusty environment with $E(B-V) \sim 0.1$–0.2 (see Table 7). These values are not unusual (Kann et al. 2010; Greiner et al. 2011; Zafar et al. 2011), most of all at the distance of GRB 141221A (Kann et al. 2006; Covino et al. 2013). The observed $N_{H,host}$ is also in agreement with those found for other bright bursts, especially when compared with the best-fitting optical extinction in the redshift interval $1 < z < 2$ (e.g. Covino et al. 2013; Watson et al. 2013). Like many other bursts, the metals-to-dust ratio ($N_{H,host}/A_V$) is in the range 1–3 $\times 10^{22}$ cm^{-2} mag^{-1} (Krühler et al. 2011; Zafar et al. 2011; Covino et al. 2013).

We finally note that the extinction is not enough to set the optical to X-ray spectral index below the value $\beta_{O-X} = 0.5$ (see Table 7), and thus we cannot consider GRB 141221A as a dark GRB (Jakobsson et al. 2004; Rossi et al. 2012).

6 CONCLUSIONS

We have analysed the observations of GRB 141221A made in optical and high-energy bands by various instruments, including TAROT and Skynet. In X-ray bands, the burst is very similar to all the previous ones observed, with a late flare. In optical bands, however, the light curve shows a rising part, a pseudo-plateau phase and various temporal breaks. We explain these breaks as due to the passing through of several specific frequencies into the optical bands. We need a minimal contribution by a reverse shock to completely explain both the optical and X-ray light curves and spectra.

An alternative hypothesis would be the presence of a thermal component, to explain the observed optical/X-ray SED. In this case, the last temporal break observed would be due to a jet effect. This,

however, would lead to various properties being, while not formally forbidden by the model, extreme, and, in addition, would lead to the presence of a thermal emission in the soft X-ray band. All of these facts are unusual and difficult to explain.

Clearly, both solutions are challenging for GRB models. In the former case, all the data point towards an absence of stellar wind during the whole phenomenon, which is in contradiction with current models. In the latter case, the microphysics parameters obtained by the model are very unusual, and in some cases not really taken into account by the model. GRB 141221A should thus be added to the short list of very constraining bursts against which each new model should be tested.

REFERENCES

Amati L., Frontera F., Tavani M., 2002, A&A, 390, 81
Amati L., Frontera F., Guidorzi C., 2009, A&A, 508, 173
Arnaud K. A., 1996, in Jacoby G., Barnes J., eds, ASP Conf. Ser. Vol. 101, Astronomical Data Analysis Software and Systems V. Astron. Soc. Pac., San Francisco, p. 17
Band D. et al., 1993, ApJ, 413, 281
Beardmore A. P., Evans P. A., Goad M. R., Osborne J. P., 2014, GCN Circ., 17211, 1
Boër M. et al., 2003, The Messenger, 113, 45
Butler N. R., 2007, ApJ, 656, 1001
Chevalier R. A., Li Z. Y., 1999, ApJ, 520, 29
Chevalier R. A., Li Z. Y., Fransson C., 2004, ApJ, 606, 369
Covino S. et al., 2013, MNRAS, 432, 1231
Gehrels N. et al., 2004, ApJ, 611, 1005
Gendre B., Piro L., De Pasquale M., 2004, A&A, 424, L27
Gendre B., Corsi A., Piro L., 2006, A&A, 455, 803
Gendre B., Galli A., Boër M., 2008, ApJ, 683, 620
Gendre B. et al., 2012, ApJ, 748, 59
Gendre B. et al., 2013, ApJ, 766, 30
Greiner J. et al., 2008, PASP, 120, 405
Greiner J. et al., 2011, A&A, 526, 30
Jakobsson P., Hjorth J., Fynbo J. P. U., Watson D., Pedersen K., Björnsson G., Gorosabel J., 2004, ApJ, 617, L21
Kalberla P. M. W., Burton W. B., Hartmann D., Arnal E. M., Bajaja E., Morras R., Pöppel W. G. L., 2005, A&A, 440, 775
Kann D. A., Klose S., Zeh A., 2006, ApJ, 641, 993
Kann D. A. et al., 2010, ApJ, 720, 1513
Klotz A., Vachier F., Boër M., 2008, Astron. Nachr., 329, 275
Klotz A., Turpin D., Boër M., Gendre B., Siellez K., Dereli H., Bardho O., Atteia J. L., 2014, GCN Circ., 17227, 1
Krühler T. et al., 2008, ApJ, 685, 376
Krühler T. et al., 2011, A&A, 534, 108
Kumar P., Zhang B., 2015, Phys. Rep. 561, 1
Marshall F. E., Sonbas E., 2014, GCN Circ., 17219, 1
Maselli A. et al., 2014, GCN Circ., 17214, 1
Mészáros P., Rees M. J., 1997, ApJ, 476, 232

Panaitescu A., Kumar P., 2000, ApJ, 543, 66

Panaitescu A., Mészáros P., Rees M. J., 1998, ApJ, 503, 314

Perley A. D., Cao Y., Cenko S. B., 2014, GCN Circ., 17228, 1

Piro L. et al., 2014, ApJ, 790, L15

Rees M. J., Mészáros P., 1992, MNRAS, 258, 41

Reichart D. et al., 2005, Nuovo Cimento C, 28, 767

Rhoads J. E., 1997, ApJ, 487, L1

Rhoads J. E., 1999, ApJ, 525, 737

Romano P. et al., 2006, A&A, 456, 917

Rossi A. et al., 2012, A&A, 545, 77

Sari R., Tsvi P., 1999, ApJ, 520, 641

Schlafly E. F., Finkbeiner D. P., 2011, ApJ, 737, 103

Schweyer T., Wiseman P., Schady P., Greiner J., 2014, GCN Circ., 17212, 1

Sonbas E., Cummings J. R., D'Elia V., Izzo L., Lien A. Y., Page K. L., Sbarufatti B., Siegel M. H., 2014, GCN Circ., 17206, 1

Sparre M., Starling R. L. C., 2013, MNRAS, 427, 2965

Starling R. L. C., Page K. L., Pe'er A., Beardmore A. P., Osborne J. P., 2013, MNRAS, 427, 2950

Stratta G., Fiore F., Antonelli A., Piro L., De Pasquale M., 2004, ApJ, 608, 846

Trotter A. et al., 2014a, GCN Circ., 17210, 1

Trotter A. et al., 2014b, GCN Circ., 17221, 1

Ukwatta T. N. et al., 2014, GCN Circ., 17213, 1

Vaughan S. et al., 2005, ApJ, 638, 920

Watson D. et al., 2013, ApJ, 768, 23

Woosley S. E., 1993, ApJ, 405, 273

Yu H. F., 2014, GCN Circ., 17216, 1

Zafar T., Watson D., Fynbo J. P. U., Malesani D., Jakobsson P., de Ugarte Postigo A., 2011, A&A, 532, 143

This paper has been typeset from a TEX/LATEX file prepared by the author.

Appendix B

Refereed proceeding in the Proceedings of Science (PoS)[1], from the conference: *Swift*: 10 Years of Discovery[2].

10 Years of XRT light curves: a general view of the X-ray afterglow

Onelda Bardho[*]

ARTEMIS (CNRS/OCA/UNS), Nice, France

E-mail: onelda.bardho@oca.eu

Michel Boër

ARTEMIS (CNRS/OCA/UNS), Nice, France

E-mail: michel.boer@unice.fr

Bruce Gendre

University of the Virgin Islands, Virgin Islands, USA

ARTEMIS (CNRS/OCA/UNS), Nice, France

E-mail: bruce.gendre@gmail.com

During the pre-*Swift* era, a clustering of light curves was observed in the X-ray, optical and infrared afterglow of gamma-ray bursts. We used a sample of 254 GRB X-ray afterglows to check this fact in the *Swift* era. We corrected fluxes for distance, time dilation and losses of energy due to cosmological effects. With all our data in hand, we faced with a problem: our data were scattered. We investigated 3 possibilities to explain this, namely: the clustering does not exist, there are problems during calibration of data, and there are instrumental problems. We finally confirm that our sample is consistent with Dainotti correlation.

---

[*]Speaker.

1. Introduction

Because of its long stay in orbit, *Swift* [1] has observed numerous Gamma-Ray Bursts (GRBs) and has helped solving a lot of mysteries related to the GRBs research. Thanks to its fast capabilities and multi-wavelength instruments, *Swift* also opened a new era in the GRB science, and one can really refer to a pre-*Swift* era and a *Swift* era. In the field of standardization of GRBs, the most tricking results are that pre-*Swift* and *Swift* era results are sometime not consistent.

For instance, in the pre-*Swift* era, the light curves of GRB afterglows were known to cluster around defined paths once corrected for any cosmological and distance effects. This was firstly stated in X-ray by [2], and then confirmed by [3] and [4]. A final (to date) check at that wavelength done by [5] by mixing pre-*Swift* and *Swift* light curves confirmed that fact: the light curves seem to cluster in two well organized groups and a third, more loosely distributed, faint group (see also Dereli et al., these proceedings, for this last group). Other groups also confirmed that fact in optical [6, 7], and infrared [8].

This changed in the *Swift* era. The profusion of X-ray light curves from the XRT allowed to study the distribution of the luminosity at a given time, and the conclusions of these works point toward no clustering in various groups, but instead in a loose and broad distribution (see for instance [9] for one of the latest of these works).

There is no obvious reason why the pre-*Swift* and *Swift* distributions of luminosities are not consistent. As a matter of consequence, we started a large project of re-analysis of a sample of X-ray afterglow light curves with known distance of the *Swift* era, in order first to confirm independently (and with the same method that was leading previously to the clusterings) this inconsistency; and second then to explain it.

Through all this paper, we will use a flat ΛCMD model of Universe, with $\Omega_m = 0.3$. All errors are quoted at the 90 % confidence level, and all methods are identical to those used in [5] for a fair comparison of the results.

2. X–ray afterglow sample and data analysis

We started to build our sample by adding to the sample of [5] the observations of long GRBs made by *Swift* between its launch and February 2013. We restricted this sample to bursts being observed by the XRT and having a measured redshift. This leads to a sample of 254 GRBs.

There are automated pipeline providing calibrated flux light curves [10, 11]. However, as stated before, we preferred to apply a similar method of the one of [5], and thus we did not use these final light curves. We however do use the raw count light curves provided by the Leicester online repository. This is the only difference with the work done in [5], as the manual extraction of more than 200 light curves would take too many time.

Once we have obtained these light curves and the associated event files, we apply our standard method, using the `HEASoft(v6.14)` that includes `XSPEC,XIMAGE,XSELECT` and *Swift* data analysis tools. First we run the XRT tool `xrtpipeline(v0.12.6)` to recalibrate the data using the latest available calibration. Being interested only in the afterglow part of the GRB, we removed from the data everything not related to the standard afterglow (i.e. the prompt phase when visible, the plateau phase, and the flares). We then extract a spectrum from the remaining data, and fit it
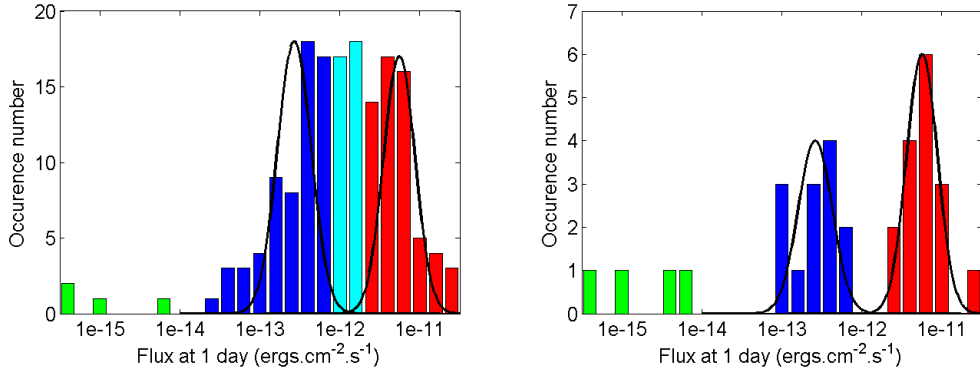
Figure 1: Flux distribution at 1 day after the burst. Left: our sample. Right: for comparison, the sample of [5]. Red, blue, and green bars show groups I, II, and III respectively. The cyan bars show the GRBs between Groups I and II. The black line shows the best-fit Gaussian distribution of [5].

with absorbed power law model (`wabs*zwabs*pow`). One of the absorption component is fixed to the galactic value, while the second is let free to vary at the redshift of the GRB. The best fit model allows us to compute the Energy Correction Factor (ECF) between counts and flux, in order to convert the raw count light curves in the standard 2-10 keV flux light curves.

To be consistent with previous papers we corrected the distance by normalizing all light curves in the standard distance to a redshift of $z = 1$. We thus correct for time dilation and we worked on 'rescaled flux' instead of luminosity. This is not mandatory to see the clusterings ([7] were working on luminosity), but allows for a more precise k-correction of the light curves, and thus add less systematic dispersion into any distribution. We finally build a normalized flux distribution at one day after the burst (in the common $z = 1$ frame) from these light curves.

3. Results

The final distribution we obtain is presented in Fig. 1 (left). For comparison, we also inserted the results of [5] as a similar distribution (right part of the figure). We can clearly see that, in agreement with the previous *Swift* era results, there is no clear clustering. In fact, we do observe 35 GRBs located between the groups I and II.

In order to check for any processing problems, we also checked a known *Swift* era correlation, i.e. the Dainotti correlation [12, 13], that links the date of the end of the plateau phase and the luminosity at that time. This correlation has its properties related to the clustering of light curves. The Fig. 2 present our check: we can reproduce the correlation, with its normal intrinsic distribution. We can also note that the red and blue points are distributed in two parallel layers with nearly no "systematic noise" within each group, which could indicate that the Dainotti correlation is stronger when considered for only one group of events. However, the 35 GRBs located between groups I and II (cyan points) are still problematic since they are placed everywhere and do not fit in any group. [12, 13] have worked only with GRBs that show a plateau phase, while we worked with all GRBs, considering in this case an extended version of Dainotti correlation. This should not impact
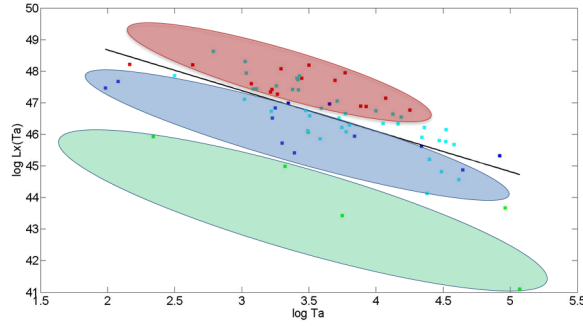
Figure 2: Dainotti correlation $\log(L_X(T_a))$ versus $\log(T_a)$. Red, blue and green points show Groups I, II and III respectively. Cyan points are 35 GRBs that are between Groups I and II.
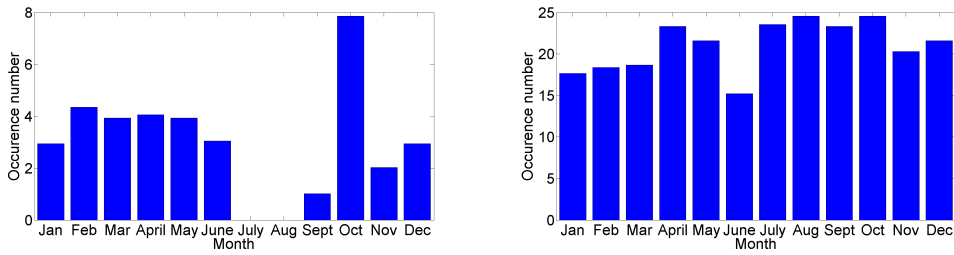

Figure 3: Left: Distribution of the month of detection for the 35 GRBs located between groups I and II. Right: Same distribution, but for our whole sample.

our results because we are working only with the beginning of afterglow, that is considered as the end of plateau phase [14].

4. Discussion

In the previous section, we have shown that in the *Swift* era, even when using our (slightly modified) method, we do not observe anymore the clustering of light curves. This leads to an interesting problem: why this clustering was observed in the pre-*Swift* era and not now? And does this also occurs for other GRB properties?

The obvious answer to the first question would be a selection effect. In the pre-*Swift* era, the rarity of X-ray light curves implies to build a sample of events observed by BeppoSAX, XMM-Newton, and Chandra. It is this mix that produce an (apparent) lack of events, then solved by *Swift*. This argument however does not hold, as the clustering was also observed when using only BeppoSAX data [2].

The fact that only the addition of *some* (not all) *Swift* bursts destruct the clustering made us wondering if there is not an instrumental problem. We checked the date of observation of these problematic events, and found some kind of periodicity (see Fig. 3, left part), with less problems near the solstices, and a maximum of problematic events near the equinoxes. This is outlined when one compare with the same distribution, but for all bursts (presented in Fig. 3, right part), where there is absolutely no periodicity (one should note that we normalized each month by its duration, so February and January can be fairly compared).
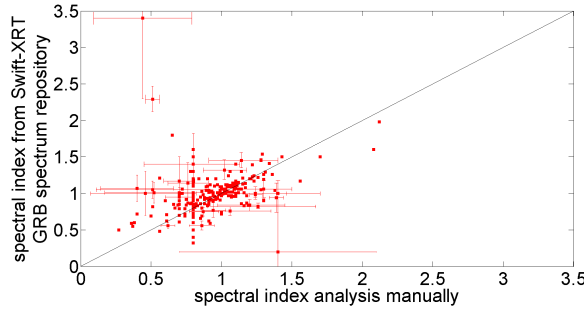
Figure 4: Comparison of the spectral indices from the manual analysis (x axis) and *Swift*-XRT GRB spectrum repository (y axis). The black line is the line of equality, where both results are equal. We removed for clarity from the plot the error bars of GRBs which are compatible with equality.

The first idea one can have at that time is a problem of Earth (or Sun) limb, i.e. an increase of the background induced by the orbit, and maybe not well taken into account during the data reduction. This could affect the raw light curve, or the spectrum. We thus tried to study both hypotheses.

We compared the spectral index of our manual analysis and the results from the *Swift*-XRT GRB spectrum repository [10, 11]. The result is displayed in Fig. 4. Clearly, in most of the cases, we are in close agreement. However, in about 11.2 % of the case, we found some discrepancies. We stress that this comparison is not straightforward, as we are not dealing with the exact same thing. First, in some cases, the temporal range for the extraction of the spectrum is not the same. We have extracted the spectrum of the *afterglow*, while the *Swift*-XRT GRB spectrum repository propose by default a time averaged spectrum between T_1 and T_2 of the object observed, irrespectively of its emission phase[1]. Second, each fit is done by using an absorbed power law model (`wabs*zwabs*pow`) one fixed in our own galaxy and one let free to the redshift, while the *Swift*-XRT GRB spectrum repository is using the same model but with two small differences: a. For some GRBs, the spectrum repository webpage reports an unknown value for the redshift, and in that case the spectral fit can give inconsistent results and b. *Swift*-XRT GRB spectrum repository is using `phabs` as an absorption model while we are using `wabs`. Last, the methods of correcting for pile-up are very different and can lead to strong differences. We are using the method explained at [15], while the limit for considering a pile-up region it is 0.8 counts/sec, but the *Swift*-XRT GRB spectrum repository is using 0.6 counts/sec [10, 11]. We thus do expect some differences, and found that about 90 % of compatibility is a good result. There are in any case 28 bursts with significant spectral discrepancies. Unfortunately, these are not all in the group of 35 problematic events. This is not the first main explanation so we are working in light curves to understand it better.

5. Conclusions

We have constructed a sample of 254 X-ray afterglows of *Swift* GRBs in order to check the clustering of afterglow light curves observed during the pre-*Swift* era. We can clearly see that in the

---

[1]A customized analysis, selecting the times T_1 and T_2 at the user requests, is however possible within online repository

Swift era, the clustering is no more apparent. We observe the presence of 35 bursts at the place of the separation of the two brightest groups. We have checked our analysis for a processing problem by reproducing the Dainotti correlation, found in the Swift era, and we successfully observed the correlation. We noted that each clustering group is consistent with the Dainotti correlation, and that could mean a kind of relationship between with correlation and the clustering correlation.

We also checked for instrumental effects and found that we have some seasonal effects for the 35 "between groups" GRBs. This could indicate a problem of background induced by the orbit. Checking our spectral analysis with the one of the *Swift*-XRT GRB spectrum repository, we found that in the majority of cases we are in agreement. However, for 11.20 % of bursts, we found some discrepancies. Some can be easily explained by a difference of time range (for the extraction of the spectrum) or model, while others are more difficult to understand. We are still working on this to understand the origin of this discrepancy.

6. Acknowledgement

References

[1] N. Gehrels, G. Chincarini, P. Giommi, et al. *ApJ* **1005** (2004) 611.

[2] M. Boër & B. Gendre, *A&A* **361** (2000) L21.

[3] B. Gendre & M. Boër, *A&A* **430** (2004) 465.

[4] C. Kouveliotou, C., S.E. Woosley, S.K. Patel, et al. *ApJ* **608** (2004) 872.

[5] B. Gendre, A. Galli & M. Boër , *ApJ* **683** (2008) 620.

[6] M. Nardini, G. Ghisellini, G. Ghirlanda, et al. *A&A* **451** (2006) 821.

[7] E. Liang and B. Zhang, *ApJ* **638** (2006) L67.

[8] B. Gendre, S. Pelisson, M. Boer, et al. *A&A* **492** (2008) L1.

[9] A. Melandri, S. Covino, D. Rogantini, et al. *A&A* **565** (2014) A72.

[10] P. A. Evans, A. P. Beardmore, K. L. Page, et al. *A&A* **469** (2007) 379.

[11] P. A. Evans, A. P. Beardmore, K. L. Page, et al. *MNRAS* **397** (2009) 1177.

[12] M. G. Dainotti, V. F. Cardone and S. Capozziello, *MNRS* **391** (2008) L79.

[13] M. G. Dainotti, R. Willingale, S. Capozziello, et al. *ApJ* **722** (2010) L215.

[14] R. Willingale, P. T. O'Brien, J. P. Osborne, et al. *ApJ* **1093** (2007) 662.

[15] S. Vaughan, M. R. Goad, A. P. Beardmore, et al. *ApJ* **920** (2006) 638.